NUMERICAL INVESTIGATION OF COMBUSTION PROCESS IN REACTIVITY CONTROLLED COMPRESSION IGNITION (RCCI) ENGINE

ZHOU DEZHI

(B.Eng., Shanghai Jiao Tong University, China)

Supervisors:
Assistant Professor Yang Wenming
Professor Shu Chang

Examiners:
Professor Chou Siaw Kiang
Associate Professor Chua Kian Jon, Ernest
Professor Jyh-Yuan Chen, University of California at Berkeley

A DISSERTATION SUBMITTED

FOR THE DEGREE OF DOCTOR OF PHILOSOPHY

DEPARTMENT OF MECHANICAL ENGINEERING

NATIONAL UNIVERSITY OF SINGAPORE

2017

DECLARATION

I hereby declare that the dissertation is my original work and it has been written by me in its entirety. I have duly acknowledged all the sources of information which have been used in the dissertation.

This dissertation has also not been submitted for any degree in any university previously.

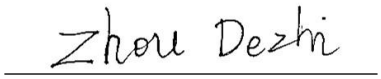

Zhou Dezhi
22 April 2017

Dedicated to my beloved family and my fiancé Ji Ya

Acknowledgements

Trekking through this four-year pathway with self-denial and failure, I now deeply comprehend the meaning of the traditional Chinese poem "after endless mountains and rivers that leave doubt whether there is a path out, suddenly one encounters the shade of a willow, bright flowers and a lovely village." At this special moment, I want to sincerely express my thanks to the people who took me out of the “endless mountains and rivers” and took me to the “lovely village”.

I still remember the first phone call from my main supervisor Professor Yang in May, 2013 when I was at home in China, asking me about the preparation issues of the trip to Singapore. The impression got from this call that Professor Yang is a so caring and kind person was even enhanced when I first met him at his office, talking about my future research directions in July, 2013. During my whole Ph.D. journey, the insightful guidance and valuable feedbacks from Professor Yang have always been leading me into a correct and bright direction in research. Professor Yang, I am very grateful for all the talks we had at your office when I had doubts in research, for all the tea breaks we had at E2 canteen where you treated us to *“Kopi”* and shared your ideas, and for all the joy we had during the trip to Miami and Huston with your family. Thank you Professor Yang!

I am also very indebted to Professor Shu Chang, who agreed to co-supervise me with the sacrifice of his own student quota. Professor Shu is a leading expert in CFD worldwide. I am very regretful to not communicate with him frequently during my Ph.D. program. I hope it is still possible to compensate this regret even after my Ph.D. program. Thank you Professor Shu!

Special appreciation sincerely goes to my two seniors, Dr. An Hui and Dr. Li Jing, for their continuous guidance to help me understand the daunting KIVA codes. Without them, I would not even know how and where to begin my research when I was new in this research field. I would also like to thank all the other members in Professor Yang's research team: Dr. Yu Wenbin, Dr. Zhao Feiyang, Dr. Balaji Mohan, Dr. Jiang Dongyue, Dr. Cui Xin, Mr. Tay Kun Lin, Dr. Liu Teng, Mr. Wu Shaohua, Mr. Zhao Wensheng and Mr. Li Han and all the colleagues in TPL1: Dr. Sun Bo, Mr. Yan Yuexiang, Mr. Xu Jia, Dr. Ge Mengyi, Mr. Li Hongkun and Mr. Ravi Ranjan for their kind help and constant support for my research. These guys have not only been supportive in my research, but also been blending various colors into my plain life in Singapore. I am very blessed to have you guys during my Ph.D. life in Singapore!

Little would be achieved in this dissertation without the resource and technical help from NUS HPC center. I want to thank the anonymous

technicians from NUS HPC center for answering every question in my email about the code compilation. Additional thanks go to Professor Kong Song-charng (Iowa State University) for sharing his classical SHELL-CTC model codes developed by himself and Professor Ren Weiqing (math department at NUS) for his insightful comments about HMM.

I owe my utmost gratitude to my parents and my elder brother. Their continuous cultivation and unconditional love on me are the biggest reason why I am the person who I am now and why I am here where I am now. Finally, I want to dedicate this dissertation to my beloved fiancée Ji Ya, who has been accompanying me to get through this four-year fantastic voyage, during which, we together experienced ups and downs, coldness and warmth, hardships and surprises. No matter what will happen in the future, I will be here with you.

Table of Contents

Summary

The reactivity controlled compression ignition (RCCI) engine concept is attractive because of its potential high efficiency and low emissions over a wide range of operating conditions. However, due to its special fuel intake manner, the combustion process in RCCI engines is complex, rendering some major challenges to its combustion process modeling.

First of all, dual-fuel chemical reaction mechanisms with compact size and robust accuracy are critical to model the combustion process of RCCI engines. Meanwhile, the co-existence of diffusion flame, auto-ignition and flame propagation in RCCI engines necessitates a unified combustion model for considering all these three different combustion modes. Moreover, the chemistry stiffness in the multidimensional engine combustion simulations causes prohibitive computational cost. Hence, in this thesis 3 different primary reference fuel mechanisms (one coupled with PAH for soot formation modeling) with different sizes were proposed to deal with the combustion chemistry in RCCI engine fueled with gasoline/diesel. It is validated that these three mechanisms are able to capture the combustion characteristics in terms of ignition delay in constant volume auto-ignition, laminar flame speed in premixed diffusion flame, intermediate species profiles in JSR and in-cylinder pressure in RCCI engines. Then, a hybrid combustion model with detailed chemistry is developed by coupling a characteristic timescale combustion

model and a well-mixed reactor model to simulate the diffusion flame and auto-ignition in RCCI combustion, respectively. This model is capable of simulating the interaction between the chemistry and turbulence and capturing the auto-ignition and diffusion flame in RCCI engines. Subsequently, a Lagrangian marker model is developed and added for the possible flame propagation in RCCI engines. These combustion models are able to model the three different combustion types, i.e., auto-ignition, diffusion flame and flame propagation, in RCCI engines. Finally, to accelerate the simulation of RCCI engines, a parallel computing algorithm for the chemistry integrator and a heterogeneous multiscale method for stiff chemistry integration are proposed. It is shown that these two methods could reduce the computational overhead in engine simulations by nearly 10 times.

List of Tables

List of Figures

List of Symbols

Abbreviations

ATDC	After top dead center
CCM	Chemistry coordinate mapping
CDC	Conventional diesel combustion
CFD	Computational fluid dynamics
CI	Compression ignition
CMC	Conditional moment closure
CN	Cetane number
CO-DAC	Correlated dynamic adaptive chemistry
CO	Carbon monoxide
CO_2	Carbon dioxide
CPU	Central processing unit
CTC	Characteristics timescale combustion
CVC	Constant volume combustion
DAC	Dynamic adaptive chemistry
DDM	Discrete droplet model
DICI	Direct injection compression ignition
DME	Dimethyl ether
DNS	Direct numerical simulation
DPIK	Discrete particle ignition kernel

DRG	Direct relation graph
DRGEP	DRG with error propagation
DRGEPSA	DRGEP aided with sensitivity analysis
ECFM3Z	Extended coherent flame 3 zones
EGR	Exhaust gas recirculation
FPM	Flame propagation model
GDI	Gasoline direct injector
CPU	Graphics processing unit
HACA	Hydrogen abstraction-C_2H_2 addition
HCCI	Homogeneous charge compression ignition
HMM	Heterogeneous multiscale method
HPC	High performance computing
HRF	High reactivity fuel
HRR	Heat release rate
ICE	Internal combustion engine
ISAT	*in situ* adaptive tabulation
IVC	Intake valve close
JSR	Jet stirred reactor
KH	Kelvin- Helmholtz
LES	Large eddy simulation
LFS	Laminar flame speed

LRF	Low reactivity fuel
LTC	Low temperature combustion
M1	Mechanism 1
M2	Mechanism 2
M3	Mechanism 3
NG	Natural gas
NTC	Negative temperature coefficient
NUS	National University of Singapore
MPI	Message passing interface
ODE	Ordinary differentiate equation
PAH	Polycyclic aromatic hydrocarbon
PCCI	Premixed charge compression ignition
PDF	Probability density function
PE	Partial equilibrium
PFI	Port fuel injector
PM	Particulate matter
PRF	Primary reference fuel
PRR	Pressure rise rate
QSS	Quasi steady state
RANS	Reynolds-averaged Navier-Stokes
RCCI	Reactivity controlled compression ignition

RCM	Rapid compression machine
rpm	Revolution per minute
RNG	Re-Normalization group
RT	Rayleigh-Taylor
SI	Spark ignition
SOI	Start of injection
TDC	Top dead center
UHC	Unburnt hydrocarbon

Chemical symbols

A1	Benzene
A_2R_5	Acenaphthylene
C(S)	Soot
H_2O	Water
NO	Nitrogen monoxide
NO_2	Nitrogen dioxide
NO_x	Nitrogen oxides
RH	Alkane
R*	Alky radical
P	Oxidized products including CO, CO_2 and H_2O
B	Branching agent
Q	Labile intermediate species

Nomenclature

a	Dimensionless quantity
b	Collision impact parameter
D	Diffusion coefficient in Fick's Law
D_n	Species concentrations destruction rate of Species n
Da	Damköhler number
$\mathbf{F}$	Rate of momentum gain per unit volume
$\mathbf{g}$	Specific body force, assumed constant
G	Scalar in G equation
I	Total reaction number in a chemical mechanism
$\boldsymbol{J}$	Heat flux
k	Turbulent kinetic energy
L	Critical length in KH-RT model
l_I	Turbulence integral length scale
MW	Molecular weight
N	Total species in a chemical mechanism
p	Fluid pressure
Pr	Prandtl number
q	Reaction rate
Q	Energy source term
r	Radius of droplet

R	Rate-of-strain term in RNG $k-\varepsilon$ model
S	Flame speed
t	Time
T	Temperature
V	Volume
$\mathbf{u}$	Velocity of fluid
u'	Isotropic turbulence intensity
$\dot{W}$	Source term of turbulent eddies rate
$\dot{y}$	Oscillation velocity
X	Molar fraction
Y	Mass fraction
Y^*	Instantaneous equilibrium value of mass fraction

Greek symbols

δ	Dirac delta function
ε	Turbulent dissipation rate
Λ	Wave length of the fastest growing wave
ν	Collision frequency
ρ	Mass density
$\boldsymbol{\sigma}$	Stress tensor
τ	Time scale
υ	Stoichiometric coefficient

ϕ	Equivalence ratio
$\dot{\omega}$	Production rate of species
Ω	Growth rate of the fastest growing wave

Subscripts

b	Burnt
c	Child droplet
dil	Diluent
n	Species index in a chemical mechanism
i	Reaction index in a chemical mechanism
i4	Cell index in KIVA
coll	Terms due to droplet collisions
bu	Terms due to droplet breakups
l	Laminar
t	Turbulence
u	Unburnt

Superscripts

c	Source term due to chemistry
s	Source term due to spray
p	Parent droplet

List of Publications

Publications in peer reviewed journals:

1. **DZ Zhou**, WM Yang, H An, J Li, C Shu. A numerical study on RCCI engine fueled by biodiesel/methanol. Energy Conversion and Management 89 (2015) 798-807. [Link to this article]
2. **DZ Zhou**, WM Yang, H An, J Li. Application of CFD-chemical kinetics approach in detecting RCCI engine knocking fueled with biodiesel/methanol. Applied Energy 145 (2015) 255-264. [Link to this article]
3. **DZ Zhou**, WM Yang, H An, J Li, M Kraft. An Enhanced Primary Reference Fuel Mechanism Considering Conventional Fuel Chemistry in Engine Simulation. Journal of Engineering for Gas Turbines and Power 138 (9), 092804. [Link to this article]
4. **DZ Zhou**, WM Yang, J Li, KL Tay. Simplified fuel cracking process in reduced mechanism development: PRF–PAH kinetic models for combustion and soot prediction. Fuel 182 (2016) 831-841. [Link to this article]
5. **DZ Zhou**, WM Yang, J Li, KL Tay, M Kraft. Combustion Modeling in RCCI Engines with a Hybrid Characteristic Time Combustion and Closed Reactor Model. Applied Energy (Under Review).
6. **DZ Zhou**, WM Yang, FY Zhao, J Li. Dual-Fuel RCCI Engine Combustion Modeling with Detailed Chemistry Considering Flame Propagation in Partially Premixed Combustion. Applied Energy (Under Review).
7. H An, WM Yang, J Li, **DZ Zhou**. Modeling study of oxygenated fuels on diesel combustion: Effects of oxygen concentration, cetane number and C/H ratio. Energy Conversion and Management 90 (2015) 261-271. [Link to this article]

8. H An, WM Yang, J Li, **DZ Zhou**. Modeling analysis of urea direct injection on the NOx emission reduction of biodiesel fueled diesel engines. Energy Conversion Management,101 (2015) 442-449. [Link to this article]
9. J Li, WM Yang, H An, **DZ Zhou**, WB Yu, JX Wang, L Li. Numerical investigation on the effect of reactivity gradient in an RCCI engine fueled with gasoline and diesel. Energy Conversion and Management 92 (2015) 342-352. [Link to this article]
10. J Li, WM Yang, H An, **DZ Zhou**, Soot and NO emissions control in a natural gas/diesel fueled RCCI engine by φ-T map analysis. Combustion Theory and Modeling (2016) 1-20. [Link to this article]
11. KL Tay, WM Yang, B Mohan, **DZ Zhou**, WB Yu, FY Zhao. Development of a reduced kerosene–diesel reaction mechanism with embedded soot chemistry for diesel engines. Fuel 181(2016) 926-934. [Link to this article]
12. J Li, WM Yang, **DZ Zhou**. Review on the management of RCCI engines. Renewable and Sustainable Energy Reviews 69 (2017) 65-79. [Link to this article]

Proceedings in peer reviewed conferences:

1. **DZ Zhou**, WM Yang, H An, J Li, SK Chou, M Kraft. Efficient Combustion Modelling in RCCI Engine with Detailed Chemistry. 8th International Conference on Applied Energy. October 8-11, 2016, Beijing, China.
2. **DZ Zhou**, WM Yang, H An, J Li, M Kraft. An enhanced PRF mechanism considering conventional fuel chemistry in engine simulation. ASME 2015 International Combustion Engine Division Fall Technical Conference. November 8-11, 2015, Houston, TX, US.

Chapter 1 Introduction

1.1 Background and motivation

Since the spark ignition (SI) engine was invented in 1876 by Otto and the compression ignition (CI) engine was developed in 1892 by Diesel, internal combustion engines have been playing a dominant role in human life for power generation, propulsion and energy conversion [1]. For instance, CI engines have been widely applied in transportation such as automobile, trucks and marine and SI engines have been widely used in the home (e.g., chain saws), in motorcycles and invariably in automotive practice [1]. The different application occasions between CI and SI engines are due to their different operation features. In CI engines, the fuel (i.e., diesel) is directly injected into the engine cylinder before the combustion occurrence. Due to the high compression ratio and high fuel reactivity, the combustion is triggered by the compression itself. The high compression ratio is also the reason why CI engines possess high thermal efficiency. However, because of its instinct operation manner, the high temperature and fuel rich zones in the combustion chamber are conducive to the formation of detrimental emissions such as nitrogen oxides (NO_x) and particulate matter (PM). Nonetheless in SI engines, the fuel (i.e., gasoline) and air are mixed prior to their induction into the cylinder. Because of the low compression ratio and low reactivity of gasoline, a spark plug is employed to

start the combustion. Consequently, SI engines organize the combustion in a premixed way and have lower thermal efficiency but better emission performance than CI engines.

Nowadays, as the demand for new engine types (besides of conventional SI and CI engines) arose, especially considering the more and more stringent emission regulations and severe fossil fuel crisis, efforts have been devoted to developing advanced combustion modes to aggregate the advantages of CI and SI engines and at the same time, avoid their disadvantages. In the past decades, a number of advanced combustion modes in engines have been proposed and studied, including homogeneous charge compression ignition (HCCI), premixed charge compression ignition (PCCI), homogeneous charge induced ignition (HCII), stratified charge compression ignition (SCCI) and RCCI, just to name a few [2]. Though their names might vary, the philosophies of them are similar. Hence, three of them (i.e., HCCI, PCCI and RCCI) are selected here to discuss the evolving history of the advanced combustion modes in engines.

Before RCCI and PCCI were proposed, HCCI had been studied for years. Both the numerical and experimental results showed that HCCI yielded high efficiency and nearly zero emissions [3]. Unfortunately, the combustion phasing of HCCI is purely determined by the fuel kinetics and HCCI is difficult to realize at high load conditions due to severe engine knocking problems [2]. Based on the concept of HCCI, PCCI was developed by injecting the fuel with

very early injection timing to form partially premixed charge. PCCI is able to preliminarily control the combustion phasing by adjusting the injection timing [4-8]. Both numerical and experimental investigations suggest that PCCI presents better combustion controllability than HCCI [9-11]. However, the high pressure rise rate and thereby the unacceptable engine knocking at high loads is still a major challenge in PCCI. In contrast, RCCI overcomes the drawbacks of HCCI and PCCI with proper combustion phasing control method by adjusting the high reactivity fuel injection timing and varying the ratio of low reactivity and high reactivity fuels at various operating conditions. Specifically, RCCI employs a port fuel injection with low reactivity fuels and a direct injection with high reactivity fuels (as shown in Figure 1.1, where LRF and HRF mean low reactivity fuel and high reactivity fuel), thereby forming fuel reactivity gradient in the combustion chamber to achieve high combustion-phase controllability. A comparative description of HCCI, PCCI and RCCI in terms of their fuel intake manners, combustion phasing controlling methods and fuel burning manner are summarized in Table 1.1.

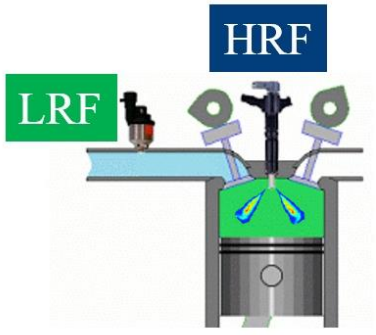

Figure 1.1 Schematic on RCCI engine [12]

Table 1.1 HCCI, PCCI and RCCI comparison

Combustion Concepts	Fuel intake manner	Combustion phasing control	Fuel burning manner
HCCI	Port injection	Fuel kinetics	Auto-ignition
PCCI	Early direct injection	Injection timing	Partially premixed combustion
RCCI	Port + direct injection	Direct injection timing, premixed fuel ratio	Partially premixed combustion

However, as indicated by Li et al. [13] and Reitz et al. [14], to realize the application of RCCI in automobile industry, more extensive fuel and engine management in RCCI engines is needed to overcome the obstacles of high hydrocarbon emissions at low loads and engine knocking tendency at high loads. Due to the explosively extending computer facilities nowadays, numerical investigation of RCCI engine is becoming more and more significant due to its lower cost. More importantly, numerical analysis could provide in-depth understanding about the combustion process (e.g., the role of fuel reactivity, the mechanism of engine knocking) in RCCI engines which, however, is impossible to obtain experimentally. Hence, the need for accurate and efficient numerical investigations of the combustion process in RCCI engines motivates the research work in this dissertation.

1.2 Strategy and challenges

Combustion models, developed and coupled with CFD solvers and other physical models (e.g., fuel spray model), is the numerical strategy to investigate the combustion process in RCCI engines in this dissertation. The development and optimization of combustion models in the multidimensional RCCI engine simulations with detailed chemistry are the focus of this dissertation.

Combustion modeling is very significant but challenging. It is often claimed that the practical application of combustion is much more advanced than its theoretical insight because combustion has been applied in every aspect

of human industry and life whereas the theoretical explanation of the stabilization mechanism in a simple lifted jet flame is still under debate [15]. In this sense, to understand the theoretical nature of combustion and utilizing combustion more efficiently and cleanly, combustion modeling plays an irreplaceable role. Nowadays, although the combustion of a simple 0-D homogeneous auto-ignition could be precisely modeled with accurate stiff ordinary differentiate equations (ODEs) solvers and detailed chemical mechanisms, accommodating realistic characterization of physical and chemical properties of gas mixtures into large-scale multidimensional combustion modeling (i.e. engine combustion simulation) is still very challenging [16]. The challenges manifest in the computational complexity arose from the computation of turbulence, chemical reactions, emission formation and other physical processes (e.g., fuel spray and evaporation). The modeling of these physiochemical processes leads to complex balance equations and high difficulty to solve these equations. With the expanded computer capacity and the development of computational fluid dynamics (CFD) algorithms, it is now possible to solve the balance equations in reactive flows with acceptable accuracy and cost. Even so, there is still a major concern: the prohibitive computational cost caused by the integration of the strongly coupled stiff transport-chemical source terms in the governing equations and by the highly-discretized spatial and temporal dimensions.

Therefore, in order to conduct feasible multidimensional combustion modeling, customized combustion models should be developed for certain types of flame (e.g., premixed turbulence flame, diffusion laminar flame) to simplify the combustion modeling [17]. Another simplification approach to obtain affordable multidimensional combustion simulation is to simulate with coarse chemical reactions or advanced chemistry integration schemes. Hence, all of these concerns invoke the requests for developing specific combustion models for certain problems and proposing advanced schemes for combustion chemistry integration.

Being subordinate to multidimensional CFD combustion modeling, the simulation of RCCI engines faces the same challenges. Moreover, in addition to the combustion process, other complex physical features such as fluid flow, fuel evaporation, liquid particle break-up, collision, emission formation and turbulence et al. also need to be considered. Even so, combustion modeling is still regarded to be one of the hardest due to several reasons [18]. Firstly, the combustion process in engines involves fuels with various components, each of which consists of hundreds of species and thousands of reactions, resulting in the complexity of chemical reaction mechanism development. Secondly, different combustion organization modes including flame propagation, diffusion flame or auto-ignition should be accounted for in the combustion modeling. Thirdly, in the combustion process, different chemical species have

their own reaction timescales, leading to high stiffness of the chemical source term integration and thus prohibitive computational cost even in the context of Reynolds-averaged Navier-Stokes (RANS).

To address these problems, different combustion models have been developed for both conventional CI engines and SI engines. In 1995, Kong et. al [19] proposed a SHELL characteristics timescale combustion (CTC) model by using an empirical correlation to account for the chemical time-scale and mixing time-scale to model conventional CI engines. They also integrated detailed chemistry into modeling auto-ignition in HCCI engine by the CHEMKIN-II package [20]. These two models are capable of modeling diffusion flame and auto-ignition in CI engines. With respect to SI engines where flame propagation dominates the combustion, G-equation [21] and Lagragian marker model [22] are two classical models for flame propagation modeling.

However, in RCCI engines, due to its special fuel intake manner, auto-ignition, diffusion flame and flame propagation could co-exist and consequently, its combustion modeling needs to be dealt with special care because the models should resolve all of these different flame types [23, 24]. To cover all the three flame types in RCCI engines, a unified combustion model being able to handle all the possible combustion regimes is needed. Moreover, to couple in detailed chemistry and calculate the finite rate combustion

chemistry in RCCI simulations, dual fuel chemical reaction mechanisms need to be developed. Another major concern in combustion modeling in RCCI engines is the expensive computational overhead.

1.3 Objectives

Therefore, the objective of this dissertation is to develop robust and unified combustion models, chemical mechanisms and advanced schemes to investigate the combustion process in RCCI engines moreeffectively and efficiently. To achieve this goal, a reduced primary reference fuel (PRF) mechanism with polycyclic aromatic hydrocarbons (PAH) embedded was firstly proposed and validated to consider diesel/gasoline dual fuel combustion and emission formation in RCCI engines. Then, a detailed chemistry hybrid combustion model with a CTC model for diffusion flame and a well-premixed reactor model for auto-ignition was proposed for the different combustion regimes in RCCI combustion. Subsequently, to model the possible flame propagation in RCCI combustion, a Lagragian marker model with detailed chemistry was developed and coupled with CHEMKIN-II. Finally, toward accelerating the computation of RCCI modeling, a parallel computing algorithm was developed to parallelize the chemistry solver computation, based on the message passing interface (MPI) architecture and the round-robin algorithm. A heterogeneous multi-scale method (HMM) was also proposed and applied to accelerate stiff combustion chemistry integration.

By integrating these models and schemes into a basic CFD framework KIVA-4 (a serial of open-source codes), this dissertation provides a numerical framework for investigating the combustion process in RCCI engines under different operating conditions with affordable computational cost and reliable prediction accuracies.

1.4 Outline

This dissertation consists of seven chapters. Chapter 1 introduces the background of RCCI engines and presents the strategy and challenges in the numerical investigation of the combustion process in RCCI engines. The objectives and outline of this dissertation are also shown in Chapter 1. 0 introduces the numerical tools for RCCI modeling. The last section in this chapter focuses on reviewing the combustion models in engines, including different combustion models in different engines, surrogate chemical reaction models for gasoline/diesel fuels and acceleration approaches for engine combustion modeling. Chapter 3 presentes a PRF dual fuel mechanism with PAH embedded in. A hybrid combustion model with a CTC model and a well-premixed reactor model to model the diffusion flame and auto-ignition in RCCI combustion with detailed chemistry is given in 0. 0 presents the modeling of the possible flame propagation in RCCI combustion with detailed chemistry by a Lagragian marker model. In Chapter 6, a parallel algorithm based on MPI is firstly introduced. A heterogeneous multiscale method is also applied to

accelerate the integration of the stiff chemical source terms. Finally, Chapter 7 summarizes the major findings and contributions in this dissertation. The recommendations for future work are also given in this chapter.

This page was intentionally left blank

Chapter 2 Modeling RCCI Engines

This chapter firstly introduces the numerical tools for RCCI modeling, including the CFD framework, governing equations, turbulence models and spray modeling. Then, the strategies to model combustion process for RCCI engine simulations are thoroughly reviewed.

2.1 Numerical tools

2.1.1 DNS, LES or RANS

The computational cost of simulations, which is characterized by the time consumed in CPUs or GPUs, is always a major concern from a practical point of view. With the emergence of super computers and high performance algorithms in CFD, multidimensional reactive flow simulations with detailed chemistry became possible. However, multidimensional direct numerical simulations (DNS), which is subject to the Kolmogorov scales and requires not only time integration computation effort, but also tremendous amount of spatial discretization computation, is still computationally prohibitive. Navier–Stokes equations in DNS are numerically solved without any turbulence model, meaning that the whole range of spatial and temporal scales of the turbulence must be resolved. Hence, most of DNS are restricted to 1-D or 2-D small molecule-fuel (such as hydrogen) combustion simulations with presumed fuel preparation, temperature profiles in the computational domain [25-31]. In

multidimensional simulations with big realistic fuels and other complex physical treatments, most of the feasible numerical tools are in the context of large eddy simulations (LES) and Reynold averaged Navier-Stokes simulations (RANS).

As shown in Figure 2.1, LES reduces the computational cost by low-pass filtering the smallest length scales. The low-pass filtered scales will be resolved by some empirical models, by which, the prohibitive computational cost incurred by the extremely small scales in DNS is alleviated. Hence, some multidimensional engine simulations were conducted by LES and the prevalent engine simulation CFD tool KIVA code has also been modified into LES versions [32-34]. After all, one of the motivations to seek the help of numerical simulations instead of experiments on optimizing engine design is because of its high efficiency. With acceptable accuracy and desirable outputs, it is then favorable to conduct engine simulations in the regime of RANS due to its highest computational efficiency. Indeed, most of the numerical simulations of multidimensional engines are conducted within RANS.

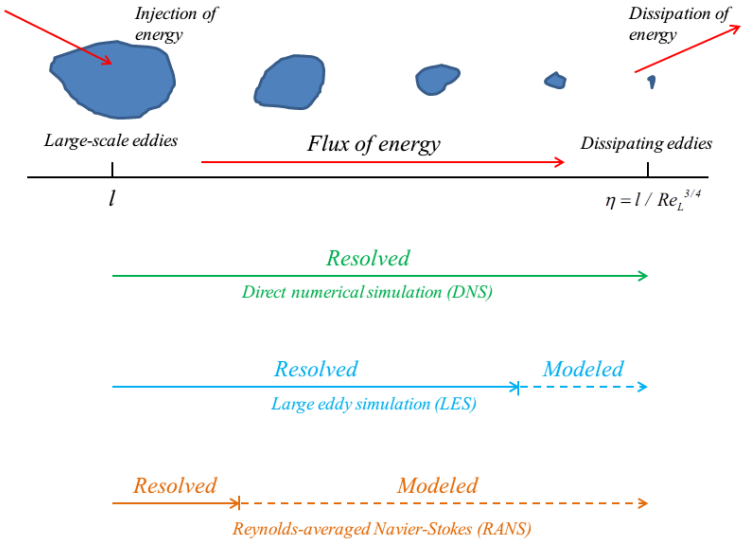

Figure 2.1 Schematic of the length scales resolved in DNS, LES and RANS [35]

In this dissertation, all the numerical simulations were conducted in the regime of RANS with a serial of open-source codes, KIVA-4 [36], which was originally developed by Los Alamos National Laboratory and then modified for different purposes by different institutes. It is capable of computing transient problems in multidimensional moving mesh with fuel sprays and combustion chemistry. Based on the previous version KIVA-3V which uses a finite volume method for arbitrary hexahedrons, KIVA-4 is capable of treating unconstructed meshes. The spatial discretization in KIVA family codes is based on the method of arbitrary Lagrangian Eulerian (ALE) [37]. The transport terms are differenced by a quasi-second-order up-winding scheme and a second-order central scheme respectively for the convection term and the diffusion term. The temporal integration is based on a first-order time-splitting scheme. For completeness, the governing equations together with all of the other models including the turbulence model, spray models equations in KIVA-4 are briefly

introduced here.

2.1.2 Governing equations

The unsteady reactive flow with turbulence in engines is governed by continuity, momentum, and energy equations, which are given as:

Continuity equation,

$$\frac{\partial \rho_n}{\partial t} + \nabla \cdot (\rho_n \mathbf{u}) = \nabla \cdot (\rho D \nabla (\frac{\rho_n}{\rho})) + \dot{\rho}_n^C + \dot{\rho}^S \delta_{n1} \tag{2.1}$$

Momentum equation,

$$\frac{\partial (\rho \mathbf{u})}{\partial t} + \nabla \cdot (\rho \mathbf{u}\mathbf{u}) = -\frac{1}{a^2} \nabla p - \nabla (\frac{2}{3} \rho k) + \nabla \cdot \boldsymbol{\sigma} + \mathbf{F}^{\mathrm{S}} + \rho \mathbf{g} \tag{2.2}$$

Energy equation,

$$\frac{\partial (\rho I)}{\partial t} + \nabla \cdot (\rho \mathbf{u} I) = -p \nabla \cdot \mathbf{u} - \nabla \cdot \mathbf{J} + \rho \varepsilon + \dot{Q}^C + \dot{Q}^S \tag{2.3}$$

The meanings of all the symbols are listed in Table 2.1.

Table 2.1 Meanings of the symbols in the governing equations (Eq. (2.1), (2.2) and (2.3)) of a unsteady reactive flow

Symbols	Meanings
ρ	mass density
t	time
$\mathbf{u}$	the velocity of fluid
D	diffusion coefficient in Fick's Law
δ	Dirac delta function
a	dimensionless quantity
p	fluid pressure
$\boldsymbol{\sigma}$	stress tensor
$\mathbf{F}$	rate of momentum gain per unit volume
$\mathbf{g}$	specific body force, assumed constant
I	specific internal energy, excluding chemical energy contribution
$\boldsymbol{J}$	the heat flux
k	turbulent kinetic energy
ε	turbulent dissipation rate
Q	energy source term
n	subscripts: species that compose the mixture
c	superscripts: source term due to chemistry
s	superscripts: source term due to spray

2.1.3 Turbulence modeling

As a type of RANS simulation, the current KIVA-4 codes adopted a classical turbulent model - the RNG (Re-Normalization Group) $k-\varepsilon$ model [38, 39]. The k equation and ε equation in RNG $k-\varepsilon$ model are:

$$\frac{\partial(\rho k)}{\partial t}+\nabla\cdot(\rho\mathbf{u}k)= -\frac{2}{3}\rho k\nabla\cdot\mathbf{u}+\sigma:\nabla\mathrm{u}+\nabla\cdot\left[\left(\frac{\mu}{Pr_k}\right)\nabla k\right]-\rho\varepsilon+\dot{W}^s \tag{2.4}$$

$$\frac{\partial(\rho\varepsilon)}{\partial t}+\nabla\cdot(\rho\mathbf{u}\varepsilon)=-\left(\frac{2}{3}C_{\varepsilon_1}-C_{\varepsilon_3}\right)\rho\varepsilon\nabla\cdot\mathbf{u}+\nabla\cdot\left[\left(\frac{\mu}{Pr_\varepsilon}\right)\nabla\varepsilon\right] +\frac{\varepsilon}{k}\left[C_{\varepsilon_1}\sigma:\nabla\mathbf{u}-C_{\varepsilon_2}\rho\varepsilon+c_s\rho\varepsilon+c_s\dot{W}^s\right]-\rho R \tag{2.5}$$

where $\dot{W}^s$ is the spray source term. C_{ε_1} and C_{ε_2} are constants with the values of 1.42 and 1.68, respectively. C_{ε_3} is defined as:

$$C_{\varepsilon_3}=\frac{-1+2C_{\varepsilon_1}-3m(n-1)+(-1)^{\delta}\sqrt{6}C_\mu C_\eta\eta}{3} \tag{2.6}$$

where constant *m* has the value of 5 while *n* is the polytropic index for adiabatic process with a value of 1.4. C_η and δ are given by:

$$C_\eta=\frac{\eta(1-\eta/\eta_0)}{1+\beta\eta^3} \tag{2.7}$$

$$\delta=\begin{cases}1, & \nabla\cdot\mathbf{u}\le 0.0\\ 0, & \nabla\cdot\mathbf{u}>0.0\end{cases} \tag{2.8}$$

As the rate-of-strain term in RNG $k-\varepsilon$ model, R is defined as:

$$R=\frac{C_\mu\eta^3(1-\eta/\eta_0)}{1+\beta\eta^3}\frac{\varepsilon^2}{k} \tag{2.9}$$

with $\eta=\frac{k}{\varepsilon}S$, $\eta_0=\sqrt{\frac{C_{\varepsilon_1}-1}{C_\mu\left(C_{\varepsilon_1}-1\right)}}$, $\beta=0.012$, $S=\sqrt{2S_{ij}S_{ij}}$ and $S_{ij}=\frac{1}{2}\left(\frac{\partial\overline{u}_i}{\partial x_j}+\frac{\partial\overline{u}_j}{\partial x_i}\right)$.

Other constants in this model are tabulated in Table 2.2.

Table 2.2 Constants used in the RNG $k-\varepsilon$ model

Constants	$C_{\varepsilon 1}$	$C_{\varepsilon 2}$	C_{μ}	Pr_k	$\mathrm{Pr}_{\varepsilon}$	C_S
Values	1.42	1.68	0.0845	0.72	0.72	1.5

2.1.4 Spray modeling

The fuel spray could significantly affect the combustion process because it directly decides the level of fuel atomization and fuel/air homogeneity. The fuel spray models in KIVA-4 are very complex, which could be sequentially divided into three phases: fuel spray, fuel droplet break-up and parcels collision. In KIVA-4, a Monte-Carlo based method called discrete droplet model (DDM) [40] is adopted to solve the spray equations. This method integrates the droplet distribution function f temporally by:

$$\frac{\partial f}{\partial t} = -\frac{\partial}{\partial x_i}(f v_i) - \frac{\partial}{\partial v_i}(f F_i) - \frac{\partial}{\partial r}(f R) - \frac{\partial}{\partial T_d}(f \dot{T}_d) - \frac{\partial}{\partial y}(f \dot{y}) - \frac{\partial}{\partial \dot{y}}(f \ddot{y}) + \dot{f}_{coll} + \dot{f}_{bu} \tag{2.10}$$

where F_i, R, $\dot{T}_d$ and $\ddot{y}$ are the temporal change rate of one droplet's velocity, radius, temperature and oscillation velocity $\dot{y}$, respectively. $\dot{f}_{coll}$ and $\dot{f}_{bu}$ are the source terms due to droplet collisions and breakups.

The subsequent fuel droplet breakup after the fuel spray will iteratively occur to form new fuel droplets until all the fuel has evaporated into gas phase. A hybrid KH-RT (Kelvin-Helmholtz and Rayleigh-Taylor) model [41] is used in the current KIVA-4 version. The fuel spray region is separated into two in

which, the first region, KH breakup model is applied near the nozzle whereas in the second region where the distance from the droplets to the nozzle exceeds a critical breakup length *L*, RT model is applied to model the secondary breakup.

The diameter change of the first breakup from a parent droplet to a child one is given by:

$$\dot{r}_p = \frac{r_p - r_c}{\tau_{KH}} \tag{2.11}$$

where $\dot{r}_p$ is the change rate of the radius of a parent droplet, r_p is the radius of a parent droplet, r_c is the radius of child droplet, and τ_{KH} is breakup time scale, given by:

$$\tau_{KH} = \frac{3.726 C_{KH} \tau_p}{\Lambda_{KH} \Omega_{KH}} \tag{2.12}$$

where Λ_{KH} and Ω_{KH} are the wave length and growth rate of the fastest growing wave. In the region where the distance exceeds *L*, the breakup and the radius change rate is the same as in Eq. (2.11) , except the timescale should be newly modeled by:

$$\tau_{RT} = \frac{C_{RT}}{\Omega_{RT}} \tag{2.13}$$

where C_{RT} is a constant in RT model, Ω_{RT} is the growth rate of the fastest growing wave for RT model, defined by

$$\Omega_{RT} = \sqrt{\frac{2}{3\sqrt{3\sigma}} \frac{\left[\left|\mathbf{F}\right|\left(\rho_l - \rho_g\right)\right]^{1.5}}{\rho_l + \rho_g}} \tag{2.14}$$

where $|\mathbf{F}|$ is the acceleration in the direction of travel.

After the first breakup in spray, droplet collision will simultaneously exist in fuel parcels. Collision model in this dissertation is the classical and simple O'Rourke model [39], in which all the collision is assumed to occur only in the parcels that lie in the same computational cell. In addition, within one computational cell, all the parcels are assumed to be homogeneously distributed.

Another assumption in this collision model is that the collision only happens in one pair of parcels. The process of the parcels collision in this model proceeds as:

1. Computing the collision frequency ν between two parcels by:

$$\nu = \frac{N_2^n}{\forall} \pi \left(r_1^n + r_2^n \right)^2 \left| \mathbf{v}_1 - \mathbf{v}_2 \right| \tag{2.15}$$

where N_2^n is the number of droplets in the parcel that have the smaller radius, $\forall$ is the volume of the computational cell where these parcels lie in.

2. Calculating the probability on the collision between two parcels by a Poisson distribution:

$$P_n = e^{-\bar{n}} \frac{\bar{n}^n}{n!} \tag{2.16}$$

where $\bar{n} = \nu \Delta t$ and Δt is the computational time step.

3. Generating a system random number $\xi \in (0,1)$ and comparing P_n with it to decide whether the collision happens. The basic principle is that if P_n is

smaller than the random number, the collision happens.

2.2 Combustion Modeling

CFD RANS numerical tools nowadays are crucial for engine design due to its low cost and high efficiency. Actually, if looking with a broader point of view, we could see that numerical tools can provide more than just cost-saving in terms of money and time. It could be used for testing some ideas and concepts that are not possible in experiments at the current stage such as the one-injector-two-fuel injection strategy. More significantly, with accurate combustion modeling, numerical simulations of engines provide engine manufacturers better insight about how the combustion occur in the new combustion mode engines. Hence, efforts have been devoted in decades to simulate engine combustion process precisely.

2.2.1 Combustion models in engines

Phenomenological description of combustion process in engines

Based on different fuel intake manners, internal combustion engines organize combustion in different ways. In conventional SI engines, the fuel is premixed with the air before its intake into the combustion chamber, in which the combustion is thus classified into the premixed combustion type. In conventional CI engines, the fuel sprays into the combustion chamber near the top dead center (TDC) and the fuel evaporation, fuel-air mixing process and combustion might happen simultaneously. Therefore, this type of combustion is

categorized into the type of non-premixed combustion. However, with more and more advanced combustion modes (e.g. gasoline direct injection (GDI), PCCI and RCCI) proposed recently, the separation of these two combustion types becomes less and less justified. The more and more ambiguous border between premixed and non-premixed combustion in engine combustion modeling is because that the partially premixed combustion in these new combustion modes requires more universal combustion models.

Treating combustion models in a more specific way, we could analyze the combustion process in engines by the dominant controlling factors in the combustion chamber. As shown in Figure 2.2, still taking the conventional SI engine as an example, the fuel is premixed in the combustion chamber (in simulations, the fuel/air would be assumed to be homogeneous) before ignition occurrence. The homogeneous fuel/air mixture is then ignited by a spark plug and then an unstretched laminar flame front forms, which afterwards evolves to a turbulent flame and propagates into the premixed fuel/air regions in the combustion chamber until that all the fuel or air has been consumed. This combustion manner is called *flame propagation*. If using the same method to analyze conventional CI engines, it is seen that after the fuel spray, with the increase of the pressure and temperature in the combustion chamber during the compression stroke, the fuel ignition is initially controlled by the local thermodynamic condition (i.e., temperature, pressure, equivalence ratio and

residue gas fraction) in the mixture. Once the thermodynamic condition reaches a critical point, the fuel auto-ignites, which we call it *auto-ignition*. However, it should be noted in CI engines, auto-ignition is not the dominant way that controls the combustion. Instead, after auto-ignition happens, a thin reaction zone, where the fuel and air diffuse in and consumed in, has been formed. The flame in this scenario is called *diffusion flame*. The chemical timescale involved in the thin reactive zone is much shorter than the mixing timescale involved in the diffusion of fuel/air towards the flame region, which is the reason why diffusion flame is also a type of mixing-controlled combustion. It is interesting to note that flame propagation is not the only combustion type in the conventional SI engines. Under undesirable combustion with engine knocking, auto-ignition could also exist (i.e., end gas auto-ignition). Based on this analysis, it is seen that a specialized model should only be used to simulate the corresponding flame. For example, combustion models for CDC should compute the species conversion and the heat release both in auto-ignition and diffusion flame and cannot be used for flame propagation modeling. For another example, combustion models only considering flame propagation are not able to model the end-gas auto-ignition thus not able to simulate engine knocking in SI engines.

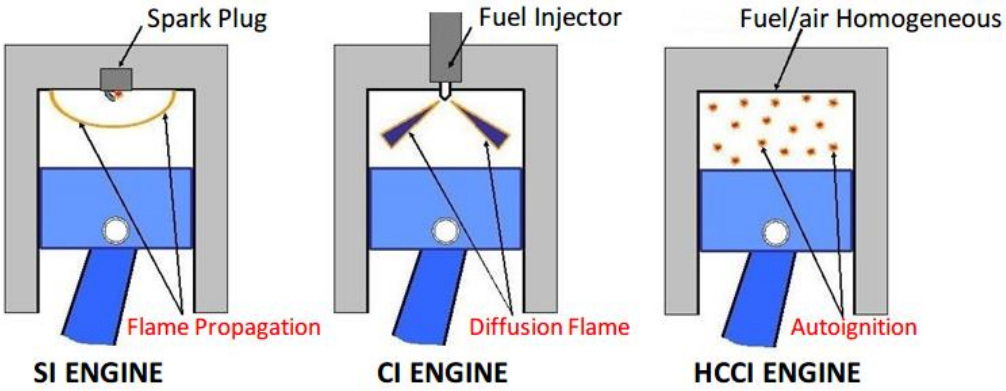

Figure 2.2 Three different types of combustion in three different engines [3]

Using the same way to analyze the combustion in RCCI engine, it yields all the three combustion types in RCCI combustion. As shown in Figure 2.3(a) in normal RCCI combustion, the advanced direct injection with HRF would undergo low combustion and at the end tip of the spray vapor, fuel/air mixing controls the combustion. Meanwhile, the premixed LRF could be consumed by auto-ignition. However, in a small amount pilot injection case (which could be regarded as RCCI in general) as shown in Figure 2.3(b), high temperature flame turning from the quick mixing controlled diffusion flame in the small amount of spray could initialize flame propagation in the LRF/air mixture [42].

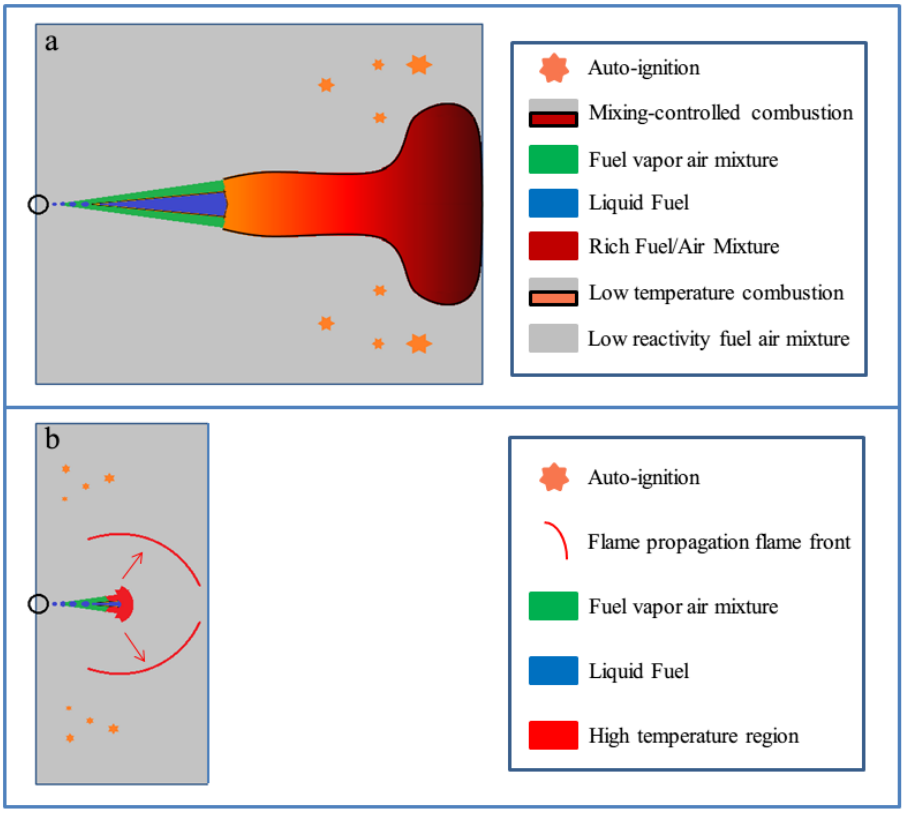

Figure 2.3 Schematic analysis of the combustion in RCCI engines with (a) early direct injection with high percentage of HRF, (b) near-TDC direct injection with small amount of HRF

Hence, in RCCI engines, flame propagation, auto-ignition and diffusion flame might co-exist. From this observation, it is concluded that unified combustion models with seamless switch among three types of combustion are necessary. Before proceeding to unified combustion models development, a review of the basics of combustion models in engines is firstly presented.

CI engines

In CI engines, combustion regimes could be classified into three scenarios: highly stratified combustion (e.g. conventional diesel combustion (CDC)), partially premixed combustion (e.g. PCCI, RCCI) and homogenous premixed

combustion (e.g. HCCI) [24]. Considering the ways of complex chemical-turbulence interactions in these three scenarios, we can also classify them in this way: mixing controlled combustion, multimode combustion and kinetically controlled combustion. In this section, starting from conventional diesel combustion, the basics of CI engine combustion models are reviewed.

In CDC, auto-ignition and diffusion flame coexist, between which, the transition and interaction need to be treated with care. In 1995, Kong et al. [19] proposed an extended combustion characteristic timescale model to account for the correlations between the mixing timescale and chemical timescale. In this model, the auto-ignition was considered by the SHELL model, which is a generic chemical process as:

$$\begin{aligned} &RH + O_2 \rightarrow 2R^* \\ &R^* \rightarrow R^* + P + Heat \\ &R^* \rightarrow R^* + B \\ &R^* \rightarrow R^* + Q \\ &R^* + Q \rightarrow R^* + B \\ &B \rightarrow 2R^* \\ &R^* \rightarrow termination \\ &2R^* \rightarrow termination \end{aligned} \tag{2.17}$$

where RH is the fuel (diesel in a diesel combustion case), R* is the alky radical, P implies the oxidized products including CO, CO_2 and H_2O, B is a branching agent, Q is a labile intermediate species. The first reaction in Eq. (2.17) is an initiation reaction, followed by a chain-propagation cycle of the branching agent B. Finally, the auto-ignition stops with two termination reactions.

Although the goal of this model is aiming at modeling diesel auto-ignition, it is, as a generic mechanism, able to model different type of alkane fuels. In this SHELL model, the formation of the labile intermediate species Q is the most significant due to its leading to the generation of the branching agent B. Hence, tuning the reaction rate of the Q formation reaction is a way to control the hot ignition production, thereby controlling the engine ignition delay. After the auto-ignition modeling by the SHELL model, the CTC model was developed to simulate the diffusion flame in CDC. The assumption in CTC model is that under high temperature conditions, the chemistry in the system tends to be in equilibrium after a certain period of time. Thus in this model, the conversion rate of the partial density for Specie *n* is given by:

$$\frac{dY_n}{dt} = -\frac{Y_n - Y_n^*}{\tau_c} \tag{2.18}$$

where Y_n is the mass fraction of Specie *n*, *Y** is the instantaneous equilibrium value of the mass fraction, τ_c is the characteristics timescale to achieve such an equilibrium state. It is noted that the most critical parameter in Eq. (2.18) to be modelled is the characteristic time-scale τ_c and the instantaneous equilibrium value *Y**.

Typically, the characteristic time is approximately formulated by the sum of the laminar timescale and the turbulent timescale [19], i.e.,

$$\tau_c = \tau_l + f \cdot \tau_t \tag{2.19}$$

where τ_l is the laminar timescale; τ_c is the turbulent timescale; *f* is a delay coefficient that determines the controlling role of the turbulent effects.

In the RNG $k-\varepsilon$ turbulence model [38], the turbulent characteristic timescale is estimated by:

$$\tau_t = C_2 \cdot k / \varepsilon \tag{2.20}$$

where k and ε are calculated in the turbulence model. C_2 is a model constant with a value of 0.1.

This SHELL-CTC model was validated to be efficient and effective for CDC simulations. However, SHELL-CTC, as presented above, only treats the transition between the chemical controlled process (i.e. auto-ignition) and the mixing controlled combustion (i.e. diffusion flame) by an empirical equation, rendering unreliability in the simulations.

In 2000, Chen et al. [43] proposed a two zone flamelet model. It splits one computational cell into two zones: one region with the unmixed fuel and air, the other region with the unburned and well-mixed fuel and air where the fuel will be consumed by flame propagation and auto-ignition. Compared with the SHELL-CTC model that only considers the mixing process by an empirical timescale, this model represents the whole mixing process from the initial mixing to a premixed mixture. Nevertheless, due to the separation of a computational cell, the mixing region and premixed region volume is roughly estimated by the total cell volume and thus not accurate. Hence, the

computation of this model for species fraction, temperature and thermodynamic parameter is not precise enough to accurately capture the unburned gas properties.

After this two-zone model, more rigorous models have been proposed to represent the auto-ignition and diffusion flame in CDC, including the flamelet approach and flame surface density approach. The turbulence flamelet concept was first proposed by Peter [44] and then applied into diesel engine simulations by Pitch et al. [45]. It tabulates the reaction rate for different scalar dissipation rate and then based on the observation of the mixture fraction and scalar dissipation rate, a presumed probability density function (PDF) is applied to estimate the laminar reaction rate integration to get the mean reaction rate. This flamelet model is capable of dealing with finite chemistry rate and local mixture fraction gradients. This original flamelet model has recently been improved by considering several flamelet simultaneously in CFD by [46, 47]. The disadvantage of the flamelet model is that it causes unaffordable computational cost. Moreover, it represents the local diffusion flame by some averaged properties (e.g. averaged species fraction) and thus not accurate. Hence, a conditional moment closure (CMC) model [48], which enhanced the computational accuracy by discretizing the mass fraction and solved the combustion and mixing by the conditioned mass fraction, was proposed. It is also noted that CMC could calculate the flame propagation by adding one

reaction progress dimension in the computation. However, the high accuracy and capability of dealing with flame propagation exasperate the CPU computational overhead.

Another approach called flame surface density model considers only the dimensions of mixing and the dimension of reaction advancement. The evolvement of this flame surface density method is dramatic since it was first proposed in the context of diffusion flames in 1977 [49]. In 1996, Van et al. [29] presented an exact balance equation to calculate the flame surface density, which was then extended to all the related values in diffusion flame by a generalized flame surface density instead of an exact one by Tap et al. [50] in 2004. Another version of flame surface density approaches is the famous extended coherent flame 3 zones (ECFM3Z) model proposed by Colin et al. [51]. By splitting each computational cell into three zones as shown in Figure 2.4 and considering flame propagation from burned gases into unburned gases, autoignition in premixed fuel/air mixture, diffusion flame in mixing fuel/air mixture, this model is capable of computing all of the three combustion types. However, this model is not able to deal with detailed chemistry due to global oxidization reactions used in this model.

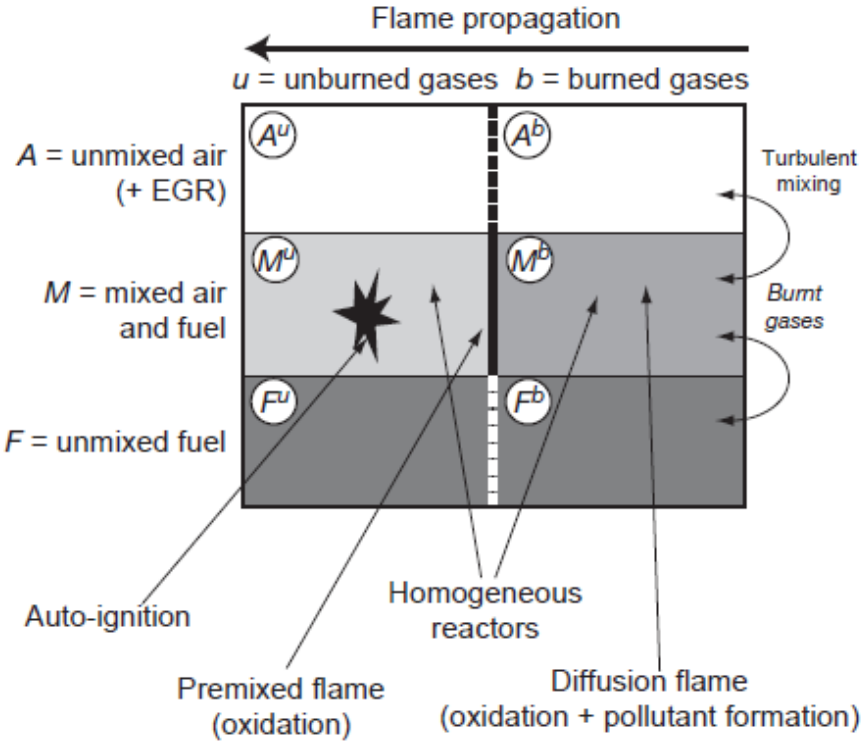

Figure 2.4 Schematic of the extended coherent flame model 3 zone (ECFM3Z) model [51]

This is basically the evolving history of combustion models in CI engines. In sum, in most of the CI engines, regardless of the fact that it is high stratified combustion, partially premixed combustion or homogeneous combustion, it is common to only develop specialized combustion models for auto-ignition and diffusion flame.

SI engines

In SI engines, the first phenomena that should be accounted for is the spark ignition. Fan et al. [52] proposed a discrete particle ignition kernel (DPIK) model and it is widely used in the subsequent SI engine simulations [21, 53-55]. By assuming the flame kernel as a spherical kernel with discrete imaginary particles, DPIK tracks these markers by a transportation equation:

$$D_{kernel} = 2 \cdot \left[\frac{T_{ad}}{T} S_L + \sqrt{\frac{2}{3} k} \right] \cdot (t - t_0) + D_0 \qquad (2.21)$$

where (t-t_0) is the elapsed time from the start of ignition, D_0 is the initial kernel size. The velocities of the particles in a 3-D mesh are given by:

$$\begin{aligned} u_p &= \left[\frac{T_{ad}}{T} S_L + \sqrt{\frac{2}{3} k} \right] \cos(\theta)\cos(\phi) \\ v_p &= \left[\frac{T_{ad}}{T} S_L + \sqrt{\frac{2}{3} k} \right] \cos(\theta)\sin(\phi) \\ w_p &= \left[\frac{T_{ad}}{T} S_L + \sqrt{\frac{2}{3} k} \right] \sin(\theta) \end{aligned} \qquad (2.22)$$

where u, v and w are the velocities in the x, y and z directions, respectively. T_{ad} is the adiabatic flame temperature and T is the estimated local gas temperature. T_{ad}/T accounts for thermal expansion effects. θ and ϕ are random angles which are between $-\frac{\pi}{2} \sim \frac{\pi}{2}$ and $0 \sim 2\pi$, respectively. During the flame kernel expansion process, the reaction rate is calculated by:

$$\frac{d\rho_n}{dt} = -C_w \min\left(\frac{\rho_f}{MW_f C_{sto,f}}, \frac{\rho_{o_2}}{MW_{o_2} C_{sto,o_2}}\right) \cdot \sum S_l MW_n C_{sto,n} \qquad (2.23)$$

where MW_n is the molecular weight of Species n, C_w is set to 80 in order to account for the wrinkling effect, S_l is the laminar flame speed. The ignition kernel will be expanded until it exceeds the integral length scale, where the model will switch to other combustion models to account for flame propagation.

The dominant fuel burning way in SI engines is flame propagation. It means that after the ignition of the fuel, the flame propagates from the burned

fuel into the unburnt fuel/air mixtures and consumes the unburnt. The flame propagation is modeled by Stiech et al. [22] by using the same imaginary maker concepts as in the DPIK. The flame front is represented by Lagrangian markers, whose speed is calculated by the local turbulent flame speed:

$$\frac{S_t}{S_l} = I_0 + I_0^{1/2}\left(\frac{u'}{u'+s_l}\right)^{1/2}\cdot\left(1-\exp\left[-\frac{r_f}{l_I}\right]\right)^{1/2} \cdot\left(1-\exp\left[-\frac{t}{T_{0G}}\right]\right)^{1/2}\cdot\left(\frac{u'}{s_l}\right)^{5/6} \tag{2.24}$$

where S_t is the turbulent flame speed, I_0 is the strain rate, u' is the isotropic turbulence intensity, l_I is the turbulence integral length scale, r_f is the flame radius and T_{0G} is the characteristic time scale, S_l is the laminar lame speed which is calculated by:

$$S_l = (1-2.1R)\cdot(26.32-84.82\cdot[\phi-1.13]^2) \cdot\left(\frac{T_u}{298K}\right)^{2.18-0.8(\phi-1)}\cdot\left(\frac{p}{101.3kPa}\right)^{-0.16+0.22(\phi-1)} \tag{2.25}$$

where R is the residue mass fraction, ϕ is the equivalence ratio.

Then, the heat release in the flame front existing cells is represented by the ratio of local flame area to the overall flame front, assuming that the flame front is a sphere:

$$\frac{dm_f}{dt} = \rho_{f,mix} S_{eff} A_{p,cell} \approx \rho_{f,mix} S_{eff}\, 4\pi r_{p,cell}^{\,2}\cdot\frac{N_{p,cell}}{N_{p,tot}} \tag{2.26}$$

where S_{eff} is the effective flame speed which is related to the turbulent flame speed, $r_{p,cell}$ is the mean distance between the ignition point and the current cell,

$N_{p,cell}$ is the number of imaginary markers in this cell while $N_{p,tot}$ is the total maker numbers. With this equation, the change of the temperature can be calculated by balancing the enthalpies of species formation and destruction.

This Lagrangian model provides a special view to model the flame propagation by imaginary Lagrangian particles and calculate the heat release in the flame front. However, this model is only originally able to account for global reaction mechanisms. In addition, the post-flame-front kinetics has not been considered by this model. More investigations are needed if it is applied into accurate flame propagation modeling.

Another famous flame propagation model is the level-set method G-equation which is first proposed by Peter [56] and implemented into engine CFD code KVIA-3v by Tan et al. [55]. Peter [56] first proposed the flamelet modeling theory and derived a level set equation for a averaged scalar *G* and its fluctuation *G''*. Together with RANS equations and turbulence models in CFD, Tan et al. [55] set the equations to fit in KIVA as:

$$\frac{\partial G}{\partial t} + (\mathbf{v}_f - \mathbf{v}_{vertex}) \cdot \nabla G = \frac{\rho_u}{\rho} S_t |\nabla G| - D_t \kappa |\nabla G| \qquad (2.27)$$

$$\frac{\partial G''}{\partial t} + (\mathbf{v}_f - \mathbf{v}_{vertex}) \cdot \nabla G'' = \nabla_{\|} \left(\frac{\rho_u}{\rho} D_t \nabla_{\|} G'' \right) + 2 D_t (\nabla G'')^2 - c_s \frac{\varepsilon}{k} G'' \qquad (2.28)$$

where $\mathbf{v}_f$ is the vector of fluid velocity, D_t is the turbulent diffusivity, k and ε are the turbulence kinetic energy and dissipation rate from the RNG k-ε turbulence model, *u'* is the turbulence intensity. S_t is the turbulence flame speed

which is calculated by the laminar flame speed S_l, the turbulence integral length l and laminar flame thickness l_f and other modeling constants including a_4, b_1 and b_3:

$$\frac{S_t}{S_l} = 1 - \frac{a_4 b_3^2}{2b_1}\frac{l}{l_f} + \left[\left(\frac{a_4 b_3^2}{2b_1}\frac{l}{l_f}\right)^2 + a_4 b_3^2 \frac{u'l}{S_l l_f}\right] \tag{2.29}$$

By solving the G-equation, it is to be noted that $G=0$ indicates the flame front. In other words, the unburnt and burnt domain is separated by the level set scalar G. The flame front heat release and conversion of Species n are then computed by the ratio of mean flame front area A_f to the cell volume V_{i4}, unburnt mass fraction $Y_{n,u}$ and burned mass fraction $Y_{n,b}$ of Species n by:

$$\frac{d\rho_i}{dt} = \rho\left(Y_{i,u} - Y_{i,b}\right)\frac{A_{f,i4}}{V_{i,4}} S_t \tag{2.30}$$

which is similar to Eq. (2.26) in the Lagranian marker model. Level set G-equation is a more rigorous way to model flame propagation. It is however unable to calculate detailed chemistry because it only considers 7 species including the fuel, O_2, N_2, CO_2, H_2O, CO, H_2. This original version of G-equation model is then improved by Liang et al. [53] by coupling detailed chemistry calculation and adding a CEQ equilibrium solver with the assumption of that the chemistry in the flame front is in equilibrium. This extended model was proved to be accurate for capturing SI engine pressure and heat release rate at different operating conditions. Nevertheless, although the CPU cost of G-equation model has not been discussed in the literatures, it is

believed to be expensive since additive ODEs need to be solved.

New combustion mode engines

HCCI engines drew tremendous attentions of engine researchers due to its tempting high thermal efficiency and near-zero emissions. Thus, modeling HCCI engines is a popular topic in recent years. Fortunately, due to its instinct fuel preparation manner, HCCI combustion is a type of simultaneous premixed auto-ignition inside the combustion chamber, thus not complex to model. It was sometimes even simulated in a 0-D way and acceptable results was obtained as in [57]. The first 3-D detailed chemistry HCCI engine modeling was accomplished by Kong et al. [20], in which, they coupled the chemical solver CHEMKIN-II with KIVA codes and assumed that every computational cell is a closed well-stirred reactor. This way is widely used by the subsequent researchers for auto-ignition modeling in multidimensional engine simulations. Then, this method (CHEMKIN coupled CFD) has been proved that in the two limits of a well-mixed charge (e.g. HCCI) engine, and a well separated charge (e.g. CDC) engine, it works well in predicting both chemistry controlled combustion and mixing controlled combustion [58]. This method is also adopted in this dissertation for combustion modeling between chemistry controlled combustion and mixing controlled combustion, thus will be reviewed in detail here for completeness.

CHEMKIN-II [59] is a chemical kinetics library which is able to handle

the chemical reaction computation. After reading the files that contain the mechanism species and reactions information together with the thermal data and transportation data, CHEMKIN-II uses an integer array, a double precision array and a character array to store all the information into a binary file. Based on the mechanism information in this binary file, CHEMKIN-II provides various subroutines to calculate different parameters including the reaction rate for each species. Specifically, provided that *N* and *I* are the number of species and the number of reactions, respectively in a chemical mechanism, the reactions in this mechanism could generally be expressed as:

$$\sum_{n=1}^{N} \upsilon'_{ni} X_n \Leftrightarrow \sum_{n=1}^{N} \upsilon''_{ni} X_n \qquad (i = 1, ..., I) \tag{2.31}$$

where υ'_{ni} and υ''_{ni} is the forward and reverse stoichiometric coefficients of Species *n* in Reaction i, X_n represents Species *n*.

Thus, the net production rate of Species *n* $\dot{\omega}_n$ can be calculated by:

$$\dot{\omega}_n = \sum_{i=1}^{I} \upsilon_{ni} q_i \qquad (n = 1, .., N) \tag{2.32}$$

where

$$\upsilon_{ni} = \upsilon''_{ni} - \upsilon'_{ni} \tag{2.33}$$

and q_i is the process variable rate of Reaction i which is calculated by:

$$q_i = k_{fi} \prod_{n=1}^{N} [X_n]^{\upsilon'_{ni}} - k_{ri} \prod_{n=1}^{N} [X_n]^{\upsilon''_{ni}} \tag{2.34}$$

where $[X_n]$ is the molar concentration of Species *n*, k_{fi} and k_{ri} are the forward and reverse rate coefficients of Reaction i, which are given by:

$$\begin{aligned} k_{fi} &= P_{dep} A_i T^{\beta_i} \exp\left(\frac{-E_i}{R_c T}\right) \\ k_{ri} &= k_{fi} \cdot K_{ci}^{-1} \\ K_{ci} &= \exp\left(\frac{-\Delta G_i^0}{RT}\right) \cdot \left(\frac{P^0}{RT}\right)^{\nu_{ni}} \\ \Delta G_i^0 &= \sum_n^N (\Delta G_n^0 \cdot \nu_{ni}) \end{aligned} \tag{2.35}$$

where A_i, β_i and E_i are Arrhenius parameters (pre-exponential factor, temperature exponent and activation energy, respectively), which are read from the chemical mechanisms. P_{dep} is the computed coefficient due to the pressure-dependent reactions. K_{ci} is the equilibrium constant of Reaction *i*. ΔG_i^0 and ΔG_n^0 are the standard Gibbs free energy of Reaction *i* and the Gibbs free energy of the formation of Species *n*, respectively.

Hence, based on these calculations, the change in density with known production rate $\dot{\omega}_n$ is built up as:

$$\dot{\rho}_n^C = W_n \dot{\omega}_n \tag{2.36}$$

The chemical heat release can be calculated by:

$$\dot{Q}^C = -\sum_{n=1}^{N} \dot{\omega}_n \left(\Delta h_f^\circ\right)_n \tag{2.37}$$

The above obtained $\dot{\rho}_n^C$ and $\dot{Q}^C$ are the chemistry related source terms in the governing equations, i.e., Eq. (2.1) and Eq. (2.3).

In new combustion modes proposed recently like RCCI, the high reactivity direct-injected fuel could play a role of spark and cause several flame propagations in the low reactivity fuel atmosphere [24]. Under this situation, the omittance of flame propagation consideration in the combustion model could cause unacceptable errors under certain operating conditions of RCCI engines. The review of combustion models in this section reveals that extended combustion models with detailed chemistry and covering all the three combustion types have not been reported. Therefore, unified combustion models with detailed chemistry to model RCCI engine under wide operating conditions are still desirable.

2.2.2 Surrogate chemical mechanisms

Besides of the combustion models to calculate heat release in the simulations, the combustion chemistry is another major concern in combustion modeling. Diesel as HRF and gasoline as LRF is still the most widely and commonly investigated fuel combination in RCCI engines [13]. As a result, compact and reliable chemical mechanism for the chemistry of diesel/gasoline in engine simulations is significant. Nevertheless, conventional fuels such as diesel and gasoline usually contain a large number of components. It is too complex to consider all those components in the combustion chemical process due to their variations depending on fuel's source and production. It is widely accepted to deem iso-octane and n-heptane (primary reference fuels (PRF)) as

surrogate fuels to calculate gasoline and diesel chemical process in engine simulations. Curran et al. [60, 61] developed the detailed n-heptane and iso-octane combustion chemistry. By combining the n-heptane and iso-octane mechanism, a PRF mechanism forms. PRF blends could represent octane number properly from 0-100 by varying the volume ratio of iso-octane. However, due to the huge size (more than 1000 species) of the detailed mechanisms, it is impossible to apply them in a multidimensional CFD engine simulation. Therefore, it is very necessary to develop reduced mechanisms with a suitable size to capture the conventional fuel combustion in these new concept engines.

To develop reduced PRF mechanisms for the use in multidimensional engine simulations, lots of efforts have been made [30, 62-69]. Initially, researchers have been trying to reduce the detailed mechanisms of n-heptane and iso-octane in [60, 61]. Patel et al. [68] developed a reduced n-heptane mechanism from [60] for HCCI diesel engine and validated it in terms of ignition delay and engine combustion characteristics. Jia et al. [62] proposed an iso-octane chemical model reduced from [61] and satisfactorily predicted ignition timing, burning rate and the emission of HC, CO and NO_x in a HCCI engine with gasoline fuel. With the basis of those existing reduced n-heptane and iso-octane mechanisms, researchers tried to develop PRF mechanisms by combining n-heptane and iso-octane mechanisms with considering the

interaction reaction between n-heptane and iso-octane. Tanaka [65] developed a very simple HCCI PRF mechanism with 32 species and 55 reactions in a rapid compression machine (RCM). Although it is compact and could represent HCCI combustion characteristics properly, it omits some significant C1-C6 species and reactions, resulting in short-estimated ignition in shock tube and high-estimated heat release. Based on this compact HCCI PRF mechanism, Tsurushima [66] further modified it into 33 species by adding the reactions of olefins and aldehydes and considering the beta-scission and thermal decomposition of alkyl radicals to ethylene.

These super-compact mechanisms seemed tempting in terms of computational cost. However, these mechanisms omit some concerning properties such as flame speed and intermediate species predictions. To enhance the predictability of PRF mechanisms, Ra et al. [64] developed a PRF mechanism with 41 species and 130 reactions. They developed an iso-octane mechanism using the similar manner in [68] and combined it with the n-heptane mechanism in [68] to get the final PRF mechanism. This mechanism was validated under different conditions in shock tube, HCCI engine and direct injection engine experiments. Nevertheless, this mechanism does not consider the flame speed and intermediate species validation. To enhance the flame speed prediction, Wang et al. [67] proposed a reduced PRF mechanism consisting of 73 species and 296 reactions, which, however, is too large and

computationally expensive for engine CFD computation.

The comparison of the existing PRF mechanisms for predicting the laminar flame speed was summarized in Figure 2.5. As shown, the mechanism of Wang et al. [67] shows a superiority for laminar flame speed calculation. However, it contains too many species and reactions which are computationally unaffordable for CFD engine simulations.

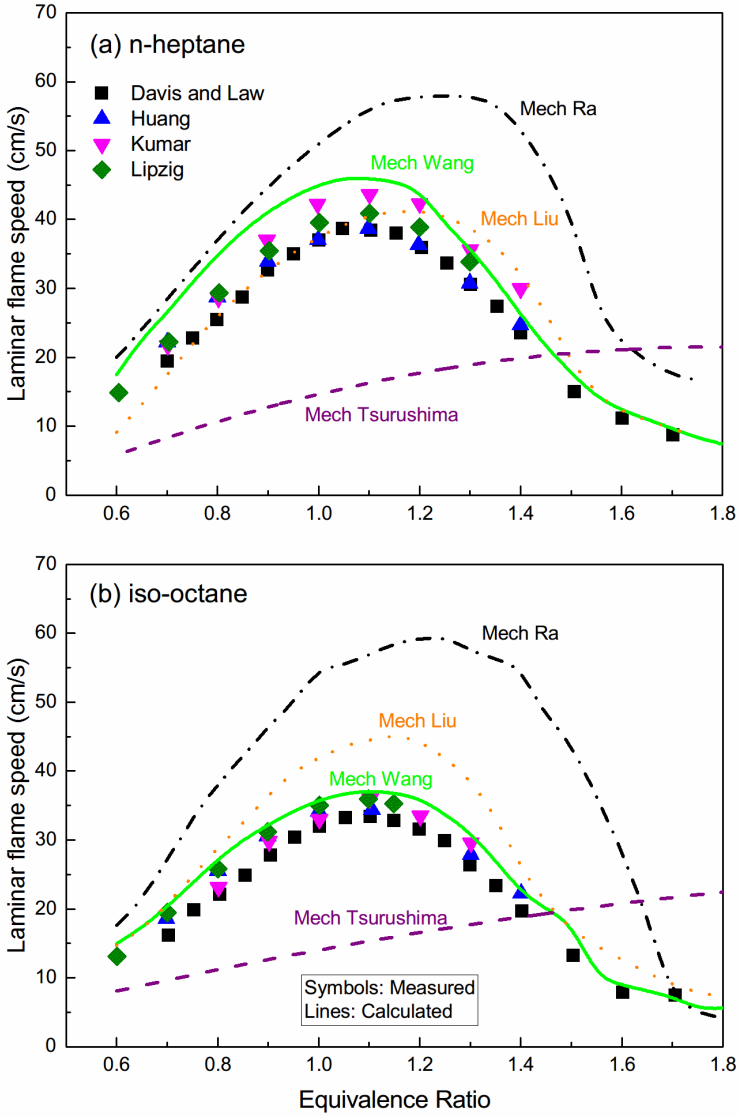

Figure 2.5 Laminar flame speed comparison of (a) n-heptane; (b) iso-octane, among different experimental and calculated results, (Experimental results from Davis and Law [70], Huang [71], Kumar [72] and Lipzig [73]; Chemical mechanisms from Wang [67], Ra [64], Liu [74] and Tsurushima [66])

Another major shortcoming of those PRF mechanisms is that they did not include PAH chemistry, which is considered as the precursors in most of the soot models [75-77]. This could result in failing to predict soot formation. Except for the formation of surface growth species, soot particle nucleation, coagulation and surface growth and oxidation, the formation of soot precursors (PAH) is always covered in the gas-phase reaction mechanism. Hence, a PAH sub-mechanism coupled in a PRF mechanism could provide tremendous convenience for the soot prediction of engine combustion gasoline or diesel.

In sum, the existing reduced/skeletal PRF mechanisms for combustion predictions have their pros and cons. The HCCI oriented PRF mechanisms in [30, 62, 64-66, 68, 69] provide extremely compact model whereas omit some important properties, failing to predict flame speed as well as the intermediate species. Other PRF mechanisms such as [63, 67] provide reliable prediction of various combustion properties and is validated in different combustion devices, but it contains too large amount of species and reactions for multidimensional CFD simulations. More importantly, to the best knowledge of the author, no PRF mechanisms have coupled the PAH reactions to predict soot formation in engine combustion fueled with gasoline and diesel.

Therefore, it is desirable to develop a PRF mechanism with PAH coupled for the simulations of RCCI combustion process with gasoline/diesel with a small size while retaining high prediction capability for some key combustion

characteristics.

2.2.3 Combustion modeling acceleration methods

Another major challenge in multidimensional engine simulations with detailed chemistry is the expensive computational cost. The challenge lies in the fact that the integration of the finite-rate chemistry is extremely computationally expensive due to the stiffness of the chemical source term. Besides the stiffness, realistic detailed chemical mechanisms beyond the simplistic generic mechanism or one-global-reaction mechanism are necessary for a reliable combustion simulation, which even dramatically deteriorate the computational overhead. Consequently, the cost of the chemical source term integration dominates the computational efforts in most reactive flow simulations [78].

Based on the above considerations, to conduct computationally affordable and robust reactive flow simulations, reliable mechanism reduction methods are important. In the past decades, various mechanism reduction methods have been proposed, targeting either the reduction of mechanism size (species number and reaction number) by eliminating the unimportant species and reactions, or the removal of stiffness by separating the chemical timescales of different species. In the first category, the dimension reduction could be achieved by simple Quasi-Steady-State (QSS) and Partial-Equilibrium (PE) approximations [79, 80] or more rigorous methods such as Direct Relation

Graph (DRG) [81-83], DRG with Error Propagation (DRGEP) [84] and DRGEP aided with sensitivity analysis (DRGEPSA) [85]. These methods are able to dramatically reduce the detailed mechanisms with thousands of species to reduced mechanisms with less than one hundred species within acceptable errors. It should, however, be noted that the reduced mechanisms still remain stiff. Other methods like Computational Singular Perturbation (CSP) [86-90] and Intrinsic Low Dimensional Manifold [91] can partly remove the stiffness by reducing the fast variables in the fast modes. However, these methods are computationally expensive especially when being applied on-the-fly, due to the expensive Jacobian matrix decomposition.

Besides mechanism reduction, different mathematical integration schemes have also been used, explicitly or implicitly, to accelerate combustion chemistry integration. Integrating the stiff chemistry is a dilemma for explicit schemes. On one hand, the extremely fast variations of some variables in the chemistry integration lead to severe stability problems when using explicit method with large step size. On the other hand, if guaranteeing the stability, an extremely small step size which must be narrower than the smallest time scale of all species is needed, causing unaffordable computation for reactive flow simulations. Hence, implicit methods such as backward differentiation formulae (BDF) [92] (packages such as DASSL [93], VODE [94]) are widely used in combustion simulations. Based on the solution of the previous step,

these solver packages adaptively modify the current time step and variable-order. However, high order discretization schemes demands the storage of variables' information of several steps before, which undermines its computational speed. Moreover, unlike in the stand-alone chemistry integration without coupling fluid mechanics, reactive simulations require re-initialization of these solvers at each global time step, significantly weakening the efficiencies [95]. In addition, the computational price of Jacobian inversion and decomposition adopted by most implicit solvers is proportional to the cube of species numbers, making it inapplicable into reactive flow simulations with large-scale mechanisms [80]. Therefore, besides the commonly used implicit solvers, some semi implicit-explicit schemes and explicit schemes for stiff chemistry integration have been proposed recently to address the above mentioned problems.

CHEMQ2 [95] is an explicit solver, which uses the QSS method. It employs an explicit predictor step to evaluate the variables in the next time step while a corrector step based on the initial and predicted values is used to check the fidelity of the predicted values. The criterion is that if the error between the predictor and corrector step is within a user defined error tolerance, the predicted values are acceptable. This method is A-stable for linear problems and second-order accurate. Under very stiff point (.i.e. reflective point in autoignition), a very small time-step is still needed considering the fact that this

is still an explicit method. Based on the observation of Shi et al. [96], it can save a lot computational time since only two algebra evaluations are needed during one integration. However, stability and extreme small time step under some conditions makes CHEMQ2 inapplicable under some certain cases [97].

Other methods tend to separate the “fast” species with “slow” species based on their characteristic time scales. The slow variables are integrated typically with explicit method, while the “stiff” variables are dealt with implicit formulation (Newton-iterative) [98] or projection method [78, 99, 100]. Gao et al. [101] applied CSP concept to identify the distinction between fast and slow variables then employed on one hand, a simple forward first-order Euler to integrate the slow variables and on the other hand, a backward first-order Euler scheme to integrate the fast variables. It is shown that this simple method could resolve the error of the splitting schemes. However, this method at its current form is not practical for using in multidimensional reactive flows since it does not formulate time step adaptive techniques and it is generally a first-order accurate scheme. Severe divergence problems could also be encountered in this method under large magnitude of reaction rate conditions (high pressure and high temperature under engine simulation for example).

In view of the above discussions, it is important to propose a robust and efficient integration method for the stiff chemistry in multidimensional reactive flows. Moreover, together with other methods such as storage retrieval method

(e.g., *in situ* adaptive tabulation (ISAT) [102]) which stores the chemical source terms in the process of computing and retrieves them when similar thermochemical conditions are found; parallel computing based on the hardware conditions (e.g., GPU-parallel [96, 103], CPU-parallel); clustering methods where computational cells with same thermochemical conditions are clustered as one to reduce the number of spatial discretization (e.g., chemistry coordinate mapping (CCM) [104] and correlated dynamic adaptive chemistry (CO-DAC) [105]), it is desirable to apply comprehensive methods to reduce computation cost in engine simulations.

2.3 Summary

In this chapter, the basic theory and equations to model RCCI engines were listed, including the governing equations, turbulence models and fuel spray models. The main topic of this dissertation, namely, modeling the combustion process of RCCI engine, is thoroughly reviewed and discussed.

To be summarized, it is seen that there are three main research gaps in RCCI combustion process simulations. Firstly, a more compact and accurate PRF mechanism for gasoline/diesel fuel chemical kinetics in RCCI dual-fuel combustion is needed. Secondly, due to the co-existence of flame propagation, diffusion and auto-ignition in RCCI combustion, a seamless and unified combustion model which is able to cover all these three combustion types is desirable. Finally, advanced schemes to solve the computationally expensive

stiff combustion chemistry in engine simulations are significant for fast and efficient RCCI engine simulations. Hence, in the next chapters, Chapter 3 proposes and validates a PRF mechanism coupled with PAH for combustion and emission formation modeling in RCCI engines. 0 and 0 is focused on developing unified combustion models for RCCI combustion simulations. Chapter 6 is devoted to accelerate the engine combustion simulation computation, including a MPI configuration for chemical solver parallel computing and a heterogeneous multi-scale method for stiff combustion chemistry integration.

Chapter 3 PRF Mechanism Development for RCCI Engine Modeling Fueled with Gasoline and Diesel

3.1 Introduction

To simulate duel fuel gasoline/diesel combustion chemistry in RCCI combustion, a reduced primary reference fuel (PRF) mechanism is indispensable. To achieve this goal, lots of efforts have been made as in ref. [30, 62-69]. However, these mechanisms do not consider flame speed and intermediate species prediction or fail to model PAH in the PRFs combustion for soot prediction in engines. This chapter proposed two reduced PRF mechanisms and one PRF-PAH mechanism for combustion and soot prediction.

During the mechanism formulation process by a semi-empirical methodology, I noted that in the realm of β-scission of free radicals, normal alkane cracks rapidly to form mostly H_2, CH_4 and C2-C4 alkenes [106]. If the cracked products (H_2/CO/C1-C4 hydrocarbon) are considered by a detailed C4 reaction model (base mechanism), may the cracking process from the fuel to C4 radicals be modelled with a simplified model? The answer is yes and this issue has been examined in some researches [106, 107]. This principle has been actually used for reduced mechanism development [108, 109]. A further question would be that is it possible to model the cracked products oxidization by a C3 detailed base mechanism or even lower and simplify the reactions the

fuel cracking process?

Besides of the objective of developing PRF mechanisms for gasoline/diesel chemical reaction modeling in RCCI combustion, this chapter proposed 3 PRF mechanisms to explore this question. Different base mechanisms (C2 and C1) were combined with the simplified models respectively into these two PRF mechanisms. Mechanism 1 (M1) deals with fuel cracking process from fuel to C2 hydrocarbon empirically while Mechanism 2 (M2) empirically treats cracking process from fuel to C1 hydrocarbon. The experimental data of shock tube and laminar flame speed were used as a basis to compare and validate these two mechanisms. In addition, with the purpose of developing a PRF with PAH mechanism, a PAH sub-mechanism was added into M2 to form Mechanism 3 (M3). M3 was further validated with ignition delay, flame speeds, species profiles in RCM, shock tube, premixed flame species, soot formation in constant volume combustion from available experiments in literatures. It was also validated in HCCI, PCCI and RCCI engines.

3.2 Methodology and mechanisms formulation

As discussed in the introduction, this study applied an empirical methodology, which is yet to be proved in this thesis: partial oxidation of fuel to intermediates, which are somewhat larger than CO and H_2 and treated by a detailed reaction mechanism, could be simplified. Obviously, to apply this

methodology, a reliable empirical low chemistry mechanism is crucial. Another significant issue is to choose small fragment reaction models [110, 111], which are believed to be very mature and well-proved. Simulations of shock tube and freely propagating flame in this study were performed by SENKIN [112] and PREMIX [113] code .

3.2.1 M1

The C2 base mechanism was chosen from Aramcomech 1.3 [114]. This mechanism has been developed to describe the oxidation of small hydrocarbons and oxygenated hydrocarbon species. It was validated over a wide range of initial conditions and experimental devices and provides accurate predictions for saturate and unsaturated hydrocarbons including methane, ethane, ethylene, acetylene and oxygenated species including formaldehyde, methanol, acetaldehyde and ethanol. A lumped low-temperature PRF oxidation model was appended to capture the low-to-intermediate temperature combustion. This low-temperature pathway was adopted by most of the PRF mechanisms [30, 62-69], which is described as below:

$$\begin{aligned} &RH + O_2 = R + HO_2 \\ &R + O_2 = RO_2 \\ &RO_2 = QOOH \\ &QOOH + O_2 = O_2QOOH \\ &O_2QOOH => OH + KETO \end{aligned} \tag{3.1}$$

where R denotes alkyl radical (C_nH_{2n+1} structure), Q denotes C_nH_{2n} structure, RO_2 denotes alkylperoxy radical, QOOH denotes hydroperoxyalkyl radical,

O_2QOOH denotes peroxyketohydroperoxide. The rate coefficients in this study were based on Tsurushima model [66], necessary rate adjustment was made for ignition delay prediction as listed in Table 3.1. The rate adjustment methodology as introduced by Ra and Reitz [64] was used here for the rate adjustments in Table 3.1. As pointed out in [60, 64], H abstraction of fuel with O_2 and OH significantly affect the ignition delay in low-intermediate temperature region. Hence, in order to obviously show the negative temperature coefficient (NTC) phenomenon and match the experimental data, the H abstraction of fuel with O_2 was dramatically adjusted by a factor of 7, leading to a 7.00^{16} cm^3/mol/s reaction rate factor, which might be a bit too high for a bimolecular reaction. Hence, it should be noted that the arbitrary reaction rate adjustment in [64] should be applied with special care.

Table 3.1 Rate adjustments of M1 from the original Tsurushima model

Reactions	Original	Adjusted
$C_7H_{16}+O_2=C_7H_{15}+HO_2$	1.000E+16	7.00E+16
$C_7H_{16}+OH=C_7H_{15}+H_2O$	6.000E+14	0.35E+14
$C_7H_{15}+O2=C_7H_{15}O_2$	1.000E+12	2.20E+12
$C_7H_{15}O_2=C_7H_{14}OOH$	1.510E+11	2.20E+11
$C_7H_{14}OOH+O_2=O_2C_7H_{14}OOH$	3.160E+11	2.36E+11
$O_2C_7H_{14}OOH=>C_7KET+OH$	8.910E+10	1.25E+10
$C_7KET=>C_5H_{11}CO+CH_2O+OH$	3.980E+15	9.00E+15
$C_8H_{18}+O_2=C_8H_{17}+HO_2$	1.000E+16	7.00E+16
$C_8H_{18}+OH=C_8H_{17}+H_2O$	6.000E+13	1.00E+13
$C_8H_{17}+O_2=C_8H_{17}O_2$	1.000E+12	2.20E+12
$C_8H_{17}O_2=C_8H_{16}OOH$	1.510E+11	2.20E+11
$C_8H16OOH+O_2=O2C_8H_{16}OOH$	3.160E+11	1.58E+11
$O_2C_8H_{16}OOH=>C_8KET+OH$	8.910E+10	2.90E+10
$C_8KET=>C_6H_{13}CO+CH_2O+OH$	3.980E+15	3.00E+15

A set of reactions to model the high temperature pyrolysis and oxidation of n-heptane and iso-octane were added into the base mechanism. As listed in Table 3.2, the cracking process from fuel to C2 in M1 was covered by 18 reactions, including H atom abstraction from n-heptane, iso-octane and small alkyl radicals by O_2, H and OH; β-scission of C7 and C8 alkyl radicals to small olefins and lower alkyl radicals; decomposition of peroxyketohydroperoxide to R'CO radicals; β-scission of R'CO radicals to small olefins and CO. The settlement of this process was based on the mechanism from the model in [67]. C_3H_7 decomposes to C_2H_4, CH_3 and C_3H_6. H abstraction of C_3H_6 was initialized by CH_3.The C3 level reactions were also covered by other C_3H_3, C_3H_4 reactions.

All the reaction rates in Table 3.2 are from the original mechanisms. Some modifications were conducted to maintain a reduced fuel pyrolysis size as well as kinetically accuracy:

(a). According to Curran et al. [60], β-scission was adopt for the R'CO cracking pathway: R'CO => small olefin + small alkyl radical + CO instead of R'CO + O_2 => small olefins + CO + HO_2 in Tsurushima model [66]. The small olefin here is C_2H_4.

(b). The mechanism in [67] was reduced from a detailed gasoline surrogate mechanism [61] by the automatic method of DRGEP, leaving many isomers in C2-C3 species. Hence, the isomers of C_3H_7 in reactions were reduced by isomer lumping to: $C_3H_7 = C_2H_4 + CH_3$, $C_3H_7 = C_3H_6 + H$.

The final M1 consists of 51 species and 225 reactions.

Table 3.2 Fuel cracking reaction for M1 and M2

M1 fuel cracking process	M2 additional C2 cracking reactions
$C5H_{11}CO = C_2H_4 + C_3H_7 + CO$	$C_2H_5 + O_2 = C_2H_4 + HO_2$
$C_7H_{15} => C_2H_5 + C_2H_4 + C_3H_6$	$C_2H_4 + OH = CH_2O + CH_3$
$C_6H_{13}CO => C_4H_9 + C_2H_4 + CO$	$C_2H_4 + OH = C_2H_3 + H_2O$
$C_4H_9 => C_3H_6 + CH_3$	$C_2H_3 + O_2 = CH_2O + HCO$
$C_8H_{17} => C_3H_7 + C_3H_6 + C_2H_4$	$C_2H_3 + HCO = C_2H_4 + CO$
$C_3H_7 = C_2H_4 + CH_3$	$C_3H_5 = C_2H_2 + CH_3$
$C_3H_7 = C_3H_6 + H$	$C_2H_4(+M) = C_2H_2 + H_2(+M)$
$C_3H_6 = C_2H_3 + CH_3$	$C_2H_3 + O2 = C_2H_2 + HO_2$
$C_3H_6 + CH_3 = C_3H_5 + CH_4$	$C_2H_3 + H = C_2H_2 + H_2$
$C_3H_5 + O_2 = C_3H_4 + HO_2$	$C_2H_2 + H(+M) = C_2H_3(+M)$
$C_3H_4 + OH = C_2H_3 + CH_2O$	$C_2H_2 + O_2 = HCCO + OH$
$C_3H_4 + OH = C_2H_4 + HCO$	$C_2H_2 + O = HCCO + H$
$C_3H_4 + OH = C_3H_3 + H_2O$	$C_2H_2 + OH = CH_2CO + H$
$C_3H_3 + H(+M) = C_3H_4(+M)$	$CH_2CO + H = CH_3 + CO$
$C_3H_3 + HO_2 = C_3H_4 + O_2$	$CH_2CO + O = HCCO + OH$
$C_3H_3 + O_2 = CH_2CO + HCO$	$CH_2CO + OH = HCCO + H_2O$
$C_3H_3 + HCO = C_3H_4 + CO$	$CH_2CO + H = HCCO + H_2$
$C_3H_3 + HO_2 = OH + CO + C_2H_3$	$HCCO + OH = HCO + HCO$
	$HCCO + O = H + CO + CO$
	$HCCO + O_2 = CO_2 + HCO$

3.2.2 M2

For the more reduced M2 mechanism, the base H_2/CO/C1 mechanism from Li et .al [111] was used as the core mechanism. This mechanism was validated by comparing against a wide range of experimental conditions for laminar premixed flame speed, shock tube ignition delay data at each level of hierarchical development.

The high temperature pyrolysis from fuel to C2 was kept the same as M1.

The additional fuel cracking from C2 to C1 was constructed as listed in Table 3.2. Considering the later PAH formation in M3, the C2 radicals' settlements are vital because acetylene is considered as a significant intermediate. These reactions were also selected from the mechanism in [61]. The final M2 consists of 43 species, 144 reactions.

3.2.3 M3

M3 was formulated by M2 with a PAH sub-mechanism. The reactions involving PAH formation are basically from the mechanism of [76, 115], which were reduced from the model of Wang and Frenklach [116]. This PAH mechanism consists of a serial of elementary reactions leading from acetylene and hydrogen to the formation of the first aromatic ring, A_1. It was widely validated with C_2H_2, A_1, A_2 also other PAH formation species including C_3H_3, C_4H_2 and widely accepted. In this mechanism, acetylene, product of the fuel, reacts with C_2H_2 or C_2H_1 to evolve to diacetylene (C_4H_2). The continuous reaction propagation would form polyenes. Also, acetylene reacts with C_4H_3 or C_4H_5 to yield benzene and the first ring hydrocarbons. The successive H and C_2H_2 addition (hydrogen abstraction-C_2H_2 addition (HACA) growth) could form higher order aromatics. The general reaction path could be presented as:

$$\begin{aligned} &A_i + H \rightarrow A_i^{\bullet} + H_2 \\ &A_i^{\bullet} + C_2H_2 \rightarrow A_i^{\bullet}C_2H_2 \\ &A_i^{\bullet}C_2H_2 + H \rightarrow A_i^{\bullet}C_2H + H_2 \\ &A_i^{\bullet}C_2H + C_2H_2 \rightarrow A_{i+1} \end{aligned} \tag{3.2}$$

where A_{i+1} is a higher ring, $\cdot$ labels the corresponding radical. In this study, the aromatics formation reactions stop at C_6H_2 (long-chain acetylene) and A_2R_5 (acenaphtylene), via which, the inception process forms soot. The final M3 contains 72 species and 225 reactions.

The NO_x sub-model that coupled into M3 for engine NO_x emission prediction was from [117]. Thermal NO formation is accounted for by the extended Zeldovich mechanism. In addition, N_2O to NO branch and NO to NO_2 branch are also covered in this NO_x mechanism. The detailed NO_x mechanism and their reaction Arrhenius constants could be found in [117].

After the settlements for all the sub-models and reactions, the reaction rate adjustment methods of Ra et al. [64] was used to modify the reaction rates mainly on n-heptane and iso-octane reactions to maintain reliable flame speed. M1 and M2 were validated by ignition delay and laminar flame speed to explore the question proposed in the introduction. With this preliminary proving, M3 was formulated and further validated in premixed flames, constant volume combustion and RCCI engines.

3.3 Validation of M1 and M2

3.3.1 Ignition Delay

Ignition delay is a fundamental characteristic of fuel combustion. The predicted ignition delays by M1 and M2 were compared to the experimental results. The current validation is taking available experimental results in shock

tube from the literatures by Fieweger et al. [118] for PRF mixtures. Figure 3.1 depicts the comparison of ignition delay of M1 and M2 between the experimental results [118] and the calculated ignition delays at initial pressure of 40 bar and equivalence ratio of 1.0 for different PRF mixtures. As exhibited, for different PRF mixtures from PRF0 to PRF 100, both M1 and M2 mechanism predict well. The NTC phenomenon, which is determined by the low-to-intermediate-temperature chemistry, is satisfactorily reproduced as well.

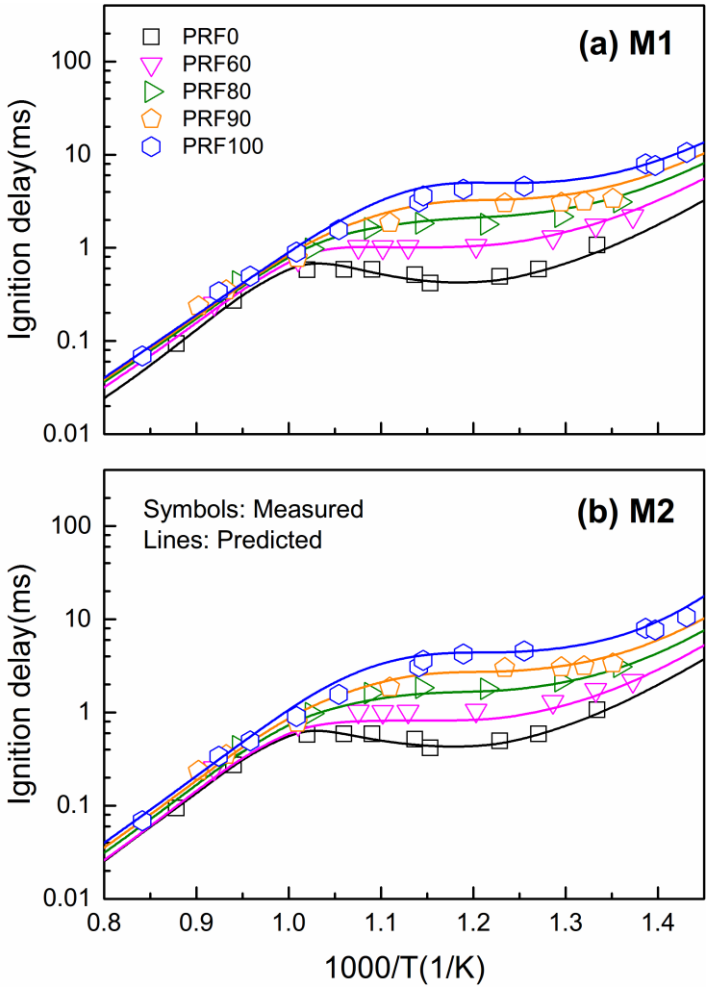

Figure 3.1 Comparisons between the measured [118, 119] ignition delays and predicted ignition delays of PRFs at initial pressure of 40 bar and equivalence ratio of 1.0. The predicted ignition delays are calcualted by (a) M1, (b) M2

To further examine the capabilities of both M1 and M2 on predicting

ignition delays under different conditions, the ignition delays under different pressures and lean, stoichiometric and rich equivalence ratios for pure n-heptane and iso-octane were also compared between the experimental and predicted results. Figure 3.2 shows the comparison results between the experiments and calculations for n-heptane and iso-octane from 3.2 bar to 45 bar. As shown, for all the wide pressure ranges, the calculated results from M1 and M2 reproduce the measured results well. Figure 3.3 shows the ignition delay comparison at lean, stoichiometric and rich n-heptane and iso-octane conditions between measured [119] and calculated results for both M1 and M2. As shown, this PRF mechanism predicts the ignition delay consistently with the experimental results from the shock tube at different equivalence ratios. It is noted that M2 over-predicted the ignition delay for the n-heptane at equivalence ratio of 1.5. This discrepancy at rich atmosphere (equivalence ratio 1.5) would be attributed to the omitted reaction paths of high carbon radical decompositions. Nevertheless, the error at this case between the predicated and measured data is less than 5%, which is acceptable. Therefore, the ignition delay predicted by both M1 and M2 satisfactorily agrees with the experimental results from the literatures at different conditions.

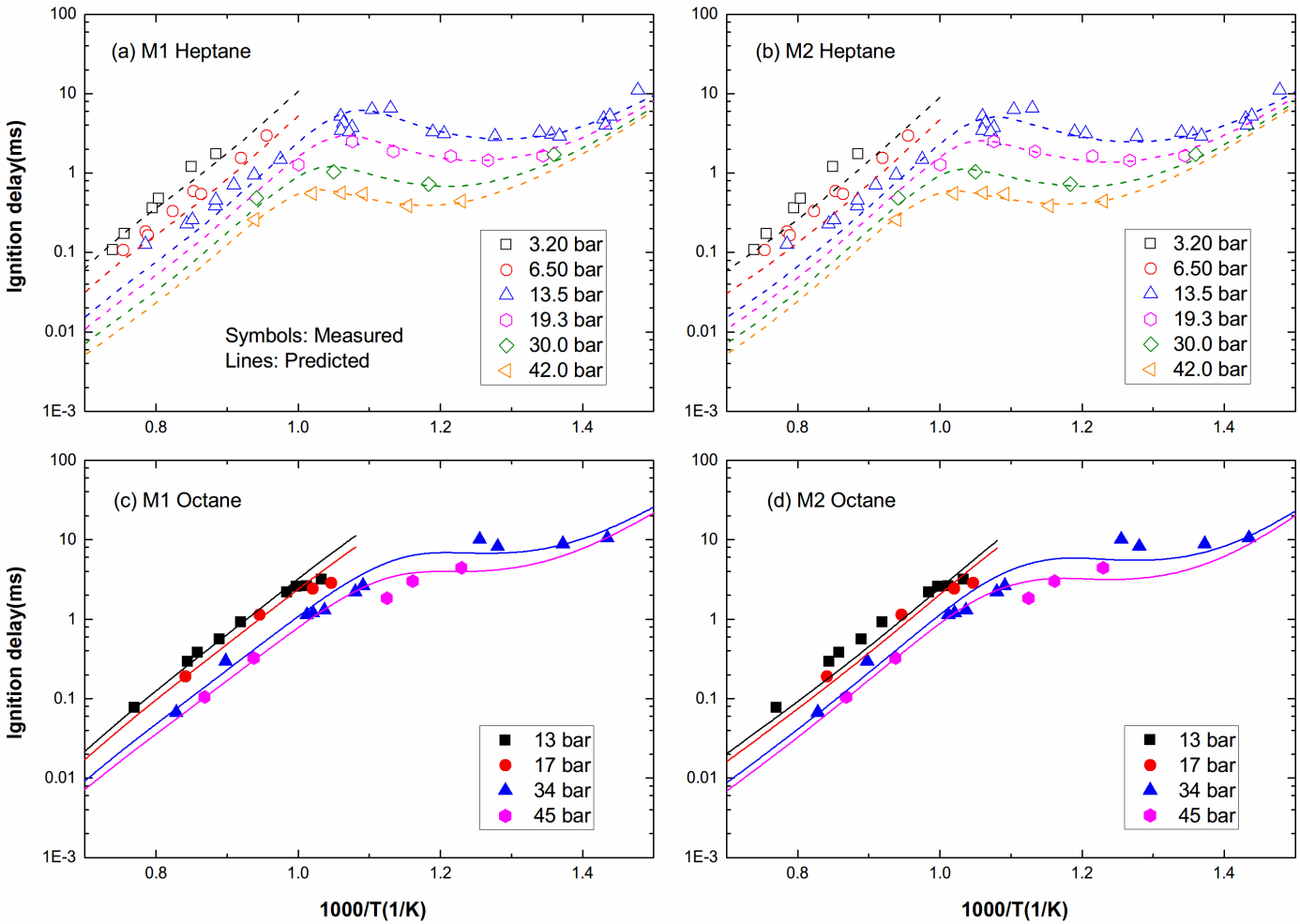

Figure 3.2 Comparison of the measured [118] ignition delay as a function of the initial temperature with the calculated ignition delay predicted by (a) M1 with n-heptane, (b) M2 with n-heptane, (c) M1 with iso-octane, (d) M2 with iso-octane under various initial pressures (equivalence ratio 1.0)

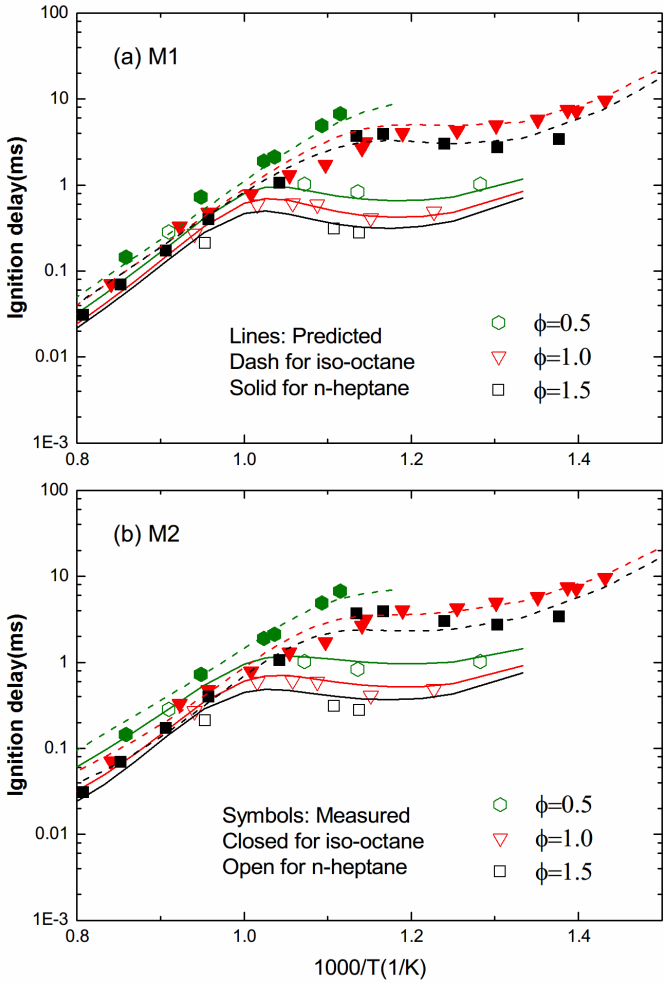

Figure 3.3 Comparison of the measured [119] ignition delay as a function of the initial temperature with the calculated ignition delay predicted by (a) M1, (b) M2 under different equivalence ratios (initial pressure 40 bar)

3.3.2 Laminar Flame Speed

This study conducted a thorough validation for laminar flame speed (LFS) under different unburnt gas temperatures to check the capability of laminar flame speed prediction for both M1 and M2. Calculations were conducted at the same conditions as the experimental ones [120]. The comparison in Figure 3.4 shows acceptable results for the laminar flame speed prediction. It is interesting to note that the general prediction capability of M1 is better than M2, attributing to more omittance of C2-C1 radicals in M2.

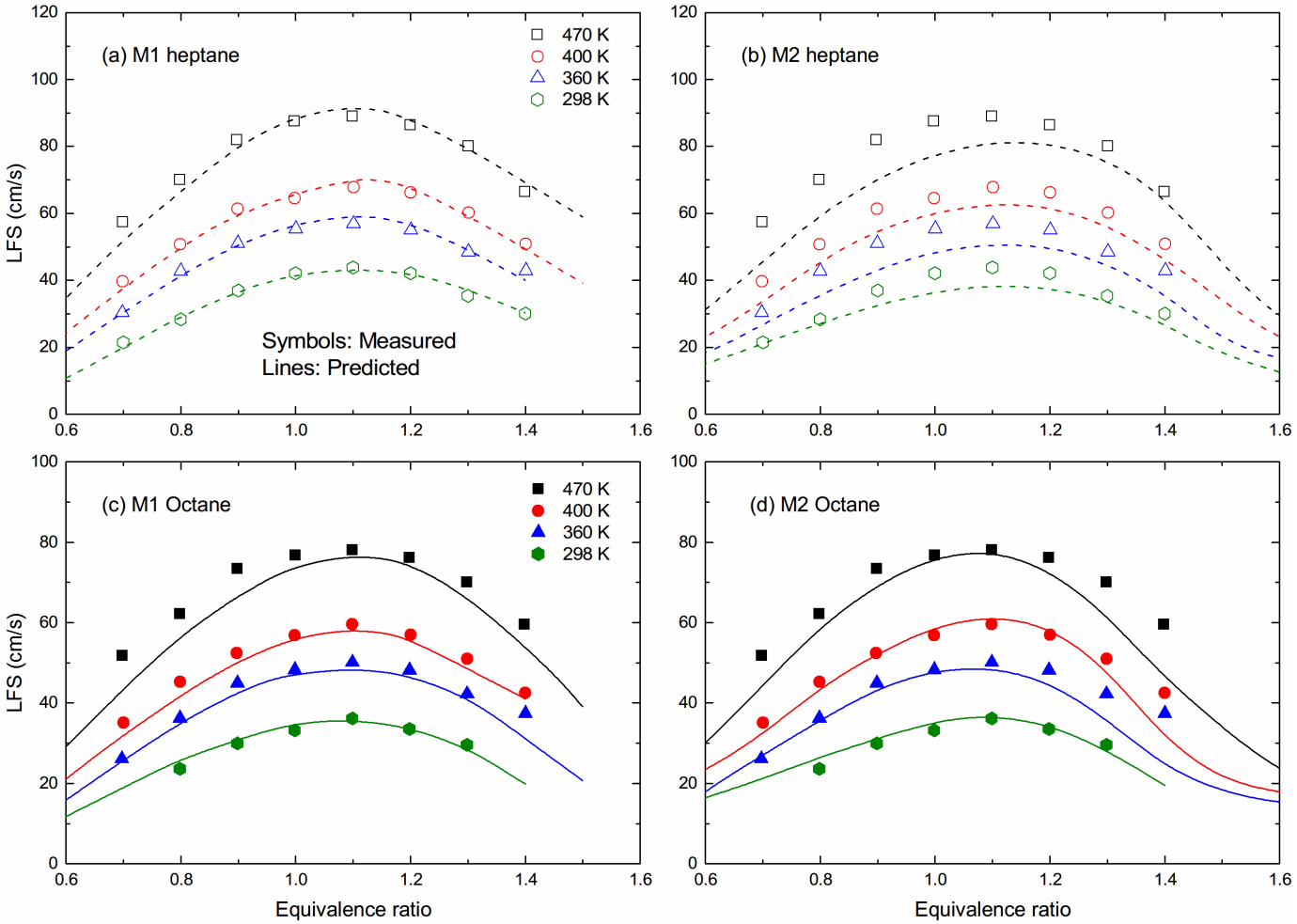

Figure 3.4 Comparison of the Measured [120] and predicted laminar flame speed as an function of equivalence ratio, predicted with (a) M1 for n-heptane; (b) M2 for n-heptane; (c) M1 for iso-octane; (d) M2 for iso-octane under different temperatures (initial pressure 1 atm)

The preliminary validation of M1 and M2 provides a basic proof that the empirical methodology that treats cracking process from fuel to C1 or C2 is reliable to develop reduced mechanism. Further proof could be provided by validating M3 with the experimental data in premix flames, jet stirred reactor (JSR), constant volume combustion (CVC) and engines.

3.4 Validation of M3

3.4.1 JSR

M3 was further validated in JSR by comparing the species profile with the experimental concentrations from [121, 122], for n-heptane, iso-octane and PRF50. The operating conditions in the simulation and experiment are as shown in the figure captions. As shown in Figure 3.5(a-c), the fuels (n-heptane, iso-octane and PRF50) and oxidizer show a satisfactory prediction compared with species profile in experiment. For CO, CO_2, it is also observed that good consistency between the measured and calculated species profile in terms of temperature. It is interesting to be noted that the CO profile underestimation and CO_2 over-prediction above 1000K implies a higher rate from CO to CO_2 in the model at high temperature which was also observed in other PRF mechanisms [63, 67]. This might be attributed to the omitted reaction path of large molecules decomposition due to the highly simplified fuel cracking [63]. Hence, it is important to point out that simplified fuel cracking to C1 level (which was adopted in M2 and M3 in this study) should be applied with care for developing

mechanism with particular target for intermediate CO and CO_2 predictions. In addition, it is important to note the discrepancy of the O_2 prediction between the predicted and measured data below 750K in Figure 3.5(a). As stated in experimental observations in [121, 122], the combustion below 750K is within low-temperature combustion regime, in which a minor oxidizer and fuel consumption could be observed. Hence, the over-prediction of O2 might be due to a slow reaction rate estimation of n-heptane in the negative temperature coefficient region in the current mechanism.

(a) n-heptane

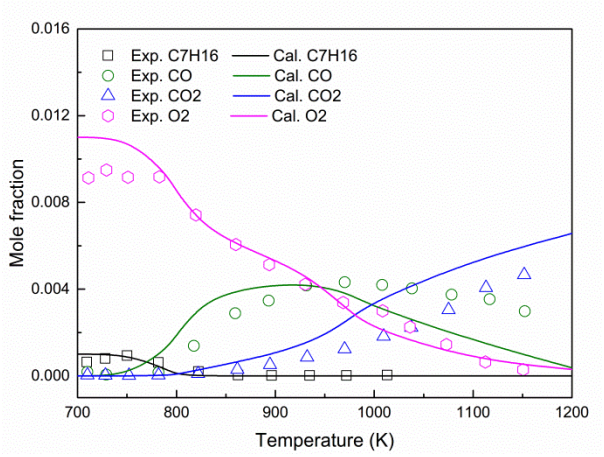

(b) PRF50

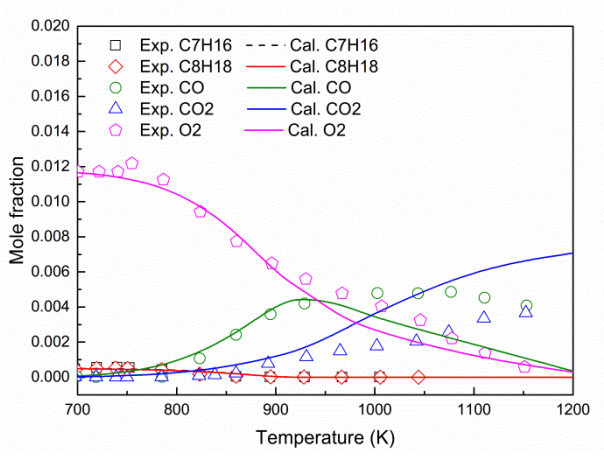

(c) iso-octane

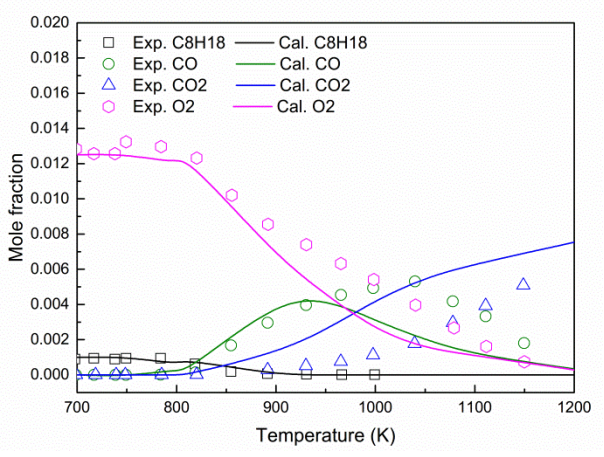

Figure 3.5 Measured [121, 122] and predicted intermediate species profile as a function of temperatures for (a) n-heptane; (b) PRF50; (c) iso-octane. 0.1% fuel; equivalence ratio 1.0; residence time 1s; pressure 10atm

3.4.2 Premixed flame species

In this section, the flame species profiles calculated from the present mechanism were compared with the experimental results from the literatures.

The present model involving PRF fuel and PAH mechanism need to be examined carefully with the flame species profile including PRF oxidation species (CO, O_2, fuel) and PAH related species (C_2H_2, C_2H_4, A_1). The temperature files above the premixed burner for the calculations were adopted from the experiments [123, 124] (at atmospheric pressure and rich fuel (equivalence ratio 1.9)). All the calculations were conducted in PREMIX in the CHEMKIN-II code.

The species in the n-heptane premixed flame at atmospheric pressure and rich fuel (equivalence ratio 1.9) were predicted by the present mechanism, which were compared with the experimental results in Figure 3.6(a and c),. Among the compared species, O_2 and n-heptane are the reactants; CO is regarded as a significant intermediate species in heat release and also the uncompleted products. For PAH related species, C_2H_2 and C_2H_4 are vital in building the first single aromatic ring; A_1 is the first aromatic ring. As seen in Figure 3.6(a and c), the species (fuel related and PAH) profile in terms of height above burner is well captured by the prediction. However, some discrepancy was still observed such as the underestimation with a factor of 1.3 of O2 near the burner surface. This might be due to the over-prediction of fuel auto-ignition at the burner surface in the current mechanism. Nevertheless, differences between the predicted and measured data within a factor of 2-3 are considered to be acceptable in this study because as pointed out by Sarathy et al. [125], the

detailed chemical mechanism could show a maximum error with a factor of 3 in the premixed flame and most species in experiment exhibit experimental errors around a factor of 2. Hence, it is acceptable to conclude that our simulation results show good agreement with the available experimental data. Bakali et al. [123] also tested the species evolution above the burner in iso-octane premixed flame. The comparison was shown in Figure 3.6(b and d). It is also observed that there are some discrepancies among the PAH related species. Considering the high uncertainty of the PAH species measurements and the highly reduced mechanism, the predicted results are also considered to be trustworthy.

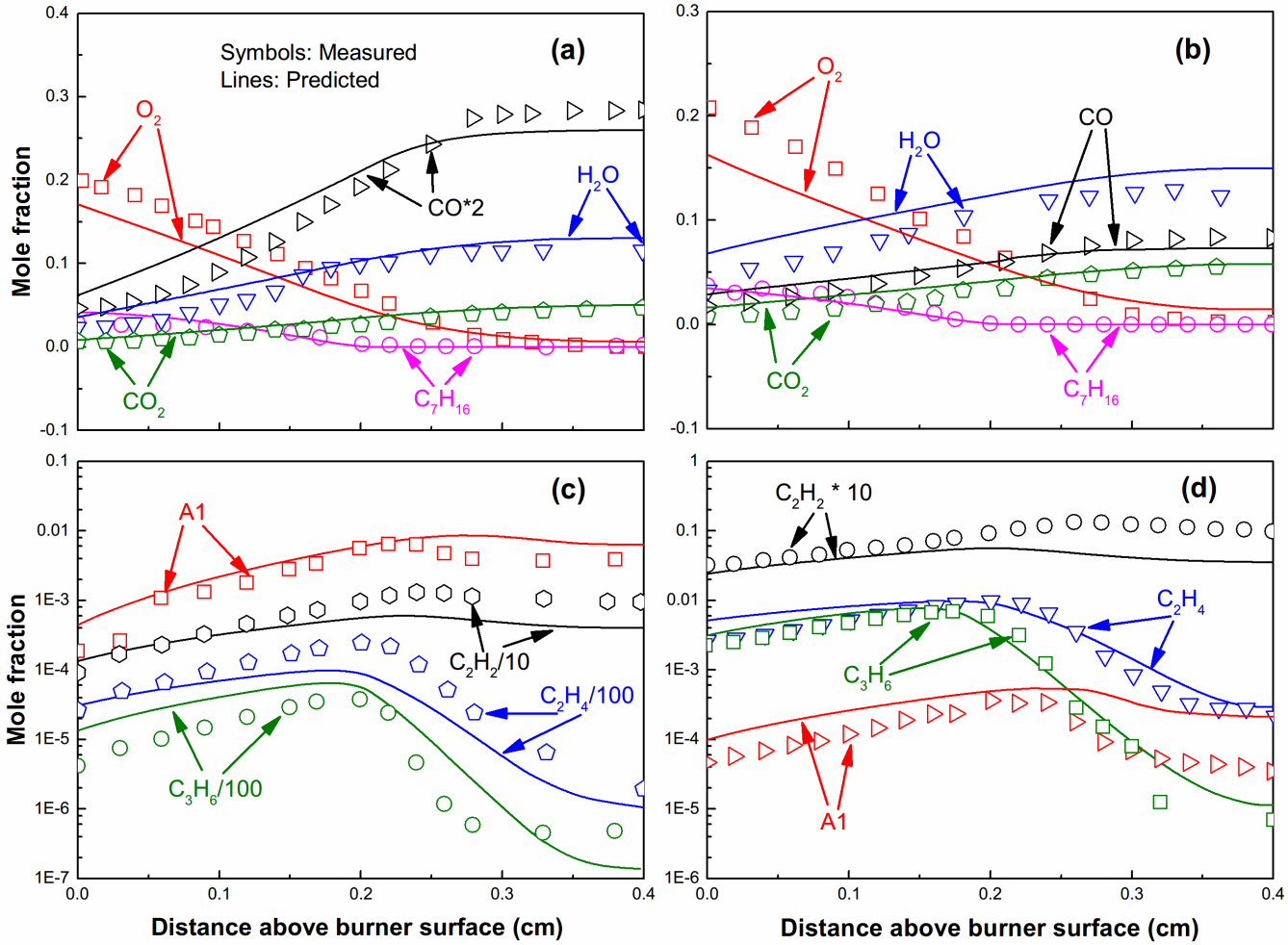

Figure 3.6 Measured [124] and predicted intermediate species evolution as a function of distance above burner surface for (a) fuel related species in n-heptane; (b) fuel related species in iso-octane; (c) PAH species in n-heptane; (d) PAH species in iso-octane flames

3.4.3 CVC

To validate the soot formation prediction of M3, the CVC combustion was conducted. A soot model from Golovitchev and Tao [76, 115] was applied. In the present soot model, we assumed the soot formation via "graphitization" processes:

$$\begin{aligned} C_6H_2 &\rightarrow H_2 + C(s) \\ A_2R_5 &\rightarrow 4H_2 + 12C(s) \end{aligned} \tag{3.3}$$

To validate the soot prediction fidelity of M3, the CVC experiment data from Sandia [126] were adopted. In this study, the CVC was simulated by KIVA-4 code with KH-RT hybrid break-up model [127].

A 2D axisymmetric mesh with 13544 cells was created for the Sandia CVC chamber, as shown in Figure 3.7(a). In the simulation, a typical ambient temperature of 1000 K was chosen for the simulation. Other parameters in the simulation were accordingly kept the same as in the experiments [126]. In spray combustion, the lift-off length, which decides the air entrance and equivalence ratio, could significantly influence the soot formation [128]. Therefore, the lift-off length prediction was firstly tested in this study. In the simulations, the lift-off length was defined as the distance from the first spray axial location to the position where the average OH mass fraction reaching 1% of maximum OH mass fraction during a period of injection interval.

(a) Constant volume chamber 2D

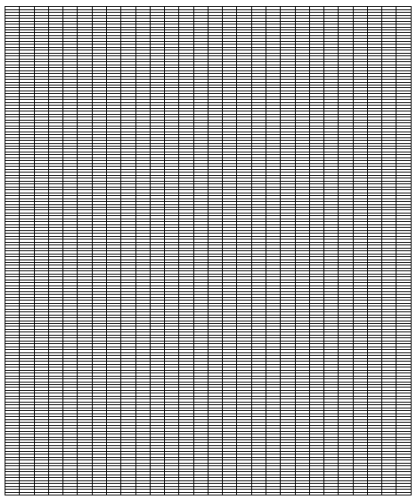

(b) Cummins diesel engine

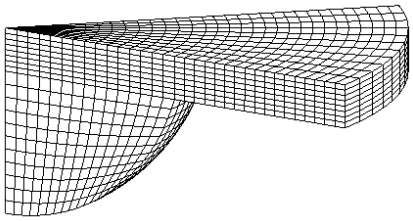

(c) Sandia GM engine

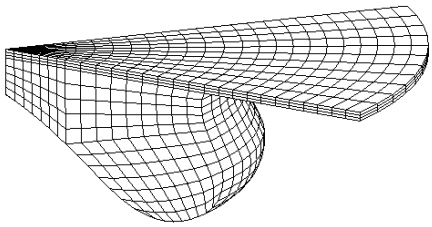

(d) GW4D20 diesel engine

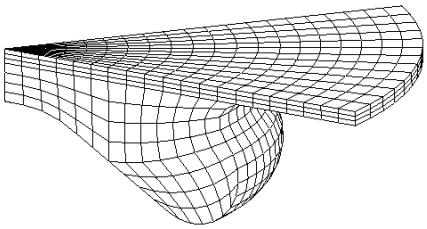

Figure 3.7 Computational meshes for (a) constant volume combustion; (b) PRF HCCI engine; (c) PRF PCCI engine; (d) gasoline/diesel RCCI engine at TDC

Before the combustion simulation, a spray validation was conducted to ensure that the spray in the CVC could properly capture the spray features in the experiment. The liquid length and jet penetration calculated from the simulation were compared with the experimental data. During this procedure, a trial-error method was applied by adjusting the arbitrary constants in KH-RT break-up

model (including B_1, C_τ and Cr_τ) [129] until a good agreement was accomplished between the simulation and experiment. The comparison results are shown in Figure 3.8(a). It is seen that the spray features in the simulation reproduce the experimental data well.

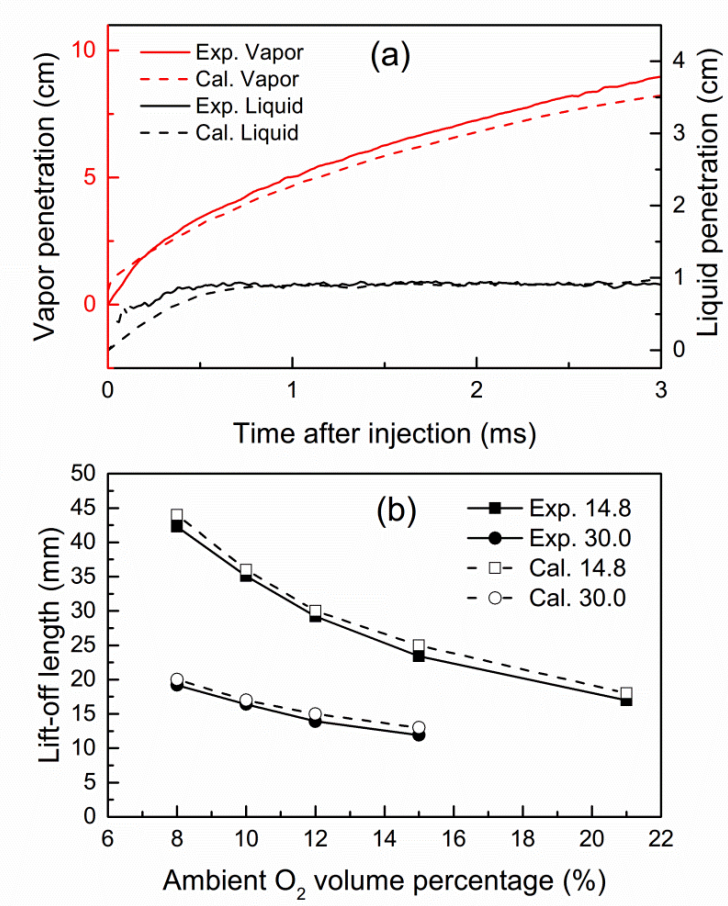

Figure 3.8 Comparison of (a) vapor and liquid penetration profile; (b) lift-off length, between the experiment and simulation

After the spray validation, the lift-off length of two different ambient density 14.8kg/m^3 and 30.0kg/m^3 was compared under different ambient O_2 volumes. As shown in Figure 3.8(b), it is observed that all the experimental lift-off length values with different ambient O_2 volume were predicted well by the simulation.

The spatial soot distribution comparison under the conditions in Table 3.3 are shown in Figure 3.9, in which the upper row is the experimental results while the bottom one are the simulation results. It can be seen that the soot formation regions during the spray are well replicated by the simulation. It is observed that with the increase of ambient O_2 volume, the soot formation regions move downward of the spray, which is similar to the lift-off length. As for the difference between the experiments and simulations, considering the reduced PAH mechanism, which considers soot formation via inception with A_2 and C_2H_6, the general results are satisfactory and this mechanism is believed to be reasonable for predicting soot emission in combustion.

Table 3.3 operating coditions in constant volume combustion (n-heptane injection duration 6.8ms)

	Ambient composition (vol. %)				Ambient density (kg/m^3)
case	O2	N2	CO2	H2O	
1	0	89.71	6.52	3.77	14.8
2	8	81.95	6.36	3.69	
3	10	80.01	6.32	3.67	
4	12	78.06	6.28	3.65	
5	15	75.15	6.23	3.62	
6	21	69.33	6.11	3.56	
7	8	81.95	6.36	3.69	30.0
8	10	80.01	6.32	3.67	
9	12	78.06	6.28	3.65	
10	15	75.15	6.23	3.62	

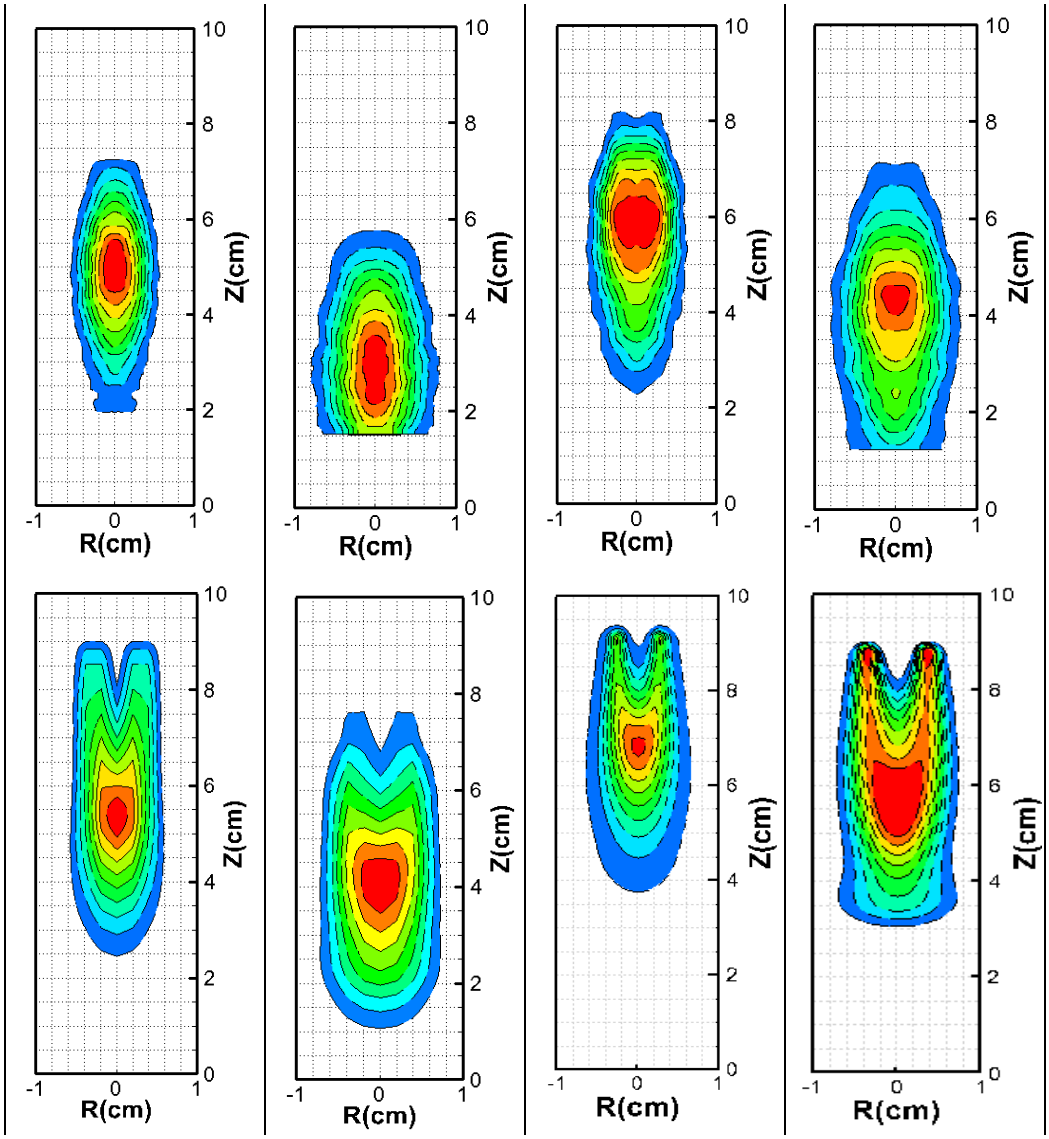

Figure 3.9 Comparison of soot mass (all normalized and averaged from 3.5ms-6ms) generation and distribution between the experiment (top row) and simulation (bottom row) (Operating conditions from left to right are case 6, 5, 10, 9 in Table 3.3)

3.5 M3 validation in engines

In order to test the capability of M3, the validation in engine combustion was also conducted. It is to be speculated that this mechanism would be computationally favourable in terms of cost in multidimensional CFD engine simulations due to its compact size. The simulations in three different types of

engines, including homogenous charged compression ignition (HCCI), premixed charged compression ignition (PCCI) and reactivity controlled compression ignition (RCCI) engine, were carried on with the KIVA4-CHEMKIN CFD codes. All of the tested engine specifications and operating conditions are tabulated in Table 3.4. The models in KIVA-4 were well-validated and the constants in the models were kept the same as in the previous studies in [130, 131].

Table 3.4 Specifications and operating conditions of the tested engines

Engine	Cummins	Sandia GM	GW4D20
Combustion	HCCI	PCCI	RCCI
Fuel	PRF73	PRF25	Gasoline/diesel
Bore×stroke (mm)	102×120	90.4×82	93.1×92
Compression ratio	14:1	16.4:1	16.7:1
Engine speed (rpm)	1200	1500	1600
Injection manner	Port injection	Direct injection	Port + direct injection
Injection timing	-	-23.1 ATDC	-40~-20 ATDC
Equivalence ratio	0.44	0.3	-
Intake tem. (K)	333	372	368
IMEP(bar)	5.5	3.0	5.06

3.5.1 PRF HCCI engine

M3 was firstly validated in a PRF73 fueled HCCI engine (Cummins B-series six-cylinder diesel engine) [8]. A 45 degrees sector mesh which contains 14839 hexahedron cells as shown in Figure 3.7(b) was created for this engine because of 8 symmetrically distributed injector holes. Figure 3.10(a)

compared the heat release rate (HRR) and in-cylinder pressure between the experiment and simulation. Except for the slightly over-estimated pressure peak, it is observed that the predicted data agrees well with the experimental HRR and pressure. The over-prediction might be due to that the non-ideal homogeneity in the combustion chamber in experiment lowers the measured pressure and HRR peak.

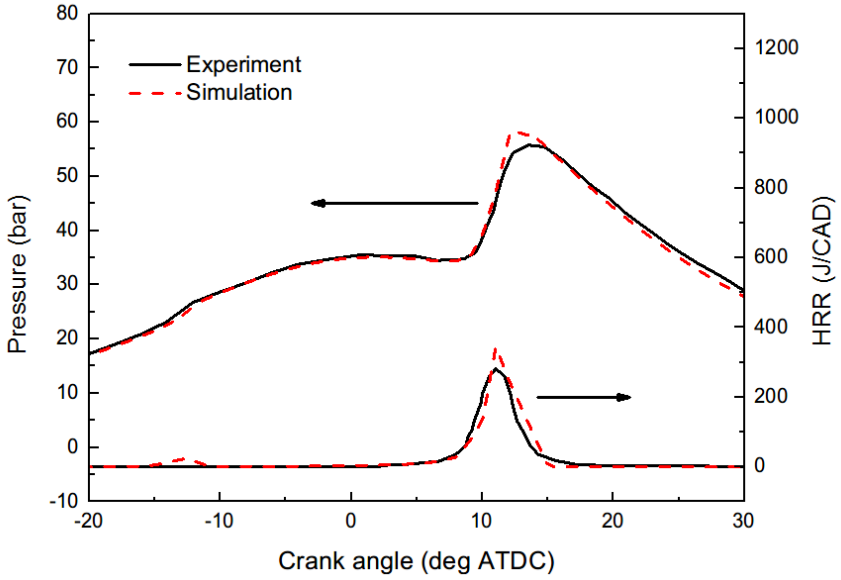

(a) HCCI condition

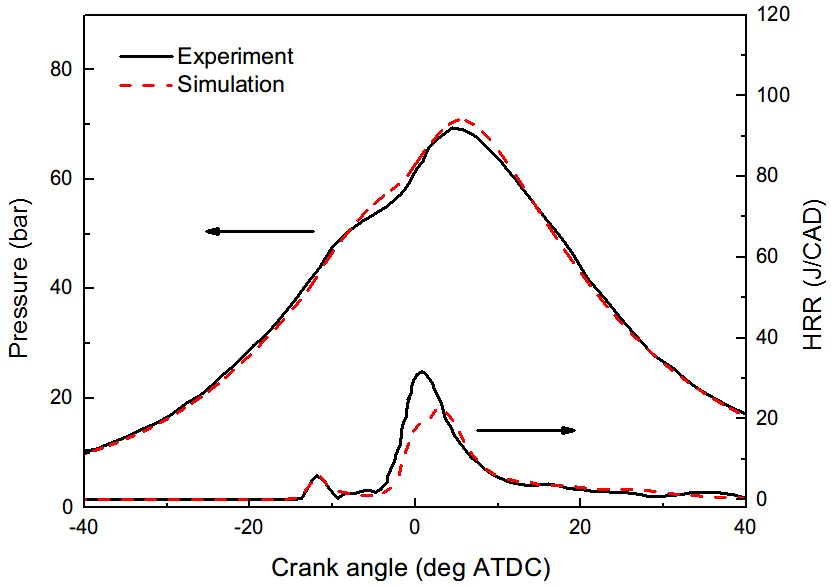

(b) PCCI condition

Figure 3.10 Comparison between the simulated and measured in-cylinder pressure and HRR results under (a) HCCI; (b) PCCI conditions

3.5.2 PRF PCCI engine

The combustion characteristics of low temperature combustion regime engines were also considered here. In the light of the experiment by Sahoo et al. [132] in a single-cylinder, early-injected (-21.3 after TDC (ATDC)) PCCI engine fueled by PRF27, the present M3 mechanism was used to couple in

KIVA-4 and predict the combustion characteristics for comparing with the experimental combustion characteristics in PCCI conditions. A 51.43 degree sector mesh with 9522 hexahedron cells was created as shown in Figure 3.7(c). The comparison between the predicted and measured results is shown in Figure 3.10(b). As shown, the low-temperature heat release (the first peak) in the engine is captured by the current mechanism, which implies the reliability of M3 to be used in low temperature combustion engines. In addition, the overall pressure and HRR trace show good consistency, indicating the reliability of M3 in PCCI engine combustion application.

3.5.3 Gasoline/diesel RCCI engine

As mentioned in Section 3.1, the primary objective of this chapter is to develop a robust and compact mechanism for RCCI combustion simulations. The experiments were conducted in a dual-fuel single-cylinder GW4D20 diesel engine by the authors. The engine specifications and experimental details can be found in [133]. The combustion characteristics are validated under double direct injections with gasoline port-fuel injection. In addition, by varying the injection timing under the single-injection scenario, another set of experiments were done to validate the combustion characteristics and emissions (NO_x and soot). The injection timing was varied under 50% (by heating value) gasoline port-injection and 50% diesel direct-injection from -20 ATDC to -40 ATDC. To simulate the RCCI engine, a 51.43 degree sector mesh with 8580 hexahedron

cells as shown in Figure 3.7(d) was created. Figure 3.11 shows the pressure comparison results between the experiments and simulations. For all the different injection strategy cases, the in-cylinder pressure was well captured by the simulations, indicating that the application of the current mechanism in RCCI engine is trustworthy. Also, the NOx and soot emission were validated under different injection timing of the direct diesel injection. As shown in Figure 3.12, the trend and value of NO_x and soot predicted by the simulation work agree well with the experimental ones. Hence, the NO_x and PAH sub-mechanism in the current mechanism were validated.

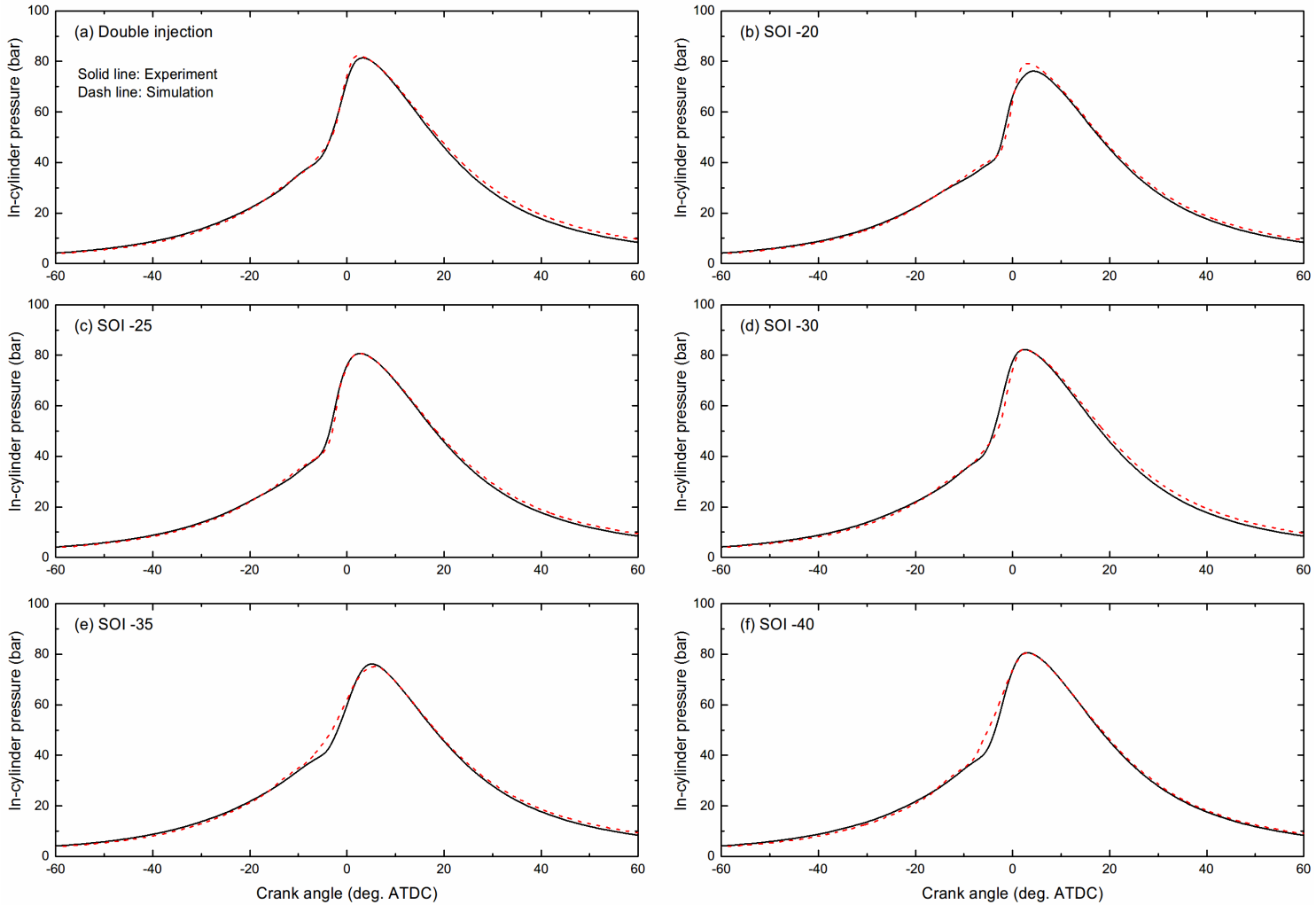

Figure 3.11 Comparison of pressure between the experiment and simulations with different injection strategies

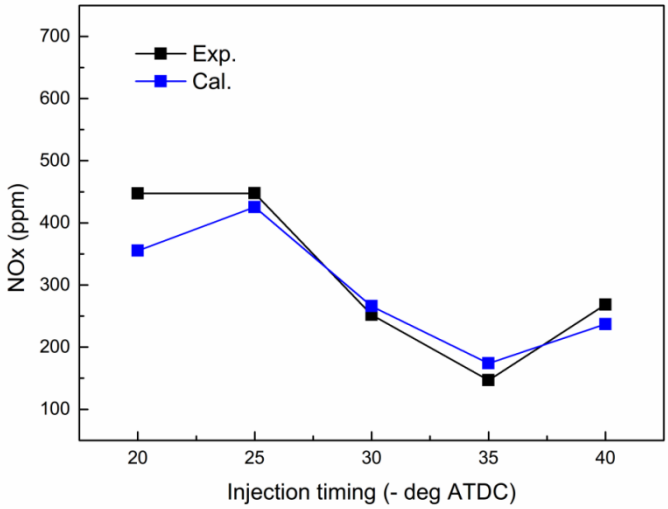

(a) NOx emission comparison between the experiment and simulation

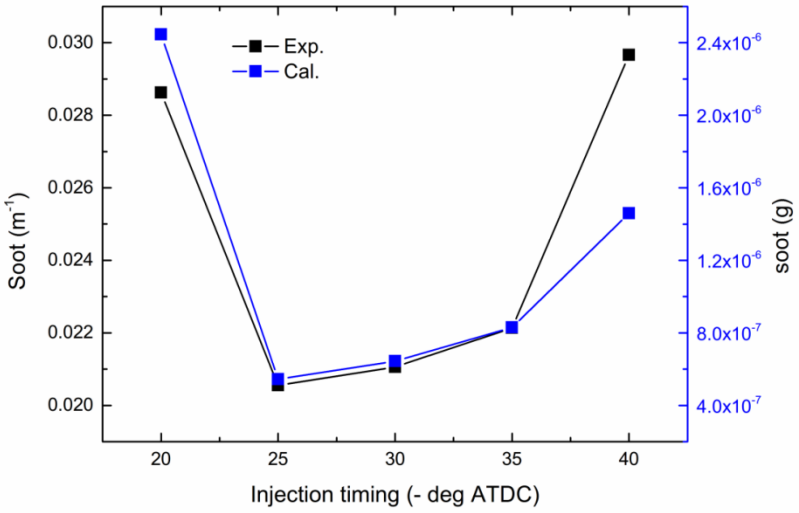

(b) Soot emission comparison between the experiment and simulation

Figure 3.12 NOx and soot emission comparison between experiment and simulation under different injection timings

3.6 Summary

In the process of developing a reduced PRF mechanism coupled with PAH for combustion and soot prediction, a semi-empirical methodology was tested. Two PRF mechanisms M1 with 51 species and 225 reactions, M2 with 43 species and 144 reactions with different core sub-mechanisms were developed

and preliminarily validated by ignition delay and laminar flame to prove the semi-empirical methodology. In addition, a PAH mechanism was coupled into M2 models, forming a 77 species and 225 reaction mechanism M3. This final version mechanism was validated by combustion characteristics (ignition delay, laminar flame speed, and intermediate species) and soot formation in various reactors including RCM, shock tube, JSR and constant volume combustion, also soot formation and combustion characteristics including in-cylinder pressure and HRR in different engines. The validation results show that this reduced PRF mechanism is able to provide credible predictions for combustion and soot formation in different reactors and engines for PRF and gasoline/diesel fuels. In sum, robust and compact chemical mechanisms with different sizes and functions for gasoline/diesel chemistry in the dual fuel RCCI engine combustion have developed.

This page was intentionally left blank

Chapter 4 Auto-ignition and Diffusion Flame Modeling in RCCI Combustion

4.1 Introduction

RCCI combustion involves low-temperature combustion and partially premixed combustion, rendering substantial complexity for combustion modeling. Researchers proposed different combustion models and integrated them into CFD framework for RCCI combustion simulations.

As a variant of HCCI, the method of CHEMKIN coupled CFD has been also applied for RCCI engine simulations. In fact, because in the KIVA framework, the transport and chemical source terms are solved separately [58], KIVA coupled CHEMKIN has even been used for conventional diesel engine simulations in which the combustion is organized by diffusion flame. Considering that flame propagation is very rare in RCCI combustion, it is shown that CHEMKIN coupled CFD has shown good predictability in RCCI combustion simulations [130, 131, 133-135]. However, its computational price is high especially for detailed mechanisms with large size and most of the computational effort are devoted to solve the ODEs in CHEMKIN. Moreover, different from HCCI, multiple combustion modes including diffusion flame and auto-ignition may co-exist in RCCI combustion, an effective method to model the diffusion flame and treat the border between diffusion flame and

autoignition is important. Hence, it is desirable to consider the diffusion flame and auto-ignition seamlessly and efficiently in RCCI combustion.

This chapter proposed a CTC model based on the original CTC model for CDC [19] and coupled it with a well-premixed reactor model for RCCI combustion simulation. It is able to solve the detailed chemical kinetics in RCCI combustion and show favorable computational price and accuracy than the commonly used sole well-premixed reactor model with CHEMKIN. This hybrid model was integrated into KIVA4 codes and validated by comparing with the experimental data from a RCCI engine fueled with gasoline/diesel. It is observed that this model can give reasonable combustion characteristic compared with the measured data. A better accuracy than the sole well-premixed reactor model with CHEMKIN can be found as well. More importantly, an evident computational overhead reduction of the current model can be observed, compared with the well-premixed reactor model with CHEMKIN.

4.2 Methodology

In conventional simulations of diesel diffusion flame, for the cells lower than a critical temperature T_c, all the chemistry and internal energy change in these cells will be treated by autoignition models (i.e., SHELL in the classical SHELL-CTC model with generic chemistry; well-premixed reactor model with CHEMKIN with detailed chemistry). In the existing RCCI engine combustion

models, all the autoignition and diffusion flame are handled by the well-premixed reactor model with the CHEMKIN library without considering the sub-grid turbulence-chemistry interaction. To illustrate the current model in a direct way, a schematic figure is shown as Figure 4.1, based on the original figure of quasi-steady diesel combustion plume as presented by Dec et al. from Sandia National Laboratories [136]. This study proposed a hybrid model with computing the autoignition cells by well-premixed reactor model with CHEMKIN and calculating the diffusion flame by CTC (the orange cells in Figure 4.1).

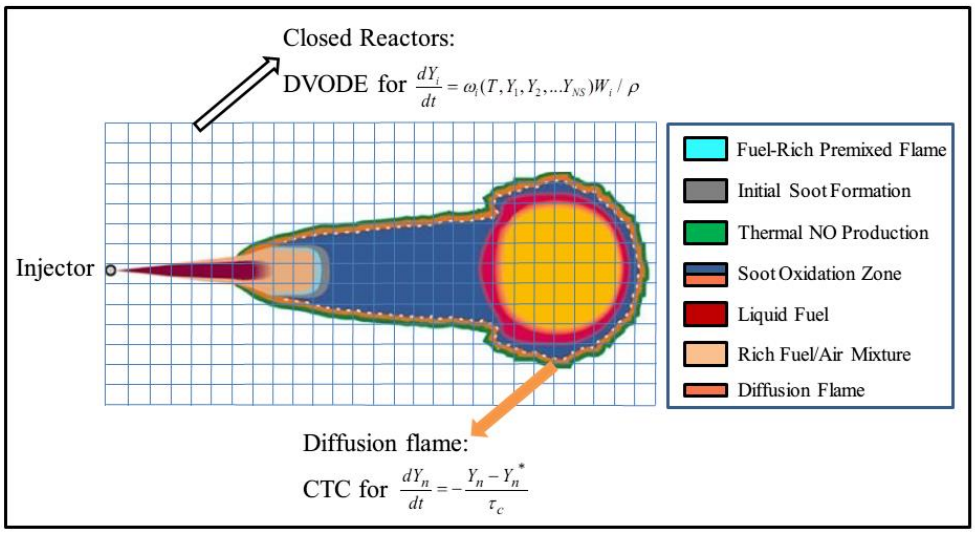

Figure 4.1 Schematic figure of the current hybrid model; the grids imply the computational domain in an engine simulation. Different colours mean different combustion and emission formation zones. The diffusion flame cells with orange colour are calculated by the CTC model while other cells are computed by the well-premixed reactor model

Nevertheless, the classical CTC model was formulated with a generic chemical model and is not capable of dealing with detailed chemistry. In the

following sections, the formulation of CTC with detailed chemistry is presented; a brief introduction of the well-premixed reactor model treated by CHEMKIN library is then described; the solution algorithm and the couple of these two models are finally introduced.

4.2.1 Formulation of CTC model with detailed chemistry

The characteristic time combustion (CTC) model is a classical model to be used in the conventional diesel combustion [19, 137]. The assumption in this model is that in the high temperature conditions, the chemistry in the system tends to be in equilibrium after a certain period of time. Thus in this model, the conversion rate of the partial density for specie *n* is given by:

$$\frac{dY_n}{dt} = -\frac{Y_n - Y_n^*}{\tau_c} \tag{4.1}$$

where Y_n is the mass fraction of specie *n*, Y^* is the instantaneous equilibrium value of the mass fraction, τ_c is the characteristics time-scale to achieve such an equilibrium state. It is noted that the most critical parameter in Eq. (4.1) to be modelled is the characteristic time-scale τ_c and the instantaneous equilibrium value Y^*. As seen in this model, the species conversion rates are approximated by the species conversion rates during its disequilibrium-to-equilibrium process. Thus, it is extremely applicable for conventional diesel combustion where diffusion flame dominates.

Typically, the characteristic time is approximately formulated by the sum

of the laminar timescale and the turbulent timescale [19], i.e.

$$\tau_c = \tau_l + f \cdot \tau_t \tag{4.2}$$

where τ_l is the laminar timescale; τ_t is the turbulent timescale; f is a delay coefficient that determines the controlling role of turbulent effects.

Because the current CFD framework KIVA-4 adopts RNG $\kappa-\varepsilon$ turbulence model [38], the turbulent characteristic timescale was estimated by

$$\tau_t = C_2 \cdot k / \varepsilon \tag{4.3}$$

where k and ε are calculated in the turbulence model. C_2 is a model constant with a value of 0.1 in the original RNG $\kappa-\varepsilon$ model, which is considered as a tunable parameter in the current study. The sensitivity analysis of C_2 will be shown in the following section.

Typically, the laminar timescale could be calculated by an Eigen-analysis of the Jacobian matrix of the chemistry ODEs by:

$$\tau_l = 1/\left|\lambda_g(J)\right| \tag{4.4}$$

where J is the Jacobian matrix of the chemistry ODEs; λ_g is the eigenvalue of J.

However, decomposition of the Jacobian matrix either evaluated numerically or analytically could cause undesirable computation overhead. Hence, a semi-empirical one-step reaction rate from a single droplet autoignition experiment for n-heptane and iso-octane [138] are used to predict

the laminar timescale:

$$\begin{aligned}
&\tau_{gasoline} = A_1^{-1} \cdot [C_8H_{18}]^{0.25} \cdot [O_2]^{1.5} \cdot \exp(E_1 / RT) \\
&\tau_{diesel} = A_2^{-1} \cdot [C_7H_{16}]^{0.25} \cdot [O_2]^{1.5} \cdot \exp(E_2 / RT) \\
&\tau_l = x(C_7H_{16}) \cdot \tau_{diesel} + x(C_8H_{18}) \cdot \tau_{gasoline}
\end{aligned} \tag{4.5}$$

in which, the bracket implies the mole concentration; A_1 = 5.1e+11; E_1 = 125.52 kJ/mol; A_2 = 4.6e+11; E_2 = 167.36 kJ/mol; R is the universal gas constant; T is the temperature; x means the mole fraction of one single fuel in the binary fuels.

The delay coefficient f in Eq. (4.2) is calculated by:

$$f = \frac{1 - e^{-r}}{1 - e} \tag{4.6}$$

where r is a parameter to indicate the completeness of combustion and could be approximated by:

$$r = \frac{Y(CO_2) + Y(H_2O)}{1 - Y(N_2)} \tag{4.7}$$

where Y means the mass fraction of a certain species.

Another important parameter in CTC model is the equilibrium partial density. Unlike the classical CTC model [19] which only 7 species were considered and the equilibrium partial density could be evaluated by assuming an incomplete combustion with products of CO, H_2O and CO_2 or a complete combustion with products of CO and H_2O and solving a serial of linear equations, the current model was proposed to account for detailed chemistry. Thus, in order to evaluate the equilibrium partial density Y^*, a chemical equilibrium solver CEQ [139] was coupled into the current CFD code KIVA4.

CEQ adopted Gibbs function continuation algorithm to achieve better computational stability and solved the local species mass fraction as a function of local enthalpy and pressure:

$$Y^* = Y_i^{EQ}(H, P) \tag{4.8}$$

In addition, the classic CTC is supposed to be proposed for diffusion flame computation in conventional diesel engine combustion which is known as the type of mixing-controlled combustion. Hence, if applied in RCCI combustion, besides the temperature, another border in the CTC model should be designed to identify the diffusion flame regime. In this study, the Damköhler number indicating the chemical reaction timescale (reaction rate) to the transport phenomena rate occurring in the system is adopted:

$$Da = \tau_t / \tau_l \tag{4.9}$$

where Da is the Damköhler number. Hence, if the Damköhler number in a certain cell is larger than a critical Damköhler number Da_c, the transport phenomena in that cell dominates the rate thus this cell will be computed by the CTC model. In sum, the precondition that the cell should be taken as in the diffusion flame regime is that its temperature is larger than T_c as well as its Damköhler number is larger than Da_c.

4.2.2 Well-premixed reactor model with CHEMKIN

In the current study, except for the cells whose temperatures are greater

than T_c and thus considered to be tended into equilibrium, the chemistry in other cells are deemed to be trapped in well-premixed reactors, in which the species conversion and the enthalpy change are solved by a chemistry solver – CHEMKIN. A skeletal primary reference fuel (PRF) chemical mechanism consisting of 43 species and 144 reactions developed in Chapter 3 was adopt for the combustion chemistry of gasoline and diesel [140] in this study. The convection and diffusion transport between cells are modelled by the RNG $\kappa-\varepsilon$ turbulence model [38]. Once considering the chemical process in a cell, this cell was considered as a closed system, in which the sub-grid scale turbulence chemistry interaction is not considered. Using CHEMKIN to model the combustion in the two limits from chemistry-controlled combustion to mixing-controlled combustion has been proved working well [58]. The change of each species in one closed computational cell was given by Eq. (2.36).

Hence, if N is the number of species in chemical mechanism, a set of ordinary differentiate equations (ODEs) with N equations will be built and then solved by VODE [94]. In this way, the energy governing equation can be obtained under constant pressure conditions as Eq. (2.37). With the newly updated species concentration by CHEMKIN, KIVA-4 will solve the energy conservation equation and update the temperature and other thermodynamic data in the system.

4.2.3 Solution algorithm

The solution algorithm in this hybrid model is intuitive:

1. Critical temperatures T_{cut} for initiating the well-premixed reactor model (700 K is recommended and was used in the current study) and T_c for initiating the CTC model (1200 K is recommended and was used in the current study) and a critical Damköhler number Da_c (1000 is recommended and was used in the current study) are pre-set as inputs into the program.

2. With the compression of the piston during the engine simulation, the temperature increases to a critical point T_{cut} where the well-premixed reactor model starts to compute the low-intermediate temperature auto-ignition in the computational domain.

3. The CTC model will be initiated for diffusion flame if the temperature of any cells is higher than T_c and the Damköhler number is larger than Da_c. Simultaneously, the well-premixed reactor keeps dealing with the other cells.

The temperature and Damköhler number of each cell will be compared with the critical temperatures at each time step to categorize the cells into the proper model.

4.3 Results and discussions

4.3.1 Validation

To validate the current model, the calculated combustion characteristics including pressure and heat release rate are compared with the experimental

data. The current hybrid model was compared with the well-premixed reactor model with CHEMKIN in terms of accuracy and computational cost.

The experiments were conducted in a single cylinder dual fuel GW4D20 engine fueled with gasoline and diesel. The operating conditions and engine specifications are listed in Table 4.1.

Table 4.1 Engine specifications and operating conditions

Engine	GW4D20 diesel engine
Fuel	Gasoline/diesel
Bore×stroke (mm)	93.1×92
Compression ratio	16.7:1
Engine speed (rpm)	1600
Injection manner	Port + direct injection
SOI (ATDC)	-60, -35, -30
Intake tem. (K)	368
IMEP(bar)	5.06

More than 6 different start of injections (SOIs) were tested experimentally, in which three of them were chosen for this validation [133]. Two of them are single injections with SOI of -35, -30 degree after the top dead center (ATDC) while the other one is a double injection with the first SOI -60 degree ATDC and second one -35 degree ATDC. Because of 8 evenly distributed injector holes in the injector in this testing engine, a 45 degree computational grid was created as shown in Fig. 2. By setting the same initial thermodynamic conditions in KIVA4-CHEMKIN-CTC and KIVA4-CHEMKIN, the simulations were conducted on the clusters in National University of Singapore (NUS) High

Performance Computing (HPC) center.

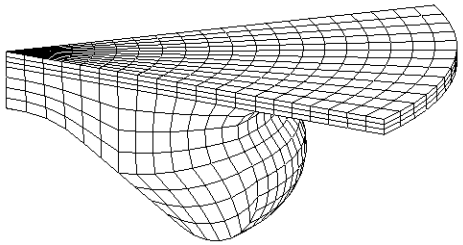

Figure 4.2 Computational grid of the testing engine at 0 deg. ATDC

The comparison among the current hybrid model, sole well-premixed reactor model with CHEMKIN and the experimental data is presented in Figure 4.3, Figure 4.4 and Figure 4.5. It is noted that all the data calculated from the current hybrid model were obtained by setting C_2 = 0.1 and Da_c = 1000 for all cases. It is observed that for all different SOI and different injection strategies, the current hybrid model predicted the pressure traces better than the pure well-premixed reactor model. With respect to the heat release rate, it is more obvious to note that in Figure 4.3 and Figure 4.4, the sole well-premixed reactor model with CHEMKIN underestimate the HRR peak while the current hybrid model captured the HRR peak more accurately. This might be attributed to the fact that that the pure well-premixed reactor resolves the diffusion flame by assuming a perfectly stirred reactor without considering the turbulence under the grid scale. Moreover, it is interesting to be noted that the difference between the pressure and HRR trace of the SOI -60 deg. ATDC case is not substantial, indicating that with a separate advanced injection, the flame is more of a premixed combustion type and in the hybrid model and more cells are

computed by the well-premixed reactor model with CHEMKIN.

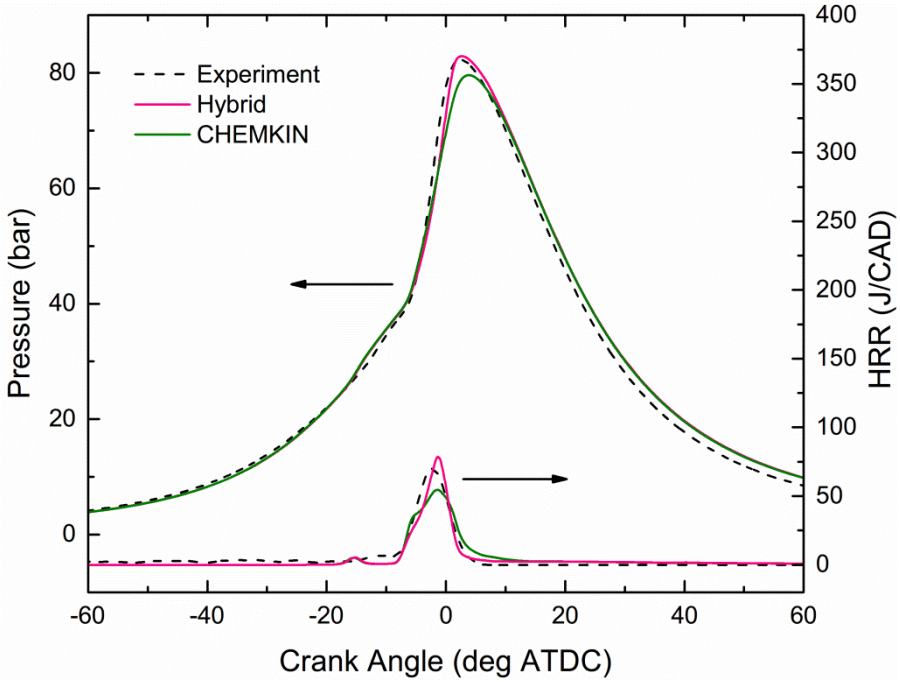

Figure 4.3 Comparisons of pressure traces and HRRs as a function of crank angle with SOI=-30 degree ATDC

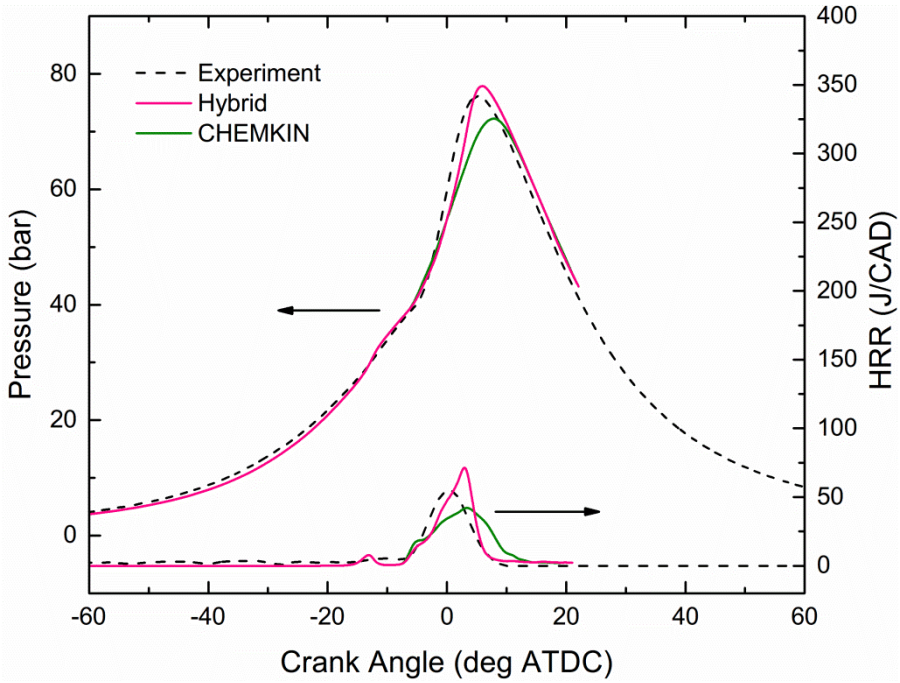

Figure 4.4 Comparisons of Pressure traces and HRRs as a function of crank angle with SOI=-35 degree ATDC

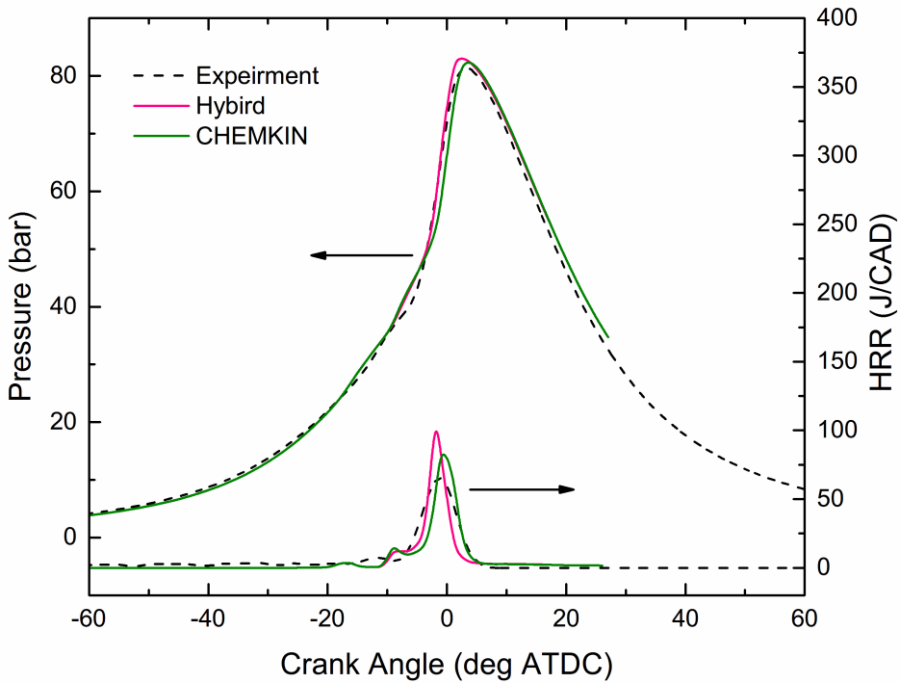

Figure 4.5 Comparisons of Pressure traces and HRRs as a function of crank angle with SOI=-60 degree ATDC with double injections

In addition, in Figure 4.6 for the SOI=-30 case, it is shown that in the temperature spatial plots the combustion occurs at the end of the spray tip where the Damköhler number is larger than the critical Damköhler number (as indicated by the Da=1000 contour line), implying that at the beginning of the combustion, the combustion is of mixing controlled type. It is also noted that after the combustion occurrence, the temperature and Damköhler number in more and more cells are becoming larger than the critical Damköhler number and temperature, thus the percentage of cell numbers computed in CTC dramatically increases.

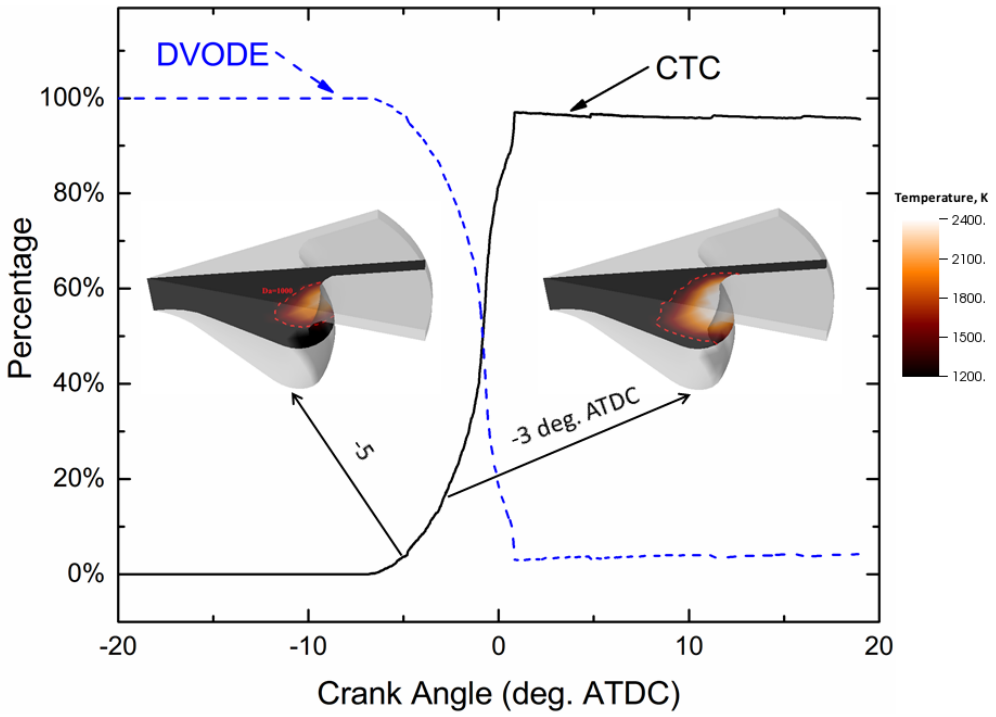

Figure 4.6 Percentage of cell numbers computed in each solver as a function of crank angle with SOI=-30 degree ATDC in the current hybrid model. The temperature spatial contours are shown at the beginning of mixing controlled combustion occurrence (-5 deg. ATDC) and at -3 deg. ATDC. The red dash line in the spatial contours indicates the Da=1000 contour line

Furthermore, because of fewer cells computed by the well-premixed reactor model with CHEMKIN in the hybrid model, less stiff chemistry ODEs system were solved by VODE. Hence, it is expected that there would be a reduction of computation time of the hybrid model because in the CTC model, solving the chemistry in these cells only needed to solve very simple equations through Eq. (4.1)-(4.7) and undergo the equilibrium solver calculation. Indeed, as shown in Figure 4.6, the hybrid model can save maximally more than 40% computational time than the sole well-premixed reactor model. As discussed in the combustion characteristics validation, the SOI -60 deg. ATDC case

computed most of the cells in the well-premixed reactor model with CHEMKIN, which could explain the fact that as shown in Figure 4.7, the computational time difference between the current hybrid model and the well-premixed reactor model in this case is trivial.

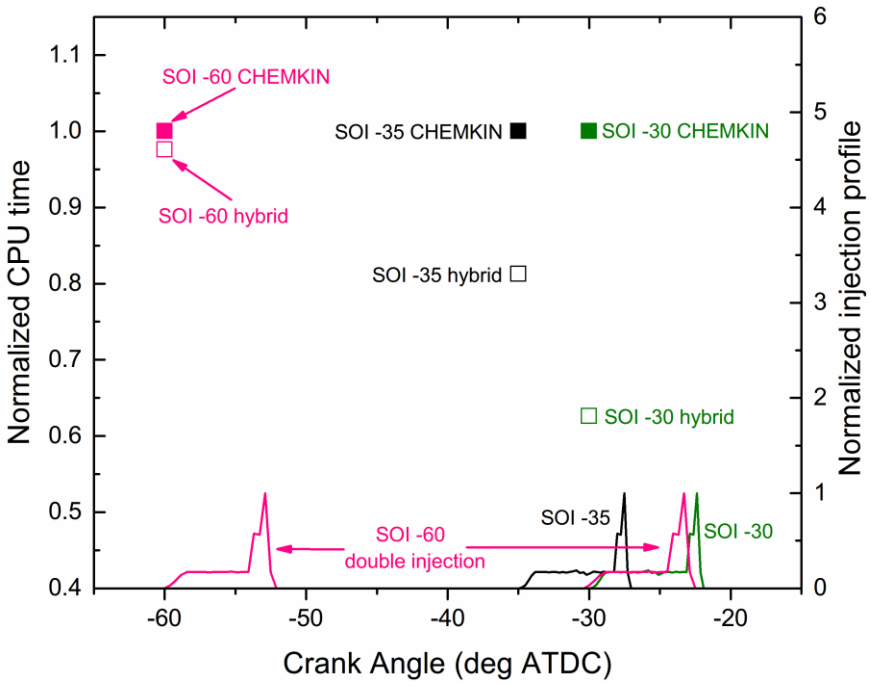

Figure 4.7 Normalized computational time and injection profile with different start of injections. The solid lines indicate the injection profiles

4.3.2 Sensitivity analysis of the tunable model parameters

One of the advantages of this current hybrid than the sole well-premixed reactor model with CHEMKIN is that it avoids its dependence of the combustion solely on fuel chemistry mechanism. A tunable parameter C_2 could be easily adjusted for different engines to properly simulate the experimental conditions. It has to be mentioned that when simulating the same engine for different operating conditions, C_2 should not be changed. In this section, a sensitivity analysis of the tunable constant C_2 in Eq. (4.3) was conducted. As

shown in Eq. (4.3), an increase of the value of C_2 could increase the turbulence timescale. A longer turbulence timescale indicates a longer characteristic time to reach the equilibrium thus a slower species conversion rate. Hence, a slower pressure rise rate would be expected with a larger C_2 value. As presented in Figure 4.8, by varying the value of C_2 among 0.05, 0.1 and 0.15 while keeping all of the other parameters constant as in the SOI -30 degree ATDC case, an obvious different computed pressure rise rate can be observed. Specifically, a larger C_2 value can lead to slower combustion and slow different pressure rise. It is pointed out that the change of C_2 could significantly lead to an obvious pressure rise rate change. Hence, users of this model should be tuning this constant cautiously to get an accurate prediction when this model is used for a new engine.

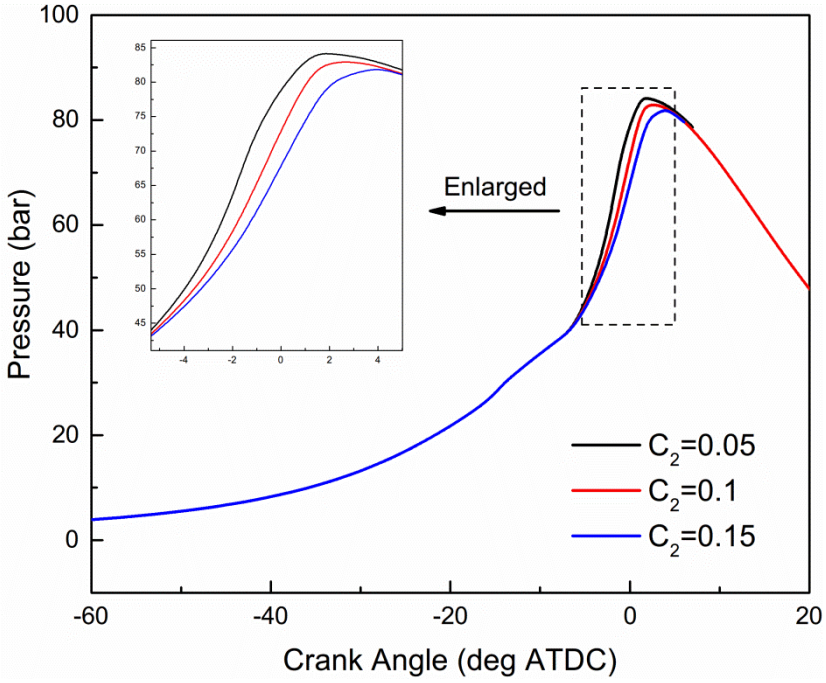

Figure 4.8 Comparison of pressure traces as a function of crank angle under various C_2 (0.05, 0.1, 0.15), computed with the SOI=-30 case. The enlarged graph shows the rapid pressure rise part of the pressure traces

Another model parameter that might affect the model performance is the critical Damköhler number Da_c. The chosen value Da_c=1000 in the present validation is based on the observation of a previous mixed-mode large eddy engine simulation [141]. As shown in Eq. (4.9), it is speculated that a too small Da_c value might lead to a possible scenario that some high-temperature premixed combustion cells are mistakenly computed as diffusion flame cells in CTC and consequently the species conversation rate could be overestimated. Varying Da_c from 10 to 1000 while keeping all of the other parameters constant as in the SOI -30 degree ATDC case, the calculated pressure traces were compared and shown in Figure 4.9. It is observed that during the combustion process (rapid pressure rise), the difference among these three cases is not obvious, indicating that after the fuel spray at -30 degree ATDC, the *Da* number of most of the high-temperature cells are larger than 1000 and the flame is of mixing-dominant type. The enlarged figure shows that the pressure of the Da_c =1000 case slightly deviate downwards from the other two cases, implying that the Damköhler number of some cells fell into the range between 100 and 1000. After the pressure peak where most of the fuel atomization and evaporation have been ended but most of the cell temperatures are still larger than T_c, using CTC to compute the combustion could overestimate the species conversion rate.

Hence, from Figure 4.9, it is observed that during the expansion stroke, the Da_c = 10 case shows overestimated pressure than other cases because most of the high temperature cells are still computed by CTC in this case.

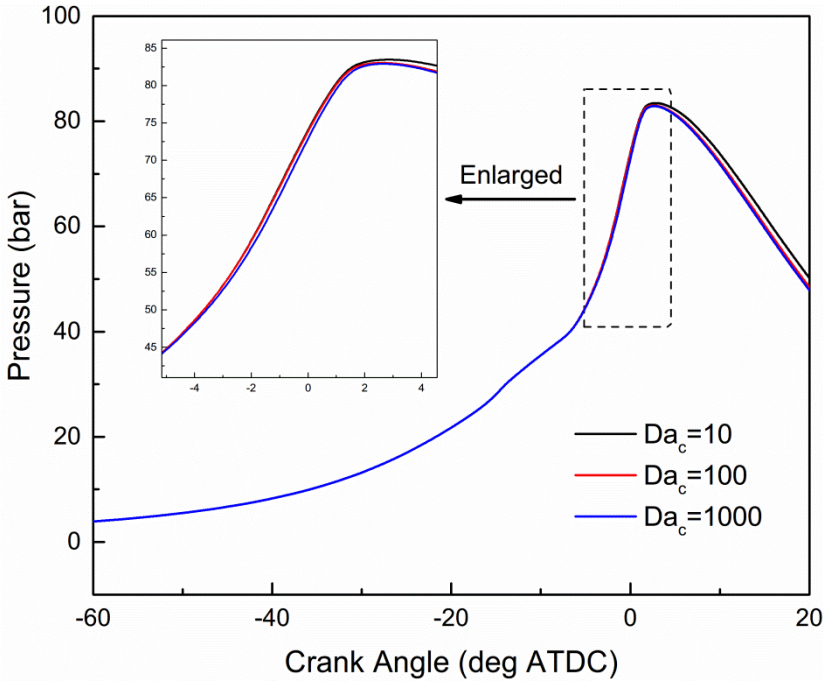

Figure 4.9 Comparison of pressure traces as a function of crank angle under various Da_c (10, 100, 1000), computed with the SOI=-30 case. The enlarged graph shows the rapid pressure rise part of the pressure traces

4.4 Summary

Under some certain scenarios when diffusion flame is substantial in RCCI combustion, it is more accurate to model the diffusion flame with turbulence-chemistry interaction considered. A hybrid model with the classical CTC model and well-premixed reactor model was proposed for RCCI combustion modeling, as a substitute of the conventional sole well-premixed reactor model. A semi-empirical one-step reaction rate from a single droplet auto-ignition experiment was adopted for the laminar timescale evaluation

while the turbulence timescale was estimated by the RNG $\kappa-\varepsilon$ model. To account for detailed chemistry in this hybrid model, a CEQ equilibrium solver was employed to solve the species concentrations under equilibrium state. This detailed chemistry CTC model was then coupled with the well-premixed reactor model with CHEMKIN library, forming a hybrid model which is able to compute the autoignition and diffusion flame under RCCI conditions.

By comparing its prediction performance with both the experimental data and the predicted data from the sole well-premixed reactor model with CHEMKIN library, it is proved that this hybrid model is robust to model RCCI combustion and gave reliable prediction for the combustion characteristics. More importantly, it is capable of reducing the computational time maximally more than 40% compared with the sole well-premixed reactor solver, due to fewer stiff ODEs solved in the CHEMKIN solver.

This page was intentionally left blank

Chapter 5 Flame Propagation Modeling in RCCI Combustion

5.1 Introduction

To achieve RCCI strategies in CI engines, wide operating conditions are required, which results in a broad spectrum of combustion regimes in a compression ignition engine and makes the combustion modeling more complex [141]. The most complex combustion is partially premixed combustion, in which not only autoignition and diffusion flame should be accounted, but also the flame propagations. Flame propagations are not usually considered in CI engines because unlike the SI engine in which ignition was triggered by a spark and combustion was organized by flame propagation, the combustion in a CI engine is initialized by auto-ignition and organized by diffusion flame. However, in RCCI, the high reactivity direct-injected fuel could play a role of spark and cause several flame propagations among the low reactivity fuel atmosphere [24]. Under this situation, no flame propagation consideration in the combustion model could cause unacceptable errors under certain operating conditions of RCCI engines.

To solve this problem, a level set based flame propagation model G-equation coupled with the SHELL and characteristic time models, and the

G-equation coupled with CHEMKIN was proposed by [23, 24], which gives acceptable prediction of RCCI engines under wide operating conditions. With a new CFD framework KIVA-4 which uses an unstructured mesh [36] and with a Lagrangian particle based model, this study proposed a Lagragian marker particle based flame propagation model [22] to predict the combustion and flame propagation in the RCCI partially premixed combustion. The formulation is introduced and the result shows that this model coupled with CHEMKIN could give better combustion simulation in wide-operating dual fuel engines than the numerical results without flame propagation considered.

5.2 Model formulation

5.2.1 Lagrangian markers

Zero-mass imaginary Lagrangian markers to track flame front position has been used in SI engine ignition model and gasoline direct injection combustion models [22, 52]. A certain number of particles which are initially assumed to be distributed uniformly and to describe a sphere will be convected by the in-cylinder gas due to the effect of chemical sources and the flow field. Once one point in the computational domain was ignited (spark ignition in SI or autoignition by the high-reactivity fuel in this study), and the physical-chemical conditions allow a self-sustained flame front to develop, the flame front will be tracked and described by the particles. In this study, the computational cell which contains these particles will be separately modeled for a premixed flame.

The heat release of other computational cells due to diffusion flame or premixed flame will be modeled by CHEMKIN. The details about the chemistry and combustion modeling in this flame propagation model (FPM) model and in the CHEMKIN will be described later.

5.2.2 CHEMKIN

In the current study, except for the flame front existing cells (containing particles), the chemistry is solved by a chemistry solver – CHEMKIN. The convection and diffusion transport between cells are modeled by RNG $\kappa-\varepsilon$ turbulence model [38]. The chemical process in a cell is considered as a closed system, in which sub-grid scale turbulence-chemistry interaction was not considered. Using CHEMKIN to model the combustion in the two limits from chemistry-controlled combustion to mixing-controlled combustion has been proved to work well [58]. The basic principle to update species concentrations in CHEMKIN in this chapter is the same as in Sector 4.2.2. With the newly updated species concentration by CHEMKIN, KIVA-4 will solve the energy conservation equation and update the temperature and other thermodynamic data in the system.

5.2.3 Flame propagation model

The basic idea of this FPM model was introduced in Section 5.2.1. The details of how FPM model simulates the flame propagation and how the FPM model calculates the turbulent flame speed and heat release in a dual fuel flame

front will be illustrated in this section. The same mechanism in [24] has been applied in this study, that is, a computational cell with a temperature higher than a critical temperature T_c is considered as the ignition site. Numbers of discrete particles will be initialized in those cells. Unlike the ignition kernel growth in a SI engine, instead of the plasma velocity, the speed of the self-sustained flame propagation has to be calculated for each particle according to the local conditions of every individual particle. In this study, the laminar flame speed (LFS) of gasoline and diesel dual fuel was calculated by their surrogate fuels, iso-octane and n-heptane, since a PRF mechanism was used. The current reduced PRF mechanism was developed and validated under wide thermodynamic conditions as in Chapter 3 (M2). The method adopted in this study to calculate the flame speed is introduced below.

Based on Metgalchi et al. [142], the experimentally measured LFS is correlated to equivalence ratio, temperature and pressure by:

$$S_L^0 = S_{L,ref}^0 \left(\frac{T_u}{T_{u,ref}} \right)^{\alpha} \left(\frac{P_u}{P_{u,ref}} \right)^{\beta} \cdot F_{dil} \tag{5.1}$$

where S_L^0 is the laminar burning velocity under current conditions while the subscript *ref* is the reference condition with pressure 1atm and temperature 298K. F_{dil} is a dilution factor. In the paper of Metgalchi et. al [142], by linearly fitting the experimental data, the equivalence ratio dependent coefficients α , β are found to be fuel-type independent for the given fuels: methanol, propane

and iso-octane:

$$\alpha = 2.18 - 0.8(\phi - 1) \tag{5.2}$$

$$\beta = -0.16 + 0.22(\phi - 1) \tag{5.3}$$

The LFS at reference conditions is given as:

$$S_{L,ref}^{0} = B_M + B_2 \left(\phi - \phi_M\right)^2 \tag{5.4}$$

For iso-octane, the values for B_M , B_2 and ϕ_M are 26.32, -84.72 and 1.13, respectively. As pointed out by Liang [21], this correlations about $S_{L,ref}^{0}$ could give acceptable flame speed predictions in conventional SI engines in which the premixed flame are near stoichiometric conditions. Unfortunately, this is not applicable in RCCI engine simulations due to the fact that negative LFS could be calculated by this correlation with small equivalence ratios in RCCI conditions. Hence, the expression proposed by Gulder [143] was used:

$$S_{L,ref}^{0} = \omega \phi^{\eta} \exp(-\xi(\phi - \sigma)^2) \tag{5.5}$$

where ω, η, ξ and σ are data fitting coefficients. For iso-octane, values of those coefficients were selected from Liang et al. [21] as shown in Table 5.1, which is optimized to match $S_{L,ref}^{0}$ prediction in Ref. [142] and different from the original values in Ref. [143].

Table 5.1 Fitting coefficients values for Eq. (5.5) from literatures for iso-octane and current estimation for n-heptane

	ω	η	ξ	σ
Iso-octane Gulder	46.58	-0.326	4.48	1.075
Iso-octane Liang	26.9	2.2	3.4	0.84
n-heptane Present	39.67	0.52	2.12	1.01

However, in the RCCI dual fuel engine, the flame propagation speed of a duel fuel composition should be calculated. Specifically in this study, another flame speed calculation of n-heptane should be predicted, which is, unfortunately, not reported by the literature. Apparently, the same correlation as iso-octane by Metgalchi et al. [142] is not applicable in n-heptane cases since it has only given the data fitting for the certain fuel types, excluding n-heptane at different pressures, temperatures and equivalence ratios. Hence, the same data fitting methodology in Ref. [142] was used to evaluate the flame speed of n-heptane. Without enough experimental data at different pressures, temperatures and equivalence ratios, the n-heptane LFS was calculated computationally by the PRF mechanism M1. Fitting by the presumed correlation Eq. (5.1) as shown in Figure 5.1, the equivalence ratio dependent coefficients α, β and $S_{L,ref}^{0}$ were obtained, as shown in Table 5.2. Hence, in terms of equivalence ratio ϕ, α and β could linearly expressed by:

$$\alpha = 1.82 - 0.2(\phi - 1) \tag{5.6}$$

$$\beta = -0.16 + 0.15(\phi - 1) \tag{5.7}$$

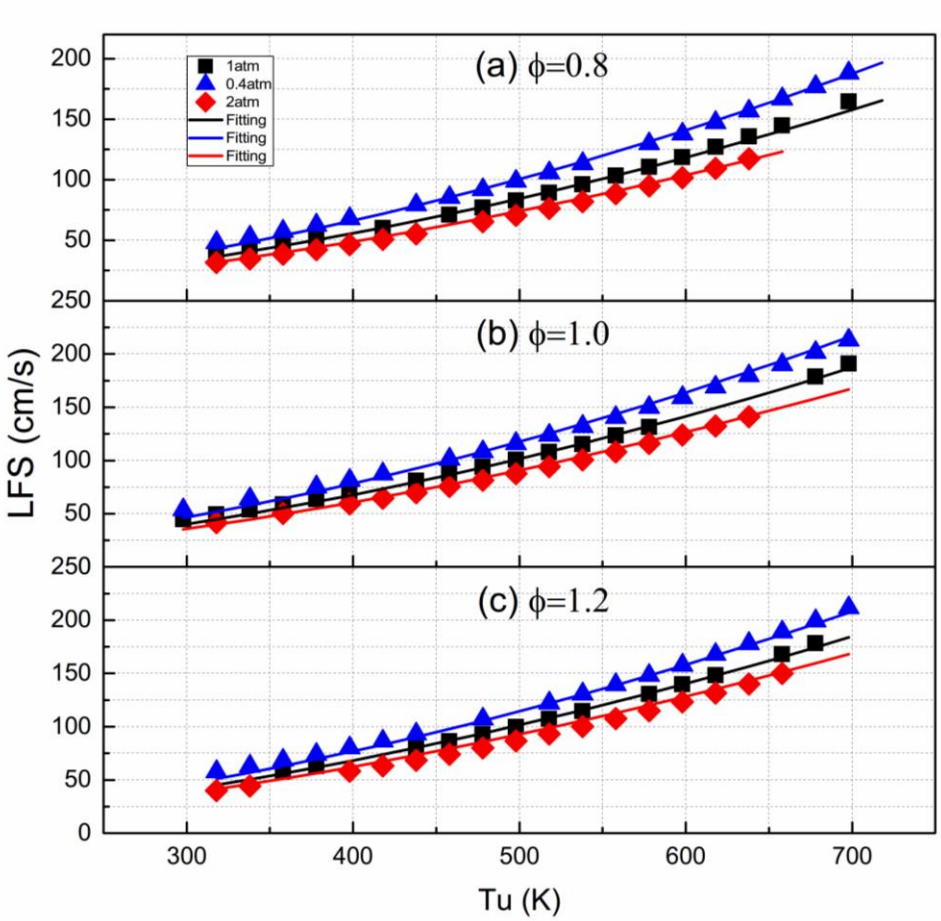

Figure 5.1 Laminar flame speed fitting by Eq. (5.1) under different pressures, equivalence ratios and temperatures in order to obtain α, β and S^0

Table 5.2 Coefficients values in Eq. (5.1) for n-heptane LFS prediction

Equivalence Ratio	α	β	$S^0_{L,ref}$
0.8	1.86	-0.19	32.2
1.0	1.82	-0.16	39.6
1.2	1.78	-0.13	40.4

Using the same methodology by Liang [21], Eq. (5.5) was used to fit $S^0_{L,ref}$. A comparison of fitting by Eq. (5.4) and Eq. (5.5) were presented in Figure 5.2, in which the symbols are $S^0_{L,ref}$ in Table 5.2. Using the least square fitting, the coefficients in Eq. (5.5) ω, η, ξ and σ for n-heptane were obtained and

given in Table 5.1.

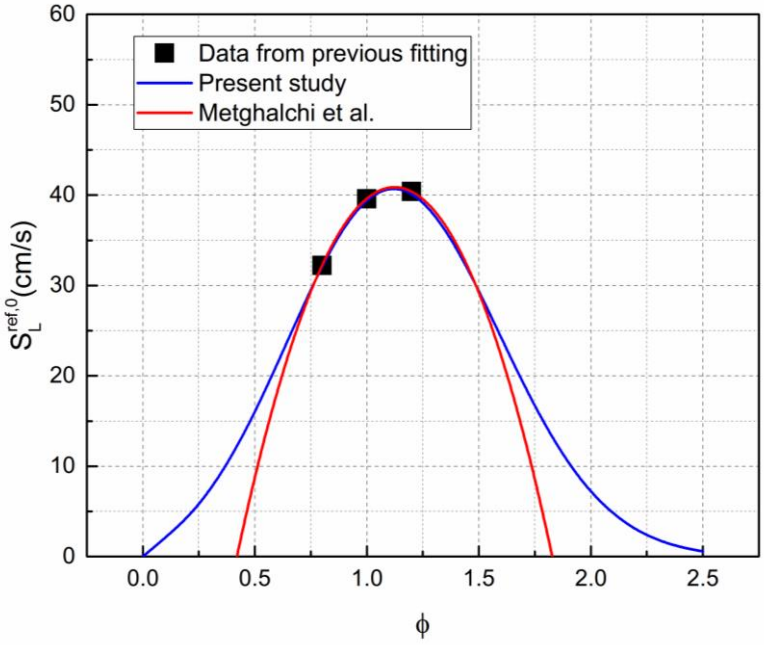

Figure 5.2 S^0 data fitting by Eq. (5.4) from Metgalchi et al. and Eq. (5.5) in the present study

The dilution effect coefficient was calculated as introduced in [144]:

$$F_{dil} = (1 - Y_{dil})^{(2.1 - 0.6Y_{dil} + 21.85Y_{dil})} \tag{5.8}$$

to make sure F_{dil} always be positive. Y_{dil} is the mass fraction of diluent.

According to the experimental observation in [73], flame speed of PRF binary mixtures could be approximately expressed by:

$$S_L = S_{L,iso-oct} \cdot PRF\% + S_{L,n-hep} \cdot (1 - PRF\%) \tag{5.9}$$

where S_L is the LFS of binary PRF mixture, $S_{L,iso-oct}$ is the LFS of iso-octane, $S_{L,n-hep}$ is the LFS of n-heptane, PRF means the PRF number of PRF mixture defined by the volume percentage of iso-octane in the mixture. The calculated PRF laminar flame speeds by Eq. (5.9) are shown in Figure 5.3 for different

PRF mixtures. Compared with the experimental data reported in [71, 73], a good agreement has been obtained.

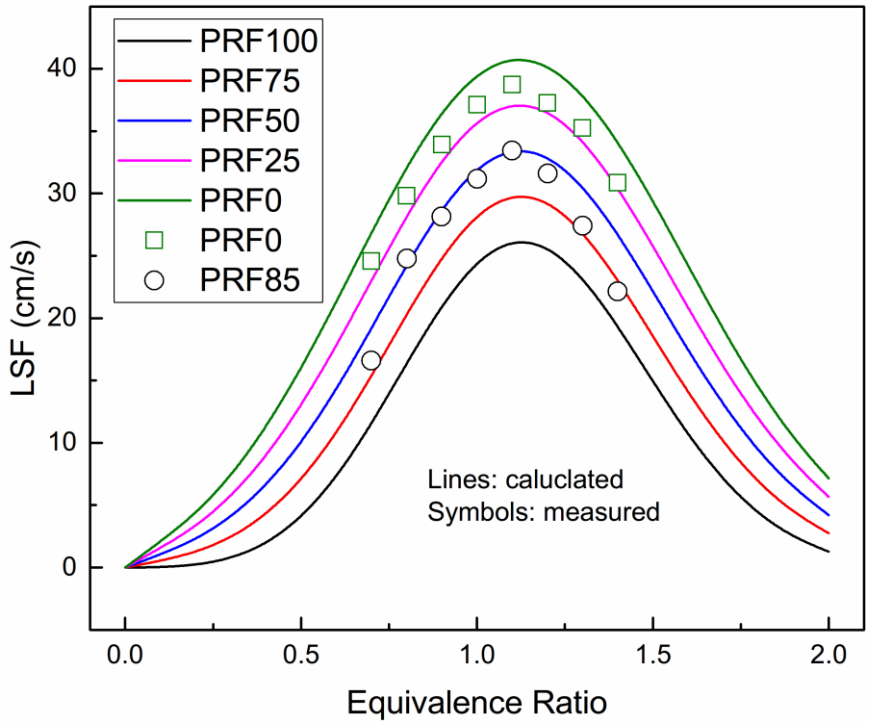

Figure 5.3 Laminar flame speed calculation by the correlation proposed in the current study as a function of equivalence ratio

The turbulent flame speed S_T is a function of local S_L and is given by [24]:

$$S_T = S_L + \mu' \left\{ -\frac{a_4 b_3^2}{2b_1} Da + \left[\left(\frac{a_4 b_3^2}{2b_1} Da \right)^2 + a_4 b_3^2 Da \right]^{1/2} \right\} \qquad (5.10)$$

where μ' is the turbulence intensity; b_1, a_4 and b_3 are turbulence modelling constants with value of 2.0, 0.78 and 1.0 respectively. Da is the Damköhler number and calculated by:

$$Da = \frac{S_L l}{\mu' l_F} \qquad (5.11)$$

In Eq. (5.11), l is the turbulence integral length scale which is derived from RNG $\kappa-\varepsilon$ turbulence model. l_F is the flame thickness:

$$l_F = \frac{(\lambda / c_p)|_{T_0}}{\rho_u S_L} \tag{5.12}$$

The heat capacity c_p and heat conductivity λ are evaluated at inner layer temperature T_0 =1500K in this study by:

$$\lambda / c_p = 2.58\times10^{-4} \frac{g}{cm\cdot \sec}(\frac{T_0}{298K})^{0.7} \tag{5.13}$$

where ρ_u is the unburnt mixture density.

The propagation of flame was represented by the propagation of the particles. Hence, the particle velocity is the turbulent flame speed S_T. In the KIVA-4 coordinates, particle velocity components u_p, v_p and w_p are calculated as:

$$\begin{aligned} u_p &= S_T \cdot \cos(\theta)\cdot\cos(\varphi) + u_{mom} \\ v_p &= S_T \cdot \cos(\theta)\cdot\sin(\varphi) + v_{mom} \\ w_p &= S_T \cdot \sin(\theta) + w_{mom} \end{aligned} \tag{5.14}$$

where θ and φ are random numbers between - π /2~ π /2 and 0~2 π, respectively; u_{mom}, v_{mom} and w_{mom} are the momentum vertex velocities of the cell in KIVA-4 that contains particles at x, y and z directions. It is pointed out that at each time step, the reason that there should be an addition of the cell momentum vertex velocities in the evaluation of velocity of the particles is due to the arbitrary Lagrangian-Eulerian methodology employed in the integration of the gas phase equation [36].

To model the conversion rates and heat release in the flame front, most of the Lagrangian particle models in the literature used a one-step reaction mechanism from the fuel and O_2 to CO_2 and H_2O to calculate the mass conversion rates by the density in the flame front ρ_f, and the flame surface area $A_{p,cell}$ within the cell. The flame surface area $A_{p,cell}$ could be approximated by the number of particles $N_{p,cell}$ divided by the total numbers of $N_{p,tot}$, as shown in Eq. (5.15) [52, 145]:

$$\frac{dm_f}{dt} = \rho_f S_T A_{p,cell} \approx \rho_f S_T 4\pi r_{p,cell}{}^2 \frac{N_{p,cell}}{N_{p,tot}} \tag{5.15}$$

With the goal of incorporating a detailed mechanism into this FPM model, a new method based on the idea of sub-grid scale unburnt/burnt volumes of flame-containing cells was suggested in this study. It assumes that in the sub-grid scale, the pressure and temperature are homogeneous and the mixture in the cell consists of burnt and unburnt portions. Another assumption is that the cell with a flame front tends to local equilibrium at constant pressure and constant enthalpy due to the unconstrained thermodynamic conditions locally. By this method, the species conversion rate in Eq. (5.15) then becomes:

$$\frac{d\rho_n}{dt} = \rho_u (Y_{n,u} - Y_{n,b}) S_T \frac{A_{p,cell}}{V_{cell}} \tag{5.16}$$

where ρ_n is the partial density of species *n*; ρ_u is the unburnt mixture density in the cell; $Y_{n,u}$ and $Y_{n,b}$ are the mass fraction of species *n* in the unburnt mixture and burnt mixture, respectively; V_{cell} is the volume of the cell. The method for

evaluating $A_{p,cell}$ is the same as in Eq. (5.15).

To evaluate $Y_{n,u}$ and $Y_{n,b}$, a chemical equilibrium solver CEQ [139] was coupled into the current CFD code KIVA-4. CEQ adopted a Gibbs function continuation algorithm to achieve better computational stability and solved the local species mass fraction as a function of local enthalpy and pressure:

$$Y_{n,b} = Y_n^{EQ}(H, P) \tag{5.17}$$

In addition, with the result from the CEQ solver, the adiabatic flame temperature T_{ad} was used to calculate the density of the burnt mixture:

$$\rho_b = \frac{P_{cell} \cdot MW_{mix,b}}{R_u T_{ad}} \tag{5.18}$$

where P_{cell} is the local pressure in the cell; $MW_{mix,b}$ is the average molecular weight of the mixture in the cell; R_u is the universal gas constant. Hence, the partial density of each species could be calculated by:

$$\rho_{n,b} = \rho_b Y_{n,b} \tag{5.19}$$

Based on the species mass conservation, the partial density of the unburnt mixture and unburnt species mass fraction can be given by:

$$\rho_{n,u} = \rho_n - \rho_{n,b} \tag{5.20}$$

$$Y_{n,u} = \frac{\rho_{n,u}}{\sum \rho_{n,u}} \tag{5.21}$$

With the calculated $Y_{n,u}$ and $Y_{n,b}$ in Eq. (5.16), the partial conversion rate of each species could be evaluated. Hence, by balancing the enthalpies of

formation of the species inside the cell, heat release and specific internal energy in the cell could be evaluated. The new cell temperature is then updated by the KIVA-4 state function.

5.2.4 NO_x model

The NO_x sub-model coupled in the current model for engine NO_x emission prediction is from [117]. Thermal NO formation is accounted for by the extended Zeldovich mechanism. In addition, N_2O to NO branch and NO to NO_2 branch are also covered in this NOx mechanism. The reactions are listed in Table 5.3. It should be noted that species conversion in the flame front in the FPM model has not included the species in NOx formation due to the slow rate of NOx reaction chemical reactions and that the equilibrium assumption is not valid for NOx formation reactions.

Table 5.3 NO_x reactions and the Arrhenius coefficients in the chemical mechanism.

Reactions	A	B	E
$N+NO=N_2+O$	3.50E+13	0	330
$N+O_2=NO+O$	2.65E+12	0	6400
$N+OH=NO+H$	7.33E+13	0	1120
$N+CO_2=NO+CO$	1.90E+11	0	3400
$N_2O+O=N_2+O_2$	1.40E+12	0	10810
$N_2O+O=NO+NO$	2.90E+13	0	23150
$N_2O+H=N_2+OH$	4.40E+14	0	18880
$N_2O+OH=N_2+HO_2$	2.00E+12	0	21060
$N_2O+M=N_2+O+M$	1.30E+11	0	59620
$NO+HO2=NO_2+OH$	2.11E+12	0	-480
$NO_2+O=NO+O_2$	3.90E+12	0	-240
$NO_2+H=NO+OH$	1.32E+14	0	360
$NO+O+M=NO_2+M$	1.06E+20	-1.4	0

5.2.5 Soot model

In this study, a multi-step phenomenological soot model which was proposed by Tao [76] has been implemented in to the KIVA-4 codes for the soot formation in RCCI engines. This soot model involves several steps including soot particle inception, particle coagulation and surface growth, etc. The soot particle generic precursor is produced from acetylene by:

$$C_2H_2 \xrightarrow{\dot{R}_2=\frac{2}{z}k_2[C_2H_2]} \frac{2}{z}R + H_2 \qquad (5.22)$$

where $k_2 = 1.0\times10^{11}\exp(-2.0\times10^4/T)(s^{-1})$; T is the temperature and z denotes

the carbon atom numbers in the precursor species; the bracket in $[C_2H_2]$ implies the concentration of C_2H_2 . The particle inception occurs from the precursor R to the particle P via:

$$R \xrightarrow{\dot{R}_3 = z k_3 [R]} P \tag{5.23}$$

where $k_3 = 5.0 \times 10^7 \exp(-2.52 \times 10^4 / T)(s^{-1})$. The particle coagulation occurred through the reaction as Eq. (5.24):

$$xP \xrightarrow{\dot{R}_4 = \frac{1}{2} k_4 N^2} P \tag{5.24}$$

where k_4 is a collision frequency constant and was evaluated by the equally-sized particles and the near-continuum coagulation constant. The surface growth is undergoing though the classical HACA mechanism as Eq. (5.25):

$$P + C_2H_2 \xrightarrow{\dot{R}_5 = k_5 [C_2H_2](A_{soot})^{1/2}} P + H_2 \tag{5.25}$$

where $k_3 = 1.05 \times 10^4 \exp(-3.1 \times 10^3 / T)(cm^{-1}s^{-1})$ and A_{soot} is the total surface area of a presumed spherical soot particle.

In addition to the precursor formation, soot inception and coagulation, the soot particles are oxidized by OH and O_2. The O_2 related oxidation is:

$$P + O_2 \xrightarrow{\dot{R}_6 = k_6 A_{soot}} P + 2CO \tag{5.26}$$

where k_6 is a constant from the NSC oxidation model as introduced in [146]. The OH related oxidation was considered by:

$$P + OH \xrightarrow{\dot{R}_7 = k_7 A_{soot}} P + CO + \frac{1}{2} H_2 \tag{5.27}$$

In this equation, k_7 is adopted from Neoh's model [147]. Readers who are interested in details in this soot model could refer to [76] for more information.

Specifically in this study, the computational cell, no matter whether it is in diffusion flame, premixed autoignition, or flame propagation front modes, will be modeled by this soot model by assuming that soot precursors are formed from C_2H_2 in the local cell.

5.2.6 Solution Algorithm

After the integration of all the models with the KIVA-4 CFD code, several criteria were applied to make seamless interactions of the models to consider the different combustion regimes in RCCI engines.

The ignition and low-temperature combustion processes were calculated by CHEMKIN until a fully developed flame was formed. In this process, all the cells are presumably a perfectly stirred reactor and the species conversion rate. It is noted that although turbulence and transport among cells are considered by the RNG $\kappa-\varepsilon$ turbulence model, sub-grid turbulence was not considered in the current study.

After the ignition kernel formed, considering the number of cells in the computational domain, $NP=1500$ Largragian particles were initiated and ready to develop into particles that represent a flame front. It is noted that the value of *NP* was determined with a simple sensitivity analysis approach by increasing *NP* to a value that the combustion characteristics do not change anymore. The

speed and directions of those particles are estimated by Eq. (5.14). For the particles that move out of the computational domain, the model sets their speed to zero and stops tracking them. The criterion to initiate a flame is when the cell temperature is greater than T_c=1200K, which is regarded as an ignition site, to account for the 300-400 K temperature rise due to ignition [23].

For each time-step, the cells that contain Largragian particles will be located. Their radius to the initial flame position and the number of particles are calculated for the species conversion rates estimation in Eq. (5.16). With the result of species change within a time-step, the specific internal energy is calculated by using the same method as in Eq. (2.37).

For both CHEMKIN and FPM, the temperature change is estimated in KIVA4 by locating the specific internal energy in a pre-stored temperature vs. enthalpy database, in which interpolation might be used if needed.

5.3 Results and discussions

To validate the current model that has been integrated with KIVA-4 and also prove its better combustion prediction capability in some RCCI cases than KIVA4-CHEMKIN, validation has been conducted in 3 different duel fuel RCCI engines fueled with both diesel/gasoline and PRF. The engine specifications for these three tested engines and their operating conditions in this study are as shown in Table 5.4. The details of the experiments are discussed in the following sections separately.

Table 5.4 Engine specifications and operating conditions of the testing engines

Engine	GW4D20 diesel engine	Caterpillar engine	YANMAR L48A diesel engine
Fuel	Gasoline/diesel	PRF65	Gasoline/diesel
Bore×stroke (mm)	93.1×92	137.2×165.1	70×55
Compression ratio	16.7:1	11.6:1	19.9:1
Engine speed (rpm)	1600	1200	3000
Injection manner	Port + direct injection		
SOI (ATDC)	-35, -30, -25, -20	-100	-14
Equivalence ratio	None	0.335	None
Intake tem. (K)	368	372	375
IMEP(bar)	5.06	4.75	None

5.3.1 Great-wall diesel/gasoline duel fuel engine

The experimental data in a Great-Wall dual fuel engine fueled with 50% (by heating value) diesel and 50% gasoline, which was conducted in our previous study [133], covered different operating conditions with an injection timing sweep. In this GW4D20 single cylinder engine, AVL GH14P was employed as the in-cylinder pressure transducer. FBY-1 was used for soot measurement, whose measurement error is within ±3%. Because of 7 evenly distributed injector holes, a 51.428 degree computational grid with 8580 cells was created as shown in Figure 5.4(a). Figure 5.5 and Figure 5.6 show the in-cylinder pressure and HRR comparisons among the CHEMKIN, FPM-CHEMKIN and experimental data.

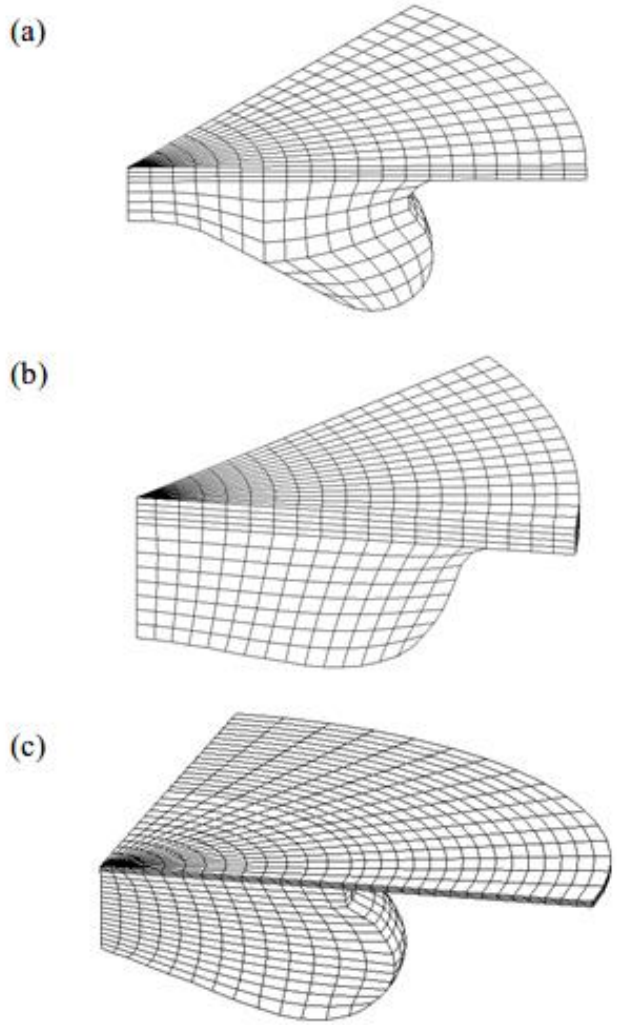

Figure 5.4 Computational girds for the testing engines at 0 deg. ATDC. (a). 45°, Great wall single cylinder engine fuelled with gasoline/diesel; (b). 45°, Caterpillar engine fuelled with PRF65. (c). 90°, YANMAR L48A diesel/gasoline dual fuel engine

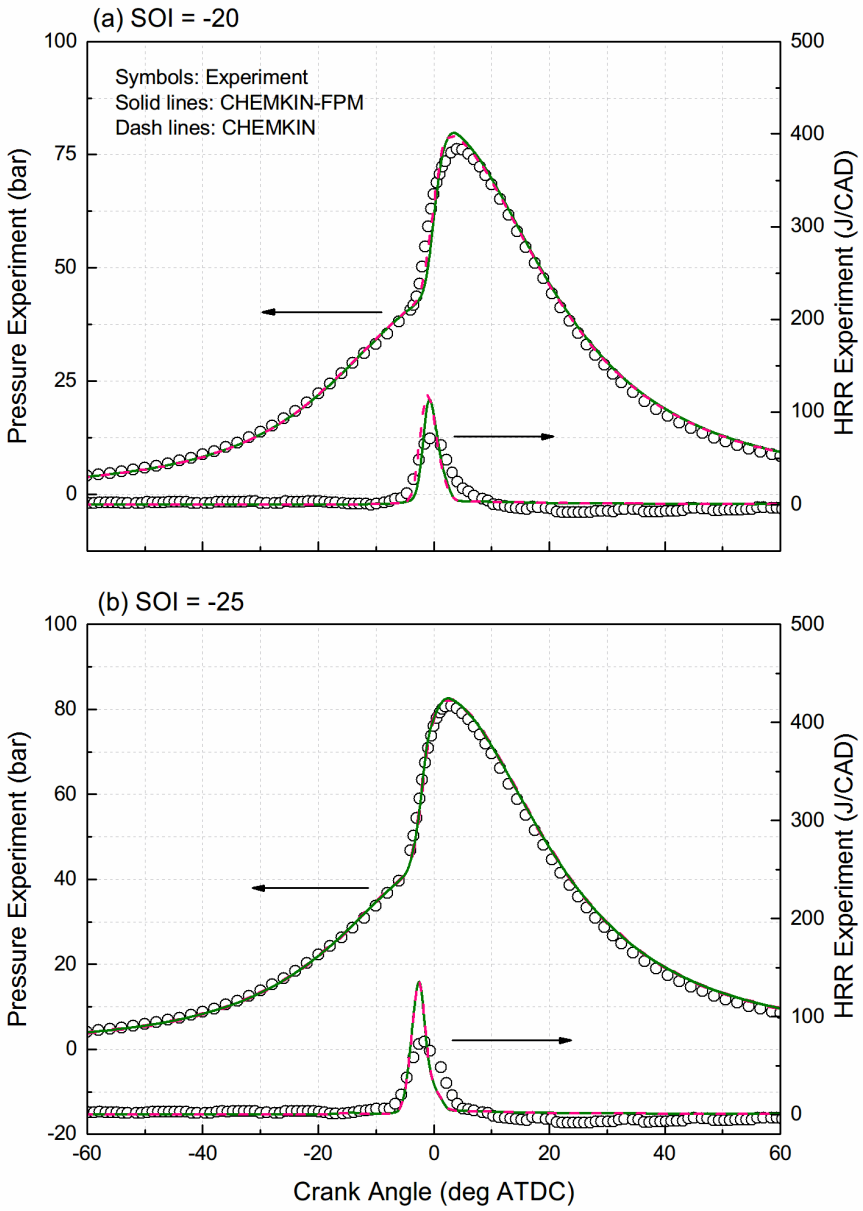

Figure 5.5 Comparisons of In-cylinder pressure and HRR as a function of crank angle under different SOIs of (a) -20 degree ATDC; (b) -25 degree ATDC. Symbols: measured data; Solid lines: computed data from CHEMKIN-FPM model; Dash lines: computed data from the CHEMKIN model

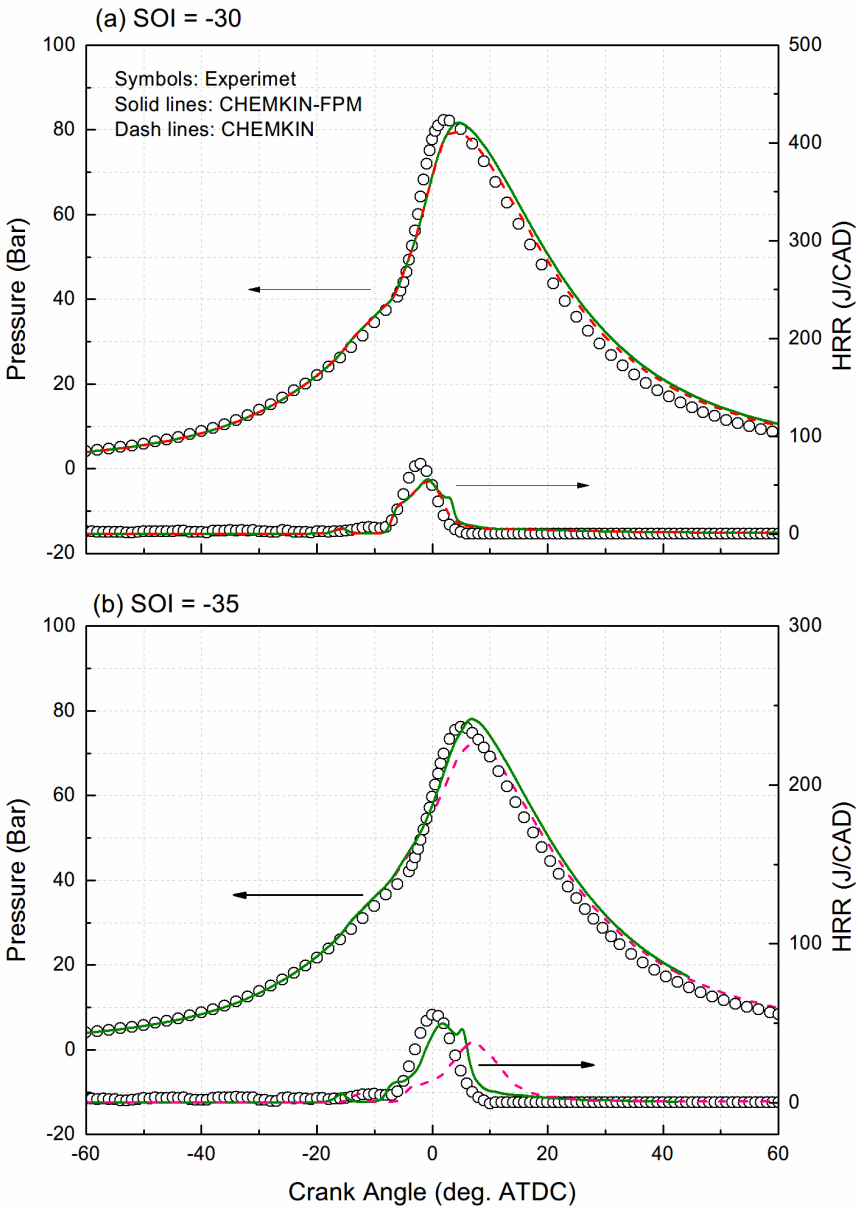

Figure 5.6 Comparisons of In-cylinder pressure and HRR as a function of crank angle under SOI of (a) -30 degree ATDC; (b) -35 degree ATDC. Symbols: measured data; Solid lines: computed data from CHEMKIN-FPM model; Dash lines: computed data from the CHEMKIN model

For the -20 ºCA and -25 ºCA start of injection (SOI) cases in Figure 5.5, it is observed that both CHEMKIN and CHEMKIN-FPM capture the measured combustion characteristics well and no obvious discrepancy was found between them. Nevertheless, for the more advanced cases of -30 ºCA and -35 ºCA in Figure 5.6, it is interesting to note that CHEMKIN underestimates the pressure

and HRR peaks while CHEMKIN-FPM improves the prediction. As known, advanced single injection timing could result in a more homogeneous mixture in the combustion chamber due to its longer ignition delay and thus more mixing time. In addition, too early an injection could lead to fuel wall-impingement, which could be developed to high temperature ignition sites, thus activating flame propagation in the RCCI partial premixed mixtures [24]. CHEMKIN coupled CFD codes shows reliable simulation performance in auto-ignition no matter whether it is a highly stratified mixing-controlled diesel diffusion combustion or a highly homogeneous kinetic-controlled HCCI combustion, but it failed to predict flame propagation controlled combustion as in a SI engine [58]. Hence, the fact that the current CHEMKIN-FPM model presented better prediction in more advanced SOI cases might be attributed to the fact that the flame propagation plays a non-negligible role in this RCCI cases.

To further prove this viewpoint, temperature contours of the -20 and -35 cases are exhibited at different crank angles in Figure 5.7. As shown in Figure 5.7 (a and e), the local maximum diesel mass fraction is observed due to the direct spray of diesel fuel. The wall impingement of diesel fuel in the -35 °CA SOI case should be noted since it turns out to be the ignition site as shown in the temperature contour at -7 ATDC (Figure 5.7(b)). Subsequently, the ignition sites trigger the flame propagation as shown in the temperature contour at -5

ATDC (Figure 5.7(c)). The combustion in the chamber consists of gasoline autoignition and flame propagation, as manifested in Fig. 7(d) by the local temperature maxima near the liner. On the contrary, in the -20 ºCA SOI case, when the combustion occurred, the local diesel mass fraction position, as indicated by Figure 5.7(e), shows a local minimum temperature (due to evaporation) in Figure 5.7(f), which implies that the combustion was triggered by the autoignition of gasoline in the high temperature zone instead of the pilot diesel injection. This fact could be further proved by the relatively homogeneous temperature distribution in the combustion chamber in Figure 5.7(h).

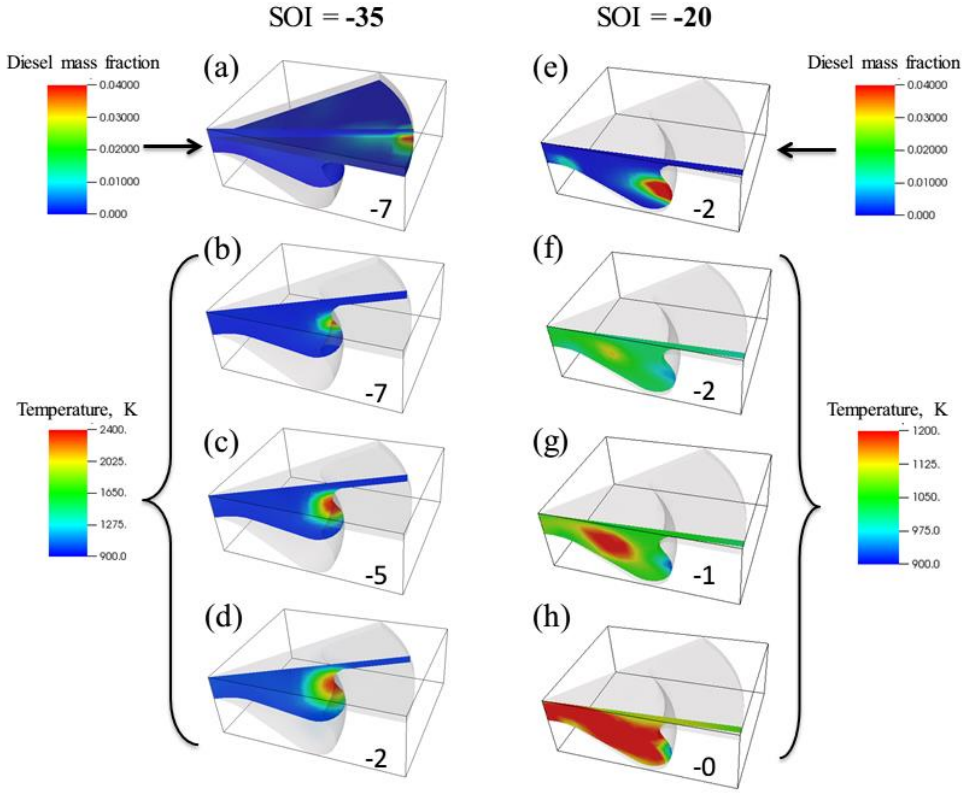

Figure 5.7 Diesel mass fraction and temperature contours. Left column, SOI = -35 deg. ATDC: (a). diesel mass fraction at -7 deg. ATDC, (b). temperature at -7 deg. ATDC, (c). temperature at -5 deg. ATDC, (d). temperature at -2 deg. ATDC. Right column, SOI = -20 deg. ATDC: (e). diesel mass fraction at -2 deg. ATDC, (f). temperature at -2 deg. ATDC, (g). temperature at -1 deg. ATDC, (h). temperature at -0 deg. ATDC

With respect to emissions, Figure 5.8 shows the NOx and soot prediction data at different direct injection timings. As shown in Figure 5.8, soot emission is captured well by the current models for both general trend and absolute value. However, the over-predicted NOx emission in CHEMKIN-FPM model could be observed. Since the NOx reactions were not considered in the flame front combustion, it is worth to point out that the difference between measured and predicted NOx might be due to the over predicted local temperature by the current FPM model instead of the conversion rate calculations. In terms of soot

emission, the CHEMKIN-FPM gives a better prediction than CHEMKIN because the local high temperature facilitates the oxidization of soot while CHEMKIN model underestimate the soot oxidization due to the overlooked flame propagation effect.

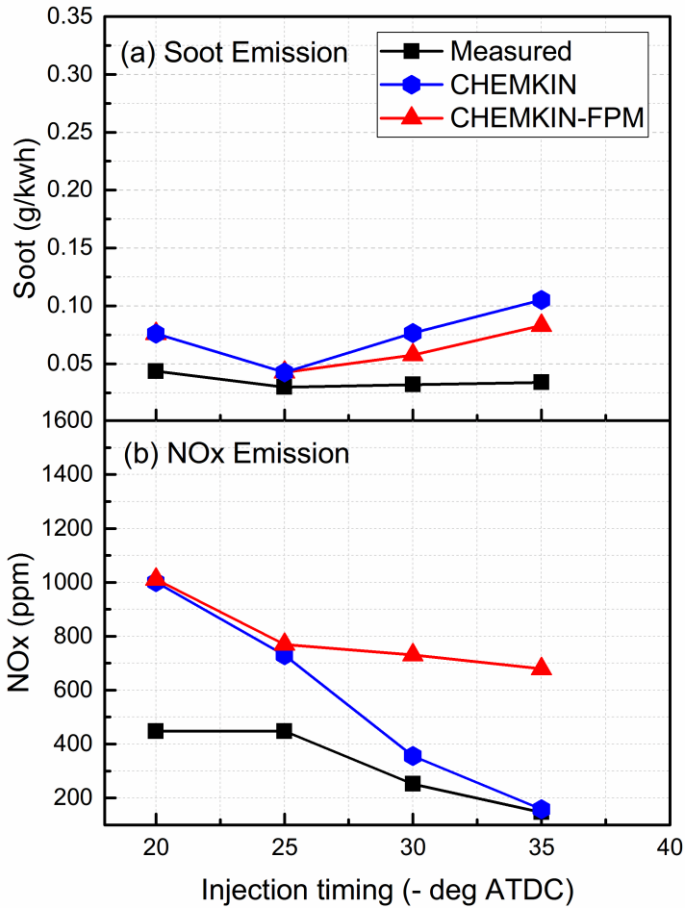

Figure 5.8 Emissions comparison among experiment, CHEMKIN and CHEMKIN-FPM at different SOI. (a). Soot emission; (b). NOx emission

This point is further proved by the soot formation and oxidization contours as shown in Figure 5.9(a). As seen in Figure 5.9(a), at 7 degree ATDC, the soot formation concentration in the calculation of CHEMKIN-FPM was larger than that in the CHEMKIN case due to the fact that the flame propagation effect accelerated the species conversion in the combustion chamber and more

precursors C_2H_2 has been formed as shown in Figure 5.9(b). However, after the oxidization of soot (i.e. at 15 degree ATDC), it is observed that the residual soot in the CHEMKIN-FMP case is less than that in the CHEMKIN case, indicating that in CHEMKIN-FMP more soot underwent the reactions as Eq. , (5.26) and (5.27) for oxidization. It is necessary to point out that in the current 4 operating conditions, all tunable constants in soot models were kept the same.

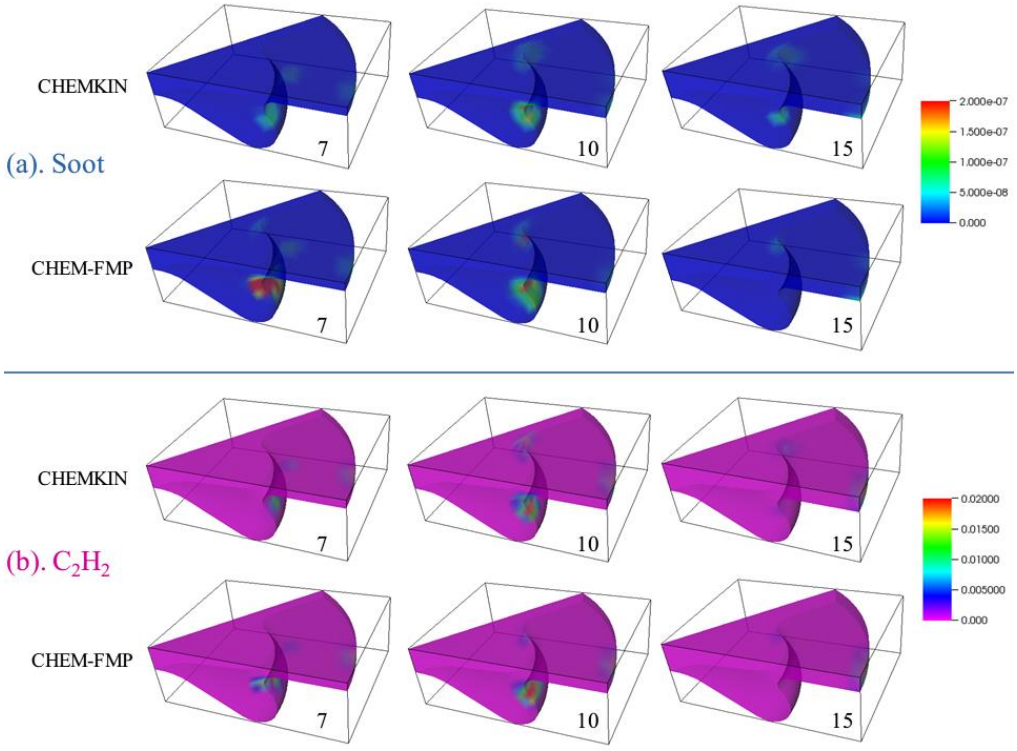

Figure 5.9 Mass fraction contours of (a) soot; (b) C_2H_2 at 7, 10 and 15 degree ATDC calculated with CHEMKIN and CHEMKIN-FMP, respectively

5.3.2 Caterpillar PRF65 dual-fuel engine

To elaborate the role of flame propagation in RCCI engines, a more advanced direct injection dual fuel engine fueled with PRF65 [148] were used to validate the current models. To measure the cylinder pressure in this heavy-duty 2.44L Caterpillar 3401 engine, Kislter model 6067C1 water-cooled

pressure transducer in conjunction with a Kistler model 510 charge amplifier were used in Ref. [148]. Acquired cylinder pressure traces were averages for 100 cycles. The operating conditions are shown in Table 5.4. The created mesh is with 9520 cells as shown in Figure 5.4(b). A super advanced single injection timing of -100 ATDC was selected. The simulation results are shown in Figure 5.10. Still, the CHEMKIN simulation results are used as a comparison here. It is clearly observed that in this case, the FPM show nothing different in terms of combustion characteristics from the CHEMKIN simulation results. This result is counterintuitive since in the former validations, a more advanced SOI makes flame propagation more crucial in a RCCI engine. The simulation results here show that the advanced injection timings could make a nearly homogeneous mixture, in which, if the conditions allowed (enough oxygen concentration and temperature), autoignition will control the combustion, as in this case. Hence, a far more advanced SOI would result in the fact that the direct injection diesel cannot ignite the mixture because of a local temporal low temperature, which in turn, leads to a well-premixed diesel with the air and gasoline mixture. Hence, its kinetic time scale becomes dominant and the combustion turns into a kinetic-controlled combustion, like in the HCCI. This result implies that a far more advanced SOI in a well-conditioned mixture could suppress flame propagation, in which the current model could show a very similar prediction as CHEMKIN.

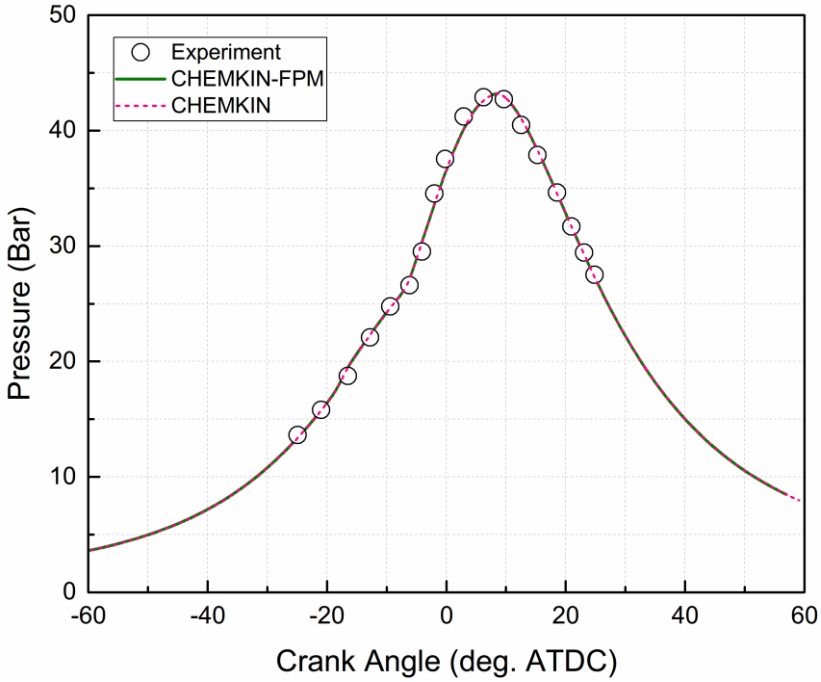

Figure 5.10 In-cylinder comparison between experimental data and CHEMKIN, CHEMKIN-FPM data of the Caterpillar PRF65 engine

5.3.3 YANMAR L48A diesel/gasoline dual fuel engine

The results in the previous discussions are further proved by applying the current model in a lean gasoline/air mixture with a -14 °CA direct diesel injection dual fuel engine, in which, as stated by Yoshida et al. [42], the flame propagation will control the combustion. The mixing region was formed in this engine by the diesel fuel injection and the entrainment of ambient mixture. The mixture combustion was triggered in this mixing region and burned by flame propagation. The operating conditions are also shown in Table 5.4. The created mesh is with 14720 cells as shown in Figure 5.4(c). Three different fuel compositions were used in the experiment, namely, direct-injected diesel without entrainment gasoline, entrainment mixture with an air/gasoline mass ratio of 128.0 and an air/gasoline mass ratio of 54.7. All these three cases

employed a diesel injection with a flow rate of 0.06g/s. To simulate these operating conditions in the experiments, a 90 degree computational grid was created because of the 4 evenly distributed injector holes. All the gasoline and air was assumed homogeneously distributed in the combustion chamber initially in the simulation.

The direct-injected diesel case is also given in Figure 5.11 for comparison with other flame propagation controlled cases. No obvious difference in the in-cylinder pressure prediction is observed between CHEMKIN and CHEMKIN-FPM for the pure diesel case. This is attributed to the fact that conventional diesel combustion is a type of highly stratified diffusion combustion, in which the combustion is organized by a diffusion flame instead of by flame propagation. Therefore, it could be well captured and simulated by the CHEMKIN combustion models and the FPM will play a trivial role because of the strained local conditions for flame propagation in the ignition cell in the computational domain.

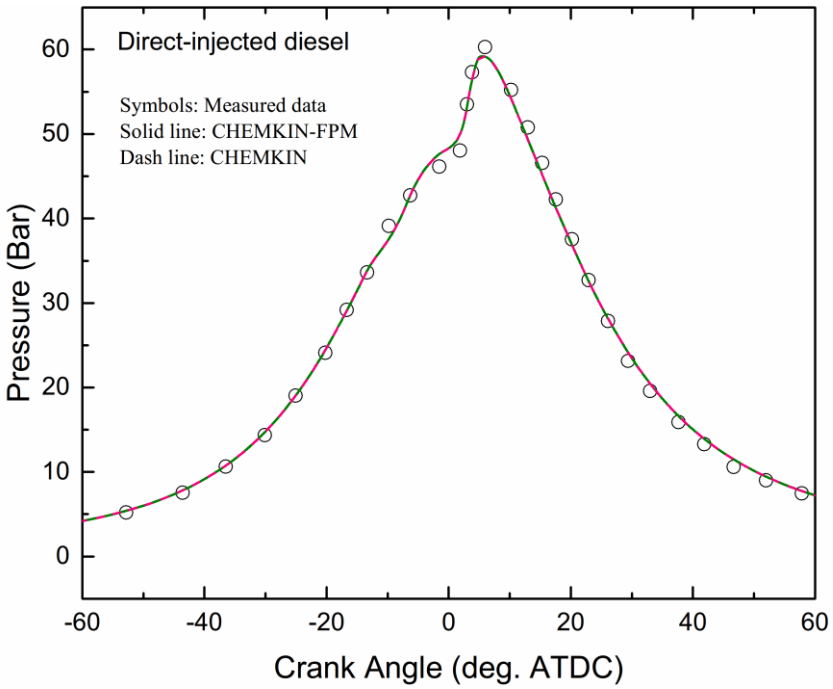

Figure 5.11 In-cylinder comparisons between the experiment data and CHEMKIN, CHEMKIN-FPM predicted data with pure diesel as the fuel

For the other two cases, all the engine parameters were kept the same as in the direct-injected diesel case in the simulations, except for gasoline addition in the entrainment air mixture. In these two cases, the combustion is supposed to be controlled mainly by the flame propagation, as implied in the experiment. Hence, one expects a failure by using CHEMKIN as the combustion model to predict the combustion characteristics. The simulation results shown in Figure 5.12 demonstrate perfectly that CHEMKIN failed to predict the dual fuel combustion in these operating conditions. As observed in Figure 5.12, due to the neglect of flame propagation triggered by diesel ignition, the ignition delay was mismatched with the experiment and thus the pressure peak was erroneously underestimated by CHEMKIN. However in CHEMKIN-FPM in the current model, the ignition delay and pressure trace were reasonably

captured. Moreover, as shown in the temperature spatial contours, at 3 degree ATDC where the pressure starts to rise in the CHEMKIN-FPM case, the auto-ignition sites have developed into local high temperature region because of the flame propagation, which subsequently, controlled the combustion as shown in the following contours at 4 and 5 degree ATDC. In contrast, the lack of flame propagation modeling in the CHEMKIN model restricted the combustion initialization to autoignition, thereby suppressed the combustion development as shown in the temperature contours at 3 and 4 degree ATDC. The same observation can be obtained in Figure 5.13 with a different air/fuel ratio. Therefore, it is concluded that in the wide operating condition regime of RCCI combustion, the FPM-CHEMKIN model in the current study could provide better predictions than CHEMKIN, especially when the combustion is organized by flame propagation.

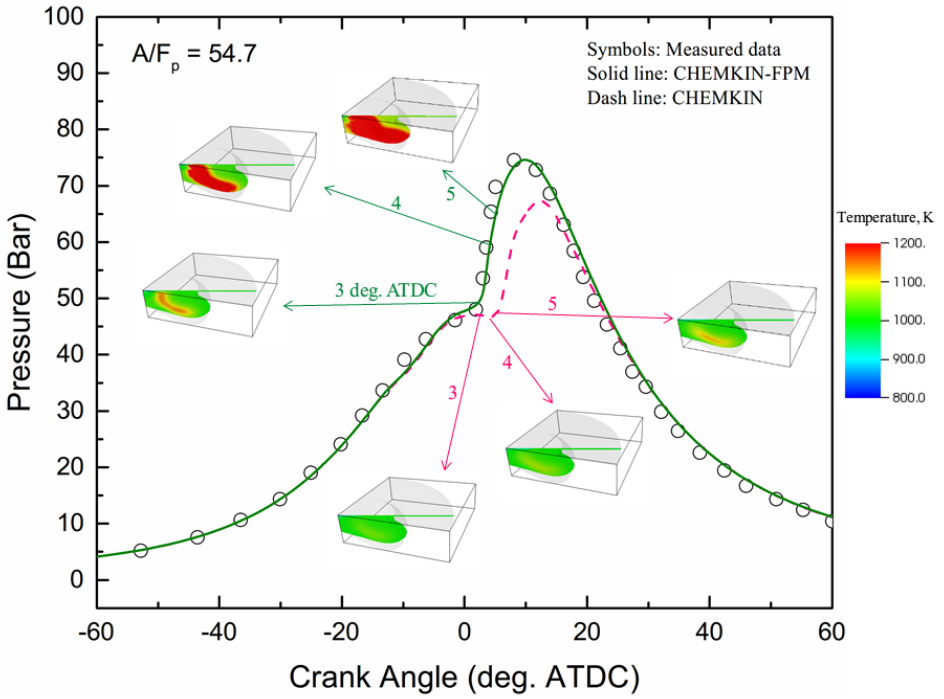

Figure 5.12 In-cylinder comparison between the experiment data and CHEMKIN, CHEMKIN-FPM predicted data (A/F$_p$=54.7, A/F$_p$ is the mass ratio of air to premixed fuel), with superimposed spatial temperature contours at 3, 4, 5 deg. ATDC

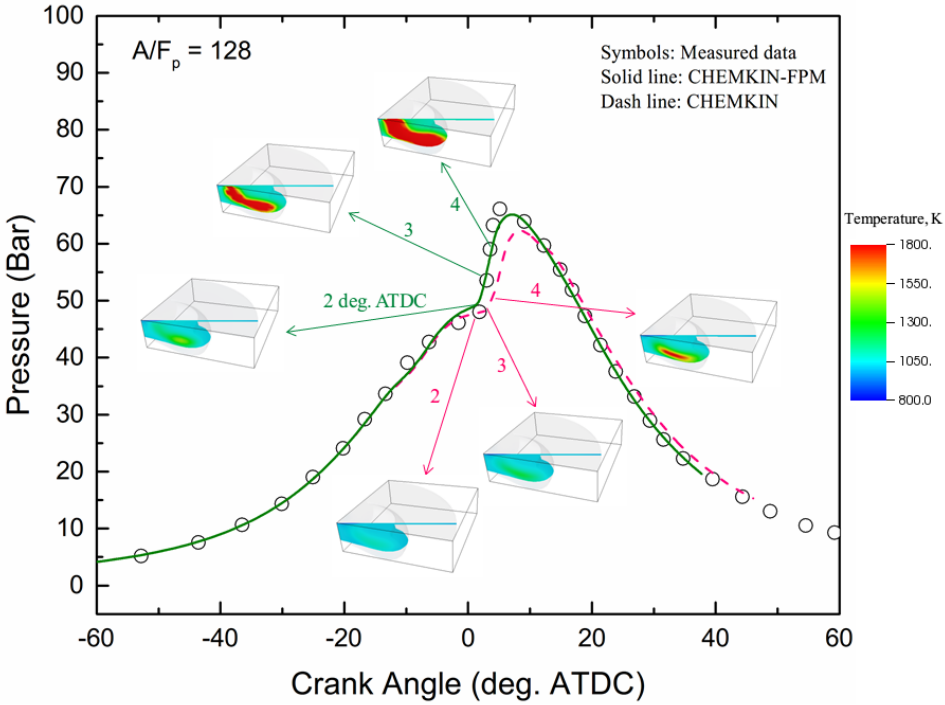

Figure 5.13 In-cylinder comparison between the experiment data and CHEMKIN, CHEMKIN-FPM predicted data (A/F$_p$=128, A/F$_p$ is the mass ratio of air to premixed fuel), with superimposed spatial temperature contours at 3, 4, 5 deg. ATDC

5.4 Conclusion

A new combustion model, which considers flame propagation in partially premixed combustion in internal combustion engines was proposed and coupled into the CFD framework code KIVA-4. In the formulation of the FPM model, a new PRF flame speed correlation was proposed. Detailed chemical kinetics was also coupled into this FPM model by assuming local equilibrium in the flame front and then solving the local equilibrium species and adiabatic temperature by a CEQ solver. Based on sub-grid burnt and unburnt volumes, the species conversion rate and thus the energy and temperature change were calculated within the turbulence flame front brush.

In addition, by coupling a phenomenological soot model into the current framework for soot prediction, together with a NOx sub-mechanism in the chemical kinetic PRF mechanism, the integrated model was used to predict combustion characteristics and emission under different combustion regimes in 3 different engines with different SOI and premixed fuel ratios. The predictions by this model obtain better agreement with the experimental data in terms of combustion characteristics and emissions. The results also show that CHEMKIN with KIVA-4 could fail for certain cases of RCCI combustion when flame propagation is dominant. In those cases, the current CHEMKIN-FPM model, however, could more precisely predict the combustion characteristics.

In the future study, a detailed sensitivity analysis of the constants *NP* could

be conducted to obtain a correlation between *NP* and number of cells of the mesh used. A sensitivity analysis of the critical temperature to T_c could also be conducted for insight of the current flame initialization phenomena in the computational domain. It is also to be noted that the current FPM mode was developed and implemented with the CFD framework KIVA-4 thus should only be applied within Reynolds-averaged Navier–Stokes (RANS) simulations.

The current integrated KIVA4-CHEMKIN-FPM could be used for future RCCI engine simulations since it gives proper predictions of the combustion characteristics and emissions under wide operating conditions no matter whether the combustion is controlled by premixed auto-ignition, diffusion flames or flame propagation.

Chapter 6 Computation Acceleration of RCCI Modeling

6.1 Introduction

Efficiency is one of the most critical factors we need to consider when simulating multidimensional engines. However, because of the large size of realistic fuel mechanism and the stiff chemistry as discussed in Section 2.2.3, the cost of the chemical source term integration dominates the computational efforts. Specifically in RCCI engine simulations, the low-intermediate temperature combustion of the premixed fuel in the combustion chamber causes the chemistry integration to start at an early stage and thus prolongs the chemistry integration process in the simulation. Moreover, unlike the CDC which could reach equilibrium in the post-combustion phase, RCCI combustion tends to be with high hydrocarbon residue, leading to no alleviation of the stiffness in the post-combustion stage.

Hence, this chapter aims at developing schemes and algorithms to accelerate RCCI engine simulations. First of all, a chemistry integrator parallel computing algorithm was proposed and then implemented based on the MPI architecture. This method is proved to be very effective to reduce the CPU cost. Then, a heterogeneous multiscale method (HMM) is proposed for integrating the stiff chemistry, as a substitute of the implicit integrator VODE. This method

is validated in both 0-D auto-ignition and 3-D partially premixed combustion engines and proved to be very efficient.

6.2 Parallel computing algorithm for chemical solver

In the original KIVA-4 code, CPU integrates the stiff combustion serially from the first computational cell to the last one. Due to the expensive chemical integration process, with increase of the grid cell quantity, the computational time grows geometrically. Hence, a natural solution is to parallelize the chemistry integrator. As such, a parallel computing method based on MPI was embedded into the coupled KIVA4-CHENMKIN code. A schematic flow chart to show the comparison of serial and parallel computation is illustrated in Figure 6.1. As shown in Figure 6.1, in the original serial computing, the stiff chemistry in each cell is integrated from the first cell to the last one. However, in the chemistry integration process in parallel computing, the state variables in the master core are broadcasted to all the slave cores. If m is the total computational cell number and n is the core number, every slave core takes a workload of m/n cells. If n isn't evenly divisible by m, the remainder will be iteratively one-by-one distributed to each slave core until it is completely allocated. In each slave core, a serial of ODEs are constructed based on the state variables and then solved by VODE. The updated species concentrations in each slave core are subsequently sent back to the master core.

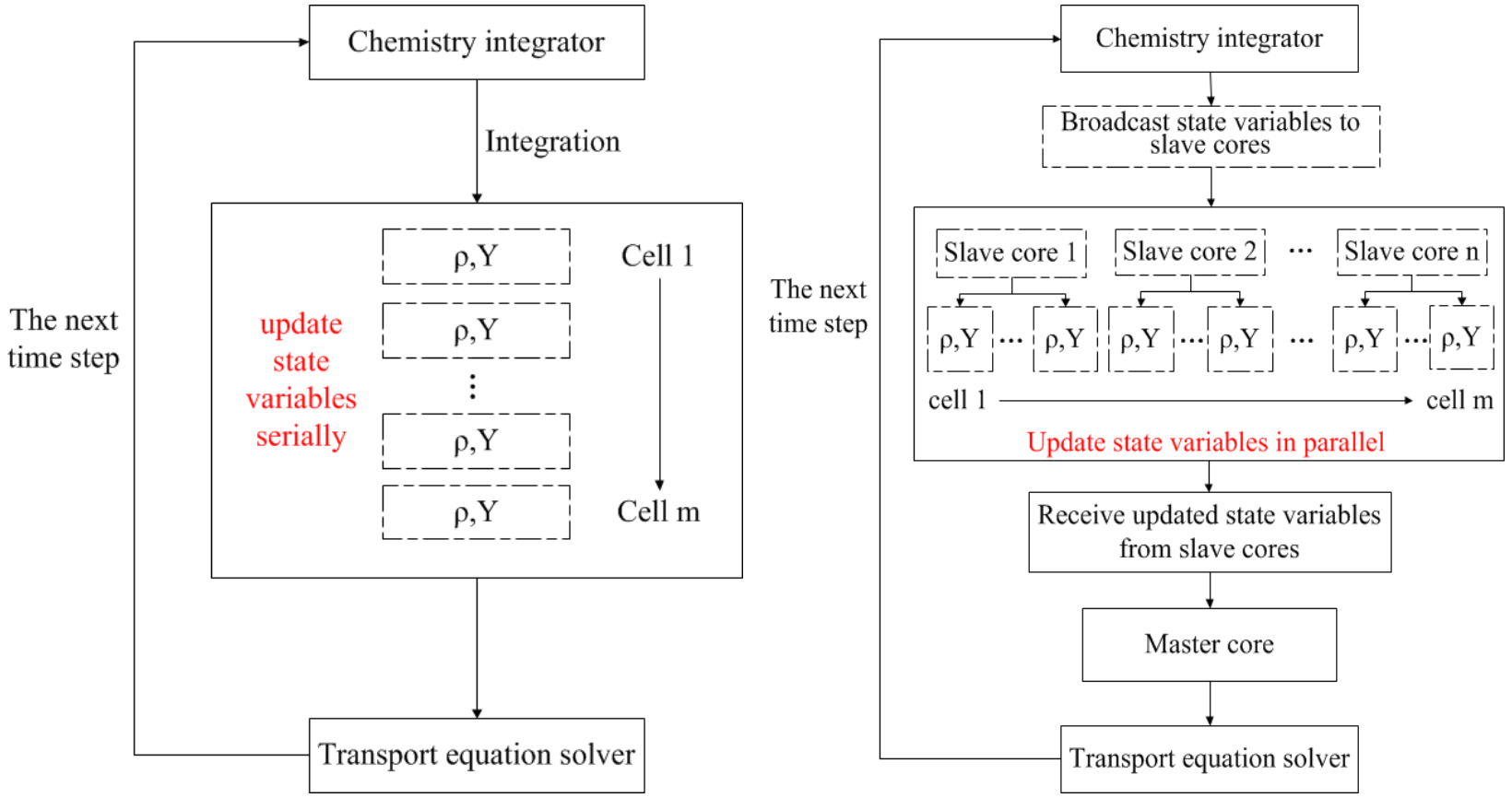

(a) Serial computing (b) Parallel computing

Figure 6.1 Schematic flow chart of (a) serial computing, (b) parallel computing in KIVA-4 CHEMKIN codes

To test the performance of this parallel computing algorithm, 3 parallel computing cases with 8, 12 and 16 cores were tested and compared with the case of serial computing. The operating conditions and engine specifications are listed in Table 6.1. A 60° sector computational grid was created due to 6 evenly-distributed holes in the injector, as shown in Figure 6.2. The simulations are of closed cycles, starting from the inlet valve closure and ending at the exhaust valve open. All the simulation cases were submitted to be running at the HPC Center at NUS with a CPU speed of 2.76 GHz.

Table 6.1 Engine specifications and operating conditions in parallel computing cases

Engine Type	Toyota four-cylinder DI diesel engine
Bore & Stroke	92mm & 93.8mm
Compression ratio	18.5
Charging	Turbocharged
Rated power	75kW at 3600 rpm
Fuels	Port-injected Methanol direct-injected biodiesel
Premixed fuel ratio	60% (by mass)
EGR rate	20%
Inlet valve closure	-149 deg. ATDC
Exhaust valve open	150 deg. ATDC

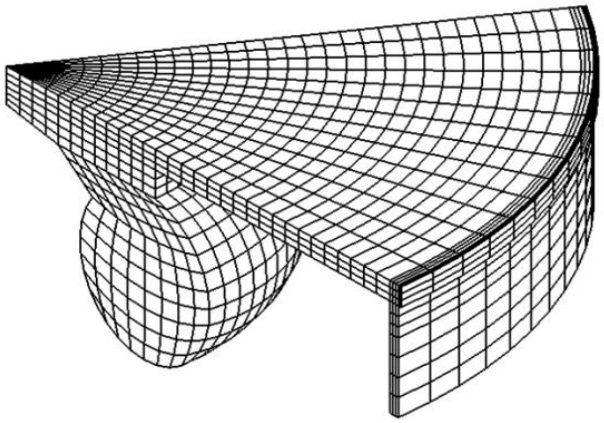

Figure 6.2 60° Computational gird for the testing engine at 0 deg. ATDC.

The predicted pressure traces as a function of crank angle by this parallel computing algorithm with different CPU cores are compared with the results by serial computing, as shown in Figure 6.3. It is seen that the predicted pressure profiles are identical, indicating good predictability of the current parallel computing algorithm.

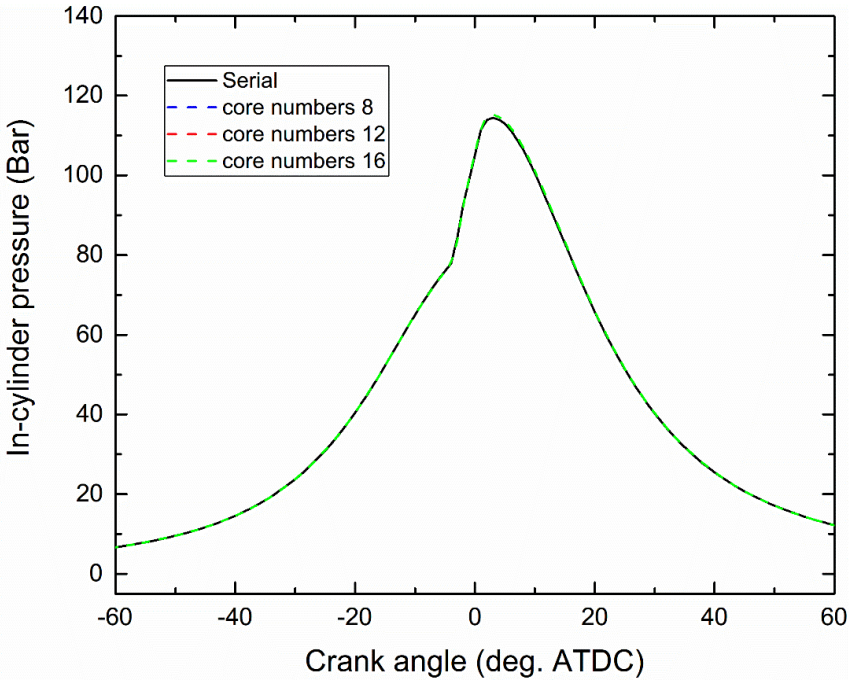

Figure 6.3 Comparison of in-cylinder pressure traces as a function of crank angle, calculated by serial computing and parallel computing with 8, 12 and 16 CPU cores

Meanwhile, the simulation CPU cost of this parallel computing scheme was compared with that of the serial computing to show the efficiency improvement. Moreover, the efficiency with different CPU core numbers was compared with each other to show the relation between CPU core number and simulation time. The serial computing here is deemed as a one-core parallel computing case for comparison. As shown in Figure 6.4, with the increased core numbers, the simulation CPU cost is dramatically reduced. As a reference, a hyperbolic line is also shown in Figure 6.4. It is noted that the CPU cost does not decrease hyperbolically with the dash line. This might be attributed to the fact that the CPU cost also includes the computational time in flow fluid calculations besides the chemistry integration. Moreover, more slave cores imply more time spent on the message communication between the master and slave cores. Based on this observation, it is not recommended to adopt arbitrarily large core numbers when using this parallel computing algorithm.

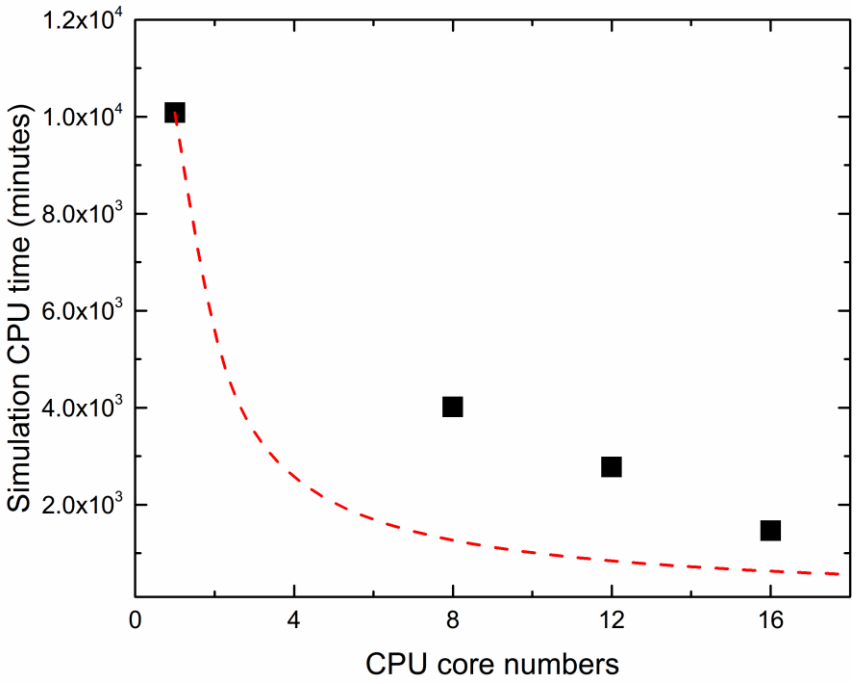

Figure 6.4 Simulation CPU cost with different CPU core numbers (1, 8, 12 and 16). The red dash line is a hyperbolic line that crosses the point with 1 CPU core

In sum, it is seen that the current parallel computing algorithm is promising to reduce the computational overhead (i.e., nearly 5 times with 12 CPU cores). More importantly, it is based on the sequence of how the chemical integrator solve the chemistry in each cell and does not modify the internal ODEs solver, implying that other advanced ODEs integration schemes could be adopted to possibly further reduce the computational cost.

6.3 Heterogeneous multiscale method in stiff chemistry integration

HMM is a general framework for designing multiscale methods toward various applications. By taking advantage of the simplicity and efficiency of the macroscopic model for large scale variables and the accuracy of the microscopic model for small scale variables, HMM is able to resolve the multiscale system accurately and efficiently. The spirit of HMM has been

applied in various research fields, including fluid flow, solids, stochastic problems, interface problems, and statistically self-similar problems [149]. In this section, the philosophy of HMM is applied to stiff chemistry integration.

6.3.1 Approach

Basics of combustion chemistry in reactive flows

The chemical mixture in the reactive flow is assumed to consist of N species and their chemistry dynamics is determined by a mechanism with I reactions. To avoid complex description of the governing equations in reactive flows and yet without losing generality, the system could be simplified as:

$$\frac{D\boldsymbol{\Phi}}{Dt} = \boldsymbol{\omega}(\boldsymbol{\Phi}) + \boldsymbol{\Omega}_1 \tag{6.1}$$

$$\boldsymbol{\Phi} = [\, y_1, ..., y_n, ..., y_N, T \,]^T \tag{6.1a}$$

$$\boldsymbol{\omega} = [\, \omega_1, ..., \omega_n, ..., \omega_N, \dot{T} \,]^T \tag{6.1b}$$

where the subscript n indicates the n-th species, y_n, T, ω_n are the species concentration, temperature and net production rate, respectively. $\boldsymbol{\Omega}_1$ is the source term vector including diffusion and other source terms of the state variables. $\dot{T}$ is the temperature changing rate, which in constant pressure process could be written as:

$$\dot{T} = -\sum_{i=1}^{N} h_n \omega_n / \rho c_p \tag{6.2}$$

where h_n, ρ, c_p are the enthalpy of Species n, density and heat capacity,

respectively. The LHS of Eq. (6.1) is a material time derivative, which includes the convection source term. To illustrate the stiffness involved in Eq. (6.1), by excluding the temperature out of $\boldsymbol{\Phi}$ (indeed, the temperature timescale is typically too large to cause any stiffness in the system), Eq. (6.1) can be put as this way:

$$\frac{D\boldsymbol{\Phi}}{Dt} = -\boldsymbol{D} + \boldsymbol{\Omega}_2 = -\frac{\boldsymbol{\Phi}}{\boldsymbol{\tau}} + \boldsymbol{\Omega}_2 \tag{6.3}$$

$$\boldsymbol{D} = [\, D_1, ..., D_n, ..., D_N \,]^T \tag{6.3a}$$

$$\boldsymbol{\tau} = [\, \tau_1, ..., \tau_n, ..., \tau_N \,]^T \tag{6.3b}$$

$$\tau_n = \frac{y_n}{D_n} \tag{6.3c}$$

where D_n is the species concentrations destruction rate of Species n; τ_n is the timescale of Species n ; $\boldsymbol{\Omega}_2$ is the source terms vector including diffusion, creation rate of the species concentrations and other slow source terms.

If all the terms in Eq. (6.3) are normalized by some factor so that y_n turns to the species mass fraction and $y_n = O(1)$, the stiffness of Eq. (6.3) lies in the fact that under some conditions there exists some $\tau_n = O(\varepsilon)$, where ε is extremely small compared with unity, even smaller than the typical size step in DNS (e.g. 10 ns). Thus, a size step which should be smaller than the minimum timescale is necessary to resolve the system explicitly. By separating the stiff variables (timescale smaller than the step size in the reactive flow) from the slow ones (timescale larger than the step size in the reactive flow), Eq. (6.3) is

then reformulated as:

$$\frac{D\boldsymbol{\Phi}}{Dt} = -\frac{\boldsymbol{\Phi}_f}{\boldsymbol{\tau}_f} - \frac{\boldsymbol{\Phi}_s}{\boldsymbol{\tau}_s} + \boldsymbol{\Omega}_2 \tag{6.4}$$

where the subscript *f* indicates fast and *s* implies slow. With Eq. (6.4), one would tend to solve the equations with a semi-implicit scheme by resolving the fast variables implicitly and the slow variables explicitly which, actually, has been adopted by some researchers [101, 150].

Basics of HMM

In ODEs system, taking Eq. (6.4) as an example, one can easily speculate that HMM would solve the small time-scale variables with a micro-model while the large time-scale variables would be dealt by a macro-model. In this section, we will generally show the algorithm based on HMM for solving stiff ODEs. Its implementation in combustion chemical kinetics will be presented in the next section.

If the fast and slow variables can be explicitly identified in the system, consider the system of ODEs [151]:

$$\begin{aligned} \dot{x} &= -\frac{1}{\varepsilon}(x - f(y)) \\ \dot{y} &= g(x, y) \end{aligned} \tag{6.5}$$

If ε is small, the variables *x* evolve much faster than the variables *y* on a $O(\varepsilon)$ timescale, which, in turn, leads to its fast dynamics being attracted to the slow manifold where $x = f(y) + O(\varepsilon)$. Hence, making use of this property, we

can choose a microscopic solver to integrate the fast variables, e.g. a forward Euler scheme:

$$x^{n,m+1} = x^{n,m} - \frac{\delta t}{\varepsilon}(x^{n,m} - f(y^n)), m = 0,1,...,M-1 \tag{6.6}$$

where n indicates the current global step; m is the current micro integration step; δt is the step size in the micro-solver; M is the total number of integration steps in the micro-solver, which should be chosen large enough so that the fast variables converge to a quasi-stationary value. Noted that during the integration as in Eq. (6.6), the slow variables y^n are fixed. The constrained slow variables in Eq. (6.6) could obtain better accuracy than simultaneously integrating the slow variables in Eq. (6.6) [151]. Having integrated the fast variables, we then fix them and estimate the motion of slow variables by:

$$\tilde{g}(y^n) = \frac{1}{M}\sum_{m=0}^{M-1} K_{m,M}\, g(x^{n,m}, y^n) \tag{6.7}$$

where $K_{m,M}$ should satisfy the normalization constraints:

$$\frac{1}{M}\sum_{m=0}^{M-1} K_{m,M} = 1 \tag{6.8}$$

Hence, use the estimated $\tilde{g}(y^n)$ in Eq. (6.7) to make a macro-step for the slow variables and get y^{n+1} by e.g. a forward Euler scheme:

$$y^{n+1} = y^n + \Delta t\, \tilde{g}(y^n) \tag{6.9}$$

Eq. (6.6)-(6.9) are the typical procedures for solving ODEs by HMM. Eq. (6.6) is the micro-step; Eq. (6.7) is the estimator step; Eq. (6.9) is the macro-step.

After this process, the global step moves forward for one step.

It is interesting to be noted that in Eq. (6.8), the options of $K_{m,M}$ should be chosen to best approximate the invariant density of the fast variables [152]. A very natural option of the weights in Eq. (6.8) is to set:

$$K_{n,M} = \begin{cases} M, m = M \\ 0, m < M \end{cases} \tag{6.10}$$

which is also adopted in the current study for its implementation in combustion chemistry. Another interesting point to be noted is that for illustration, the integrators in Eq. (6.6) and Eq. (6.9) are a simple forward Euler scheme. In the application of HMM, however, the integration in the micro and macro steps can be conducted either explicitly or implicitly with first-order or high-order accuracy. Moreover, the micro step and estimator step could be conducted iteratively if the ODEs system has more than 2 groups of variables with distinct scales.

6.3.2 HMM implementation in combustion chemistry

HMM for stiff combustion chemistry

In a reactive flow simulation, there are a global time step Δt_g and an inner time step Δt_{in} during a global integration. Before the integration of each inner time step, by defining that each neighboring species group has a different magnitude of timescale, the species are classified into N_m groups:

$$N_m = Log_{10}(\frac{\Delta t_{in}}{\tau_{min}}) + 1 \tag{6.11}$$

where τ_{min} is the minimum timescale of all the species. The group index of a species with a timescale τ_i is obtained by:

$$N_i = Log_{10}(\frac{\Delta t_{in}}{\tau_i}) + 1 \tag{6.12}$$

The ideal implementation of HMM (name this implementation as Integration A) in the combustion chemistry is as followed (micro and macro solvers are both assumed to be Euler forward scheme for illustration):

1. Identify the number of groups and the group index of each species by Eq. (6.11) and (6.12). Species whose timescales are larger than the inner time step Δt_{in} are slow variables, while species whose timescale are smaller than the inner time step Δt_{in} are fast variables. It is noted that with Eq. (6.12), the group index of all the slow species is 1.
2. Use $\boldsymbol{\Phi}_{N_i}$ to represent the variables with a group index of *i*. Then the first group $\boldsymbol{\Phi}_1$ includes all the slow variables while $\boldsymbol{\Phi}_2$, $\boldsymbol{\Phi}_3$, … , $\boldsymbol{\Phi}_{N_i}$, … , $\boldsymbol{\Phi}_{N_m}$ represent the fast variables with timescales of different orders of magnitude. Recall Eq. (6.4) and integrate the fast variables hierarchically with a micro solver with constrained slow variables.

   For $N_i = N_m$ (the fastest group),

$$\boldsymbol{\Phi}_{N_m}^{m+1} = \boldsymbol{\Phi}_{N_m}^{m} + \delta t_{N_m}\left[-\boldsymbol{D}(\boldsymbol{\Phi}_2^m, ..., \boldsymbol{\Phi}_{N_m}^m, \boldsymbol{\Phi}_1^0) + \boldsymbol{\Omega}_2\right] \tag{6.13}$$

$$\delta t_{N_m} = \Delta t_{in} / 10^{(N_m - 1)} \tag{6.13a}$$

   where δt_{N_m} is the time step of group N_m; the superscript *m* indicates the integration step in the micro solver. After M_{N_m} steps integration in Eq.

(6.13) so that $||\boldsymbol{\Phi}_{N_m}^{m+1}||$ converges to quasi-stationary values with desired accuracy, fix the values of this group and go to the slower groups.

Generally, for $N_m \geq N_i > 1$,

$$\begin{aligned}\boldsymbol{\Phi}_{N_i}^{m+1} = \boldsymbol{\Phi}_{N_i}^{m} + \delta t_{N_i}[-\boldsymbol{D}(\boldsymbol{\Phi}_2^m,...,\boldsymbol{\Phi}_{N_i-1}^m,\boldsymbol{\Phi}_{N_i}^m,\\ \boldsymbol{\Phi}_{N_i+1}^{M_{N_i+1}},...\boldsymbol{\Phi}_{N_m}^{M_{N_m}},\boldsymbol{\Phi}_1^0)+\boldsymbol{\Omega}_2]\end{aligned} \tag{6.14}$$

$$\delta t_{N_i} = \Delta t_{in} / 10^{(N_i-1)} \tag{6.14a}$$

where δt_{N_i} is the time step of group N_i. After M_{N_i} steps integration as Eq. (6.14) so that $||\boldsymbol{\Phi}_{N_i}^{m+1}||$ converges to quasi-stationary values with desired accuracy, fix this group and go to the slower groups.

Repeat this step until $N_i = 2$ so that all the fast variables are converged to stationary values.

3. Integrate the slow variables by:

$$\boldsymbol{\Phi}_1^1 = \boldsymbol{\Phi}_1^0 + \Delta t_{in}\left[-\boldsymbol{D}(\boldsymbol{\Phi}_2^{M_1},...,\boldsymbol{\Phi}_{N_i}^{M_{N_i}},...,\boldsymbol{\Phi}_{N_m}^{M_{N_m}},\boldsymbol{\Phi}_1^0)+\boldsymbol{\Omega}_2\right] \tag{6.15}$$

4. Reinitialize the state variable vector by:

$$\boldsymbol{\Phi}^0 = [\boldsymbol{\Phi}_1^1,\boldsymbol{\Phi}_2^{M_2},...,\boldsymbol{\Phi}_{N_i}^{M_{N_i}},...,\boldsymbol{\Phi}_{N_m}^{M_{N_m}}]^T \tag{6.16}$$

5. Go to step 1 if having not reached the end of the global integration time.

It needs to point out that for DNS simulations, the global time step is small enough (e.g. 10 ns) to ensure the sparse coupling of the fast chemical processes, thus could be taken as the inner time [80]. However, in large eddy simulations (LES) and RANS where larger global time step size is adopted, the densely-coupled fast chemical processes, particularly the fast partial-equilibria

reactions are common. Hence, to apply step 2 in Integration A without causing unacceptable errors, a smaller inner time step is necessary. Hence in this study, an adaptive time step scheme is proposed to estimate the inner time step based on a predictor-corrector algorithm, which will be introduced in the next section.

Consequently, if the inner step size is not smaller than a critical step size t_c, all of the variables will be integrated in the macro solver, leading to a macro solver in this modified implementation of HMM (name it as Integration B) an implicit solver:

1. (a). If the inner time step is larger than t_c, directly integrate all the variables by a second order trapezoidal rule:

$$\boldsymbol{\Phi}^{n+1} = \boldsymbol{\Phi}^{n} + \frac{1}{2}\Delta t_{in}\left[-\boldsymbol{D}(\boldsymbol{\Phi}^{n+1}) - \boldsymbol{D}(\boldsymbol{\Phi}^{n}) + 2\boldsymbol{\Omega}_2\right] \tag{6.17}$$

Eq. (6.17) is typically a nonlinear system, which should be solved by some iterative method such as the Newton method. In the current study, Eq. (6.17) is solved by an inexact Newton method globalized by backtracking with a Krylov subspace trial step obtaining method [153].

(b). If the time step is smaller than t_c, then integrate through step 1-3 in Integration A, replacing the first Euler scheme in Eq. (6.15) by:

$$\begin{aligned}\boldsymbol{\Phi}_1^1 = \boldsymbol{\Phi}_1^0 + \frac{1}{2}\Delta t_{in}[&-\boldsymbol{D}(\boldsymbol{\Phi}_2^{M_1},\ldots,\boldsymbol{\Phi}_{N_i}^{M_{N_i}},\ldots,\boldsymbol{\Phi}_{N_m}^{M_{N_m}},\boldsymbol{\Phi}_1^0) \\ &-\boldsymbol{D}(\boldsymbol{\Phi}^1) + 2\boldsymbol{\Omega}_2]\end{aligned} \tag{6.18}$$

2. Modify the inner time step by an adaptive time step scheme to control the error, which will be introduced later.

3. Reinitialize the state variable vector by replacing the initial values by the updated ones as Eq. (6.16).
4. Go to step 1 if having not reached the end of the global integration time.

An adaptive time step scheme for HMM in reactive flows

In some LES and RANS simulations, the global time step could be relative large (e.g. 1.0^{-6} s), for which a smaller inner time step should be adopted to accurately resolve the system. Hence in this study, an adaptive time step modification scheme was proposed. It is based on a predictor-corrector procedure and customized for the HMM implementation in this study.

Firstly, we estimate the initial time step by a Euclidean norm:

$$\Delta t_{in} = 10^{-6} / || \omega_i \cdot mw_i / \rho || \tag{6.19}$$

where mw_i is the molecular weight of Species i. We then give a first order prediction for the species concentrations y_i with the current inner time step by a QSS predictor as in [95]:

$$y_i^p(\Delta t_{in}) = y_i(0) e^{-r\Delta t_{in}} + \frac{q}{r}(1 - e^{-r\Delta t_{in}}) \tag{6.20}$$

$$r = D_i(0) / y_i(0) \tag{6.20a}$$

$$q = \Omega_{2_i}(0) \tag{6.20b}$$

where $y_i^p(\Delta t_{in})$ is the predicted value at the time of Δt_{in}; in $y_i(0)$, zero in the bracket means the initial value before the integration; Ω_{2_i} is the i-th entry in vector $\boldsymbol{\Omega_2}$. The corrector step is Integration B and the corrected value y_i^c is obtained as:

$$[\, y_1^c, ..., y_i^c, ..., y_{ns}^c \,]^T = \boldsymbol{\Phi}^{n+1} \tag{6.21}$$

The integration of Eq. (6.20) is supposed to be a first-order scheme in which the truncation error is $O(\Delta t_{in}{}^2)$. Assuming that an n-order solver is adopted in the macro-step, the truncation error in HMM is assumed to be $O(\Delta t_{in}{}^{n+1})$. Approximately, the relative error between the predicted and corrected value could be estimated by a single n-order term of the size step Δt_{in}:

$$\frac{y_i^c - y_i^p}{y_i^c} = a(\Delta t_{in})^n \tag{6.22}$$

The targeting value of the relative error ε is given by:

$$|\, a(\Delta t_{target})^n \,| = \varepsilon \tag{6.23}$$

Defining a parameter σ by:

$$\sigma = \max_i \left(\frac{|\, y_i^c - y_i^p \,|}{\varepsilon y_i^c} \right) \tag{6.24}$$

Hence, to limit the relative error below ε, the targeting time step could be estimated by:

$$\Delta t_{target} = \Delta t_{in} / [(\sigma)^{1/n} + 0.005] \tag{6.25}$$

We define a user defined parameter c:

$$c = f / \varepsilon \tag{6.26}$$

where f is a safety factor to guarantee the error is limited within an expected value. If the relative error estimated in Eq. (6.22) is below ε, the values from Integration B is acceptable. Otherwise, the integration will be

reinitialized with a new time step as estimated by Eq. (6.25).

It is interesting to observe that from Eq. (6.25), the time step adopted by the next step is dependent on the current time step and the relatively error between the predicted values and the correct values. A user-defined parameter *c* could be used for controlling the error and step sizes. By using this adaptive scheme, the error estimation parameter σ would converge to 1 because when σ =1, the updated step size is barely changed. Finally, it is noted that if a higher order scheme macro-solver is used in HMM (*n* is larger), the targeting time step size is larger, reflecting that a higher order scheme could alleviate the requirement for a small step size.

6.3.3 HMM in homogeneous auto-ignition

The HMM scheme (Integration B) proposed in this study was first implemented in constant-volume auto-ignition. To test HMM's accuracy and efficiency, its auto-ignition of H_2, CH_4 and C_4H_{10} with air was conducted with SENKIN [112]. The detailed hydrogen, methane and butane mechanisms adopted in this study are listed in Table 6.2.

Table 6.2 Chemical mechanisms tested in this study. PRF stands for primary reference fuel, which is a two-component blend of n-heptane and iso-octane.

Mechanism	Size	Sources
Hydrogen	10 species, 21 reactions	LLNL hydrogen [154]
Methane	53 species, 325 reactions	GRI 3.0 [155]
Butane	111 species, 784 reactions	USC-II [110]
Diesel surrogate	48 species, 157 reactions	PRF mechanism [140]

Recalling Eq. (6.1), the governing equations in this constant volume auto-ignition could be expressed as:

$$\frac{d\boldsymbol{\Phi}}{dt} = \boldsymbol{\omega}(\boldsymbol{\Phi}) + \boldsymbol{\Omega}_1 \tag{6.27}$$

$$\boldsymbol{\Phi} = [\, y_1, ..., y_i, ..., y_{n_s}, T \,]^T \tag{6.27a}$$

$$\boldsymbol{\omega} = [\, \omega_1, ..., \omega_i, ..., \omega_{n_s}, \dot{T} \,]^T \tag{6.27b}$$

Different from Eq. (6.1), because of the trivial transportation terms, the LHS of Eq. (6.27)is a normal time derivative instead of a material time derivative and $\boldsymbol{\Omega}_1 = 0$. Moreover,

$$\dot{T} = -\sum_{i=1}^{n_s} h_n \omega_n / \rho c_v \tag{6.28}$$

where h_n, ρ, c_v are the enthalpy of species n, density and heat capacity, respectively.

It is noted that both the HMM scheme and adaptive time step scheme are applied into this auto-ignition process. The user-defined parameter c was set as 500 for all cases. The relative and absolute error tolerances in HMM are 10^{-5} and 10^{-15}, respectively. As a comparison, the ODEs integrator DASAC was used, in which, the relative and absolute error tolerances are set as 10^{-5} and 10^{-20}. Due to an extremely small steps near the ignition point and an strict error control scheme used in DASAC, it is noted that we take the calculated values from DASAC as the exact ones and thus evaluate the relative errors κ for a variable Φ in the current HMM by:

$$\kappa = \frac{|\Theta - \Theta^E|}{|\Theta + \Theta^E|} \tag{6.29}$$

where Θ^E is the exact values computed from DASAC. In addition, the original DASAC in SENKIN is initialized once and hence no reinitialization is needed. However, as pointed out by Imren et al. [78] and Gou et al. [150], to be more representative of solver performance in CFD combustion, an imposed solver reinitialization after every base time step *h* was considered in the current homogenous auto-ignition. In the current study, $h = 10^{-7}$ was used unless otherwise specified.

Accuracy

Figure 6.5 shows the comparison between the HMM calculated and DASAC calculated ignition delays at 3 different equivalence ratios with different temperatures and pressures in a methane and air mixture. As seen, for all of the cases, the ignition delays predicted by the current HMM method agree very well with those calculated by DASAC. Two selected significant intermediate species OH and HO_2 as well as the temperature profile in the methane auto-ignition at initial temperature of 1200K and 1 atm with an equivalence ratio of 1, calculated with HMM and DASAC, respectively are shown in Figure 6.6. It is observed that even near the ignition point where the temperature and species change dramatically, the current HMM scheme is still able to capture the exact values, indicating that the HMM integrates the stiff

chemistry accurately.

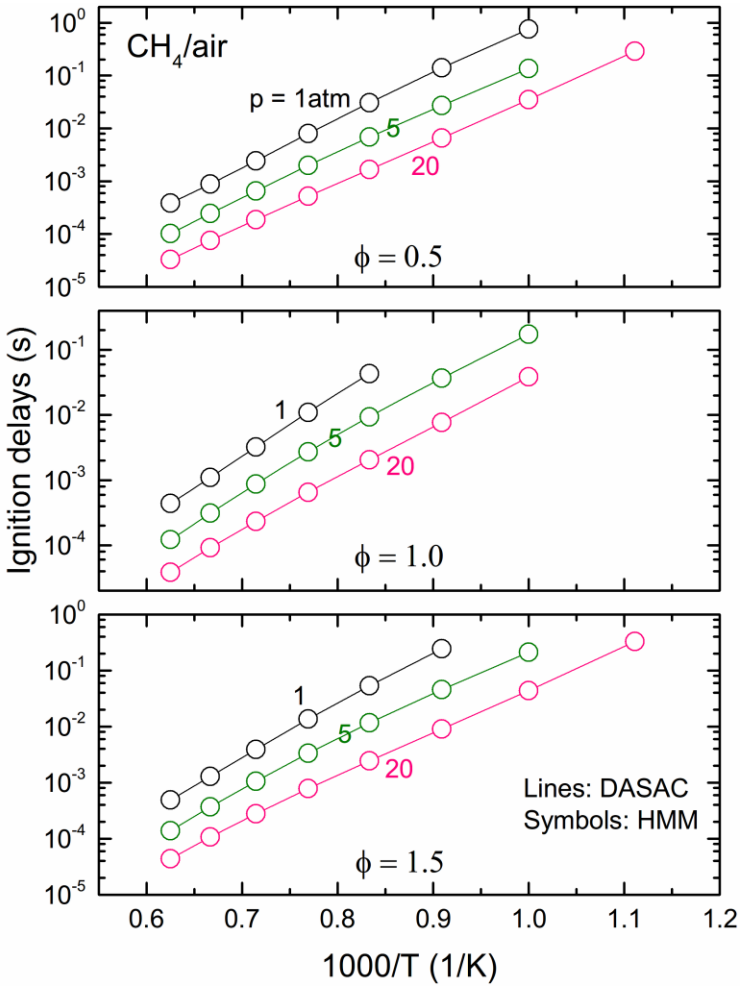

Figure 6.5 Comparison of ignition delays as a function of the initial temperature for constant-volume auto-ignition of CH_4/air under various pressures and equivalence ratios, calculated with DASAC (lines) and HMM (symbols), respectively

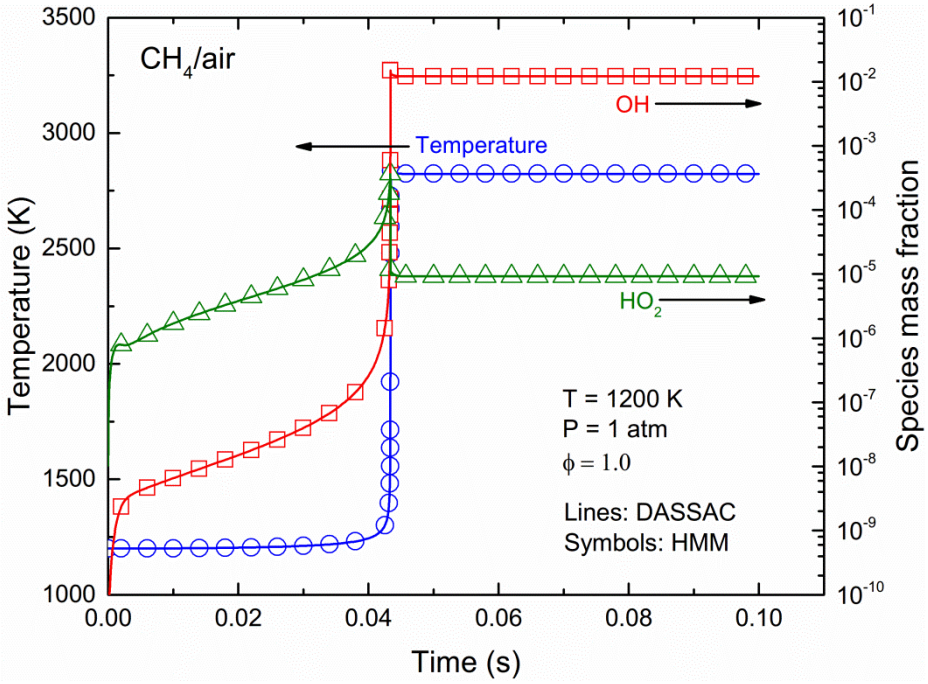

Figure 6.6 (a) Profiles of temperature (Left Y) and species mass fractions (OH and HO_2, Right Y) for constant-volume auto-ignition of CH_4/air, calculated with DASAC (lines) and the HMM method with (symbols), respectively

To analyze the accuracy of the current HMM, the relative error of temperature as well as the two selected species calculated by Eq. (6.29) is shown in Figure 6.7. It is observed that near the ignition point, the error shows a peak for all the three parameters. It is attributed to the fact that in the implicit ODEs solver DASAC adopt an extremely small step size to control the error while the current adaptive scheme in the current HMM should give consideration to the efficiency. To further prove this point, we increased the user-defined parameter *c* and calculated the relative error at the inflection point (as indicated by the black circle in Figure 6.7) for the temperature. It is observed that with a larger *c* values from 1000 to 3000, the relative error of the temperature decreased. Moreover, it is interesting to note that the change of

the error with the increasing *c* value is in a small scale, indicating that the error is not subject to the *c* value when it is larger than 500 (large enough).

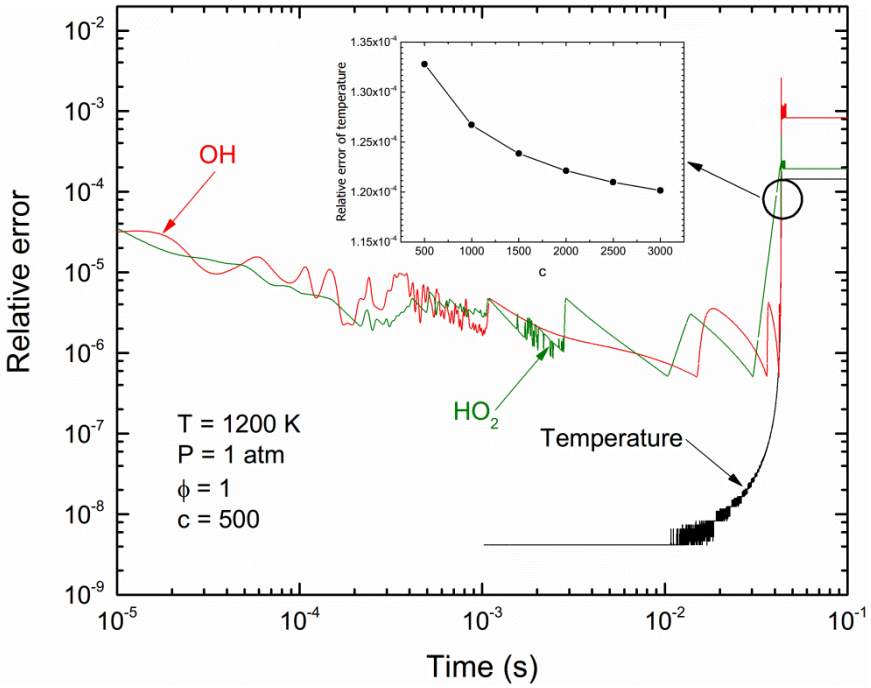

Figure 6.7 Relative errors in temperature and species mass fractions (OH and HO_2) between HMM and DASAC with c=500. Near the ignition point as indicated by the black circle, the relative errors in temperature were plotted with different *c* values

The capability of HMM for different fuels with different sizes of mechanisms was also tested. Figure 6.8 shows the ignition delays calculated with HMM and DASAC in H_2/air mixture and C_4H_{10}/air mixture, respectively. It is again shown that there is no difference between the calculated values between these two solvers.

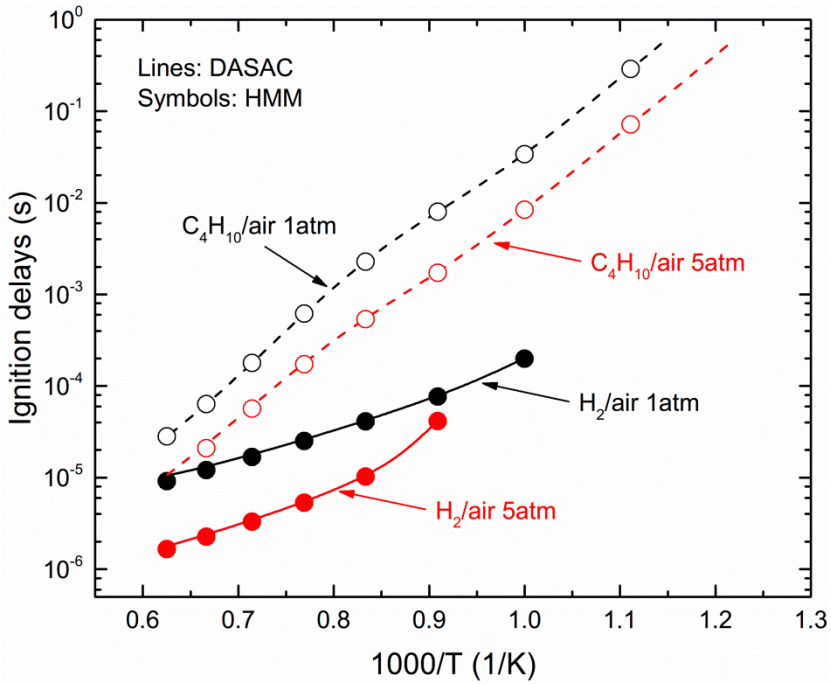

Figure 6.8 Comparison of ignition delays as a function of the initial temperature for constant-volume auto-ignition of C_4H_{10}/air and H_2/air under 1 atm and 5 atm, calculated with DASAC (lines) and HMM (symbols), respectively

Efficiency

Normally, because a first order explicit solver is used and typically less than 10 steps are needed to be converged to stationary values for each group in Eq. (6.14), the computational cost in the micro-solver is inexpensive. However, if the estimated inner time step is extremely small such as at the thermal runaway stage in some high temperature and high pressure conditions, the 2nd order implicit solver in Implementation B might cause nontrivial cost, which will be seen later in the multidimensional CFD engine-condition simulations. In the current homogenous constant volume ignition delay calculations with relatively low pressure and temperature, a dramatically CPU wall-clock time reduction can be achieved as shown in Figure 6.9(a). It is interesting to note that

with the increase of the initial temperature, the CPU time presents a decreasing trend in the HMM scheme. This is because the total time of calculation for all cases were set as 1s while for the high temperature cases which have short ignition delays, most of the calculation is under equilibrium conditions where the global time step is directly adopted as the inner time step. In terms of mechanism sizes, the computational time was also compared to show the current scheme's applicability in mechanisms with different sizes. As shown in Figure 6.9(b), the CPU time speed-up factor (the computational CPU time of DASAC divided by that of HMM) shows an increasing trend with larger sizes. Theoretically, if both the micro-solver and macro-solver are explicit solvers, the relation between computational CPU time in HMM and mechanism should be linear [80]. However, as we can observe here, because of a 2^{nd} order implicit solver used in the macro-solver in this study, the correlation is nonlinear. Hence, the performance of the current HMM is subject to the solvers used by the users. In the current formulation of HMM, we can observe that a larger reduction factor could be achieved in larger size mechanism integrations (e.g., for C_4H_{10}, the CPU time speed up by more than 700 times with this HMM scheme than the conventional DASAC solver with imposed reinitialization).

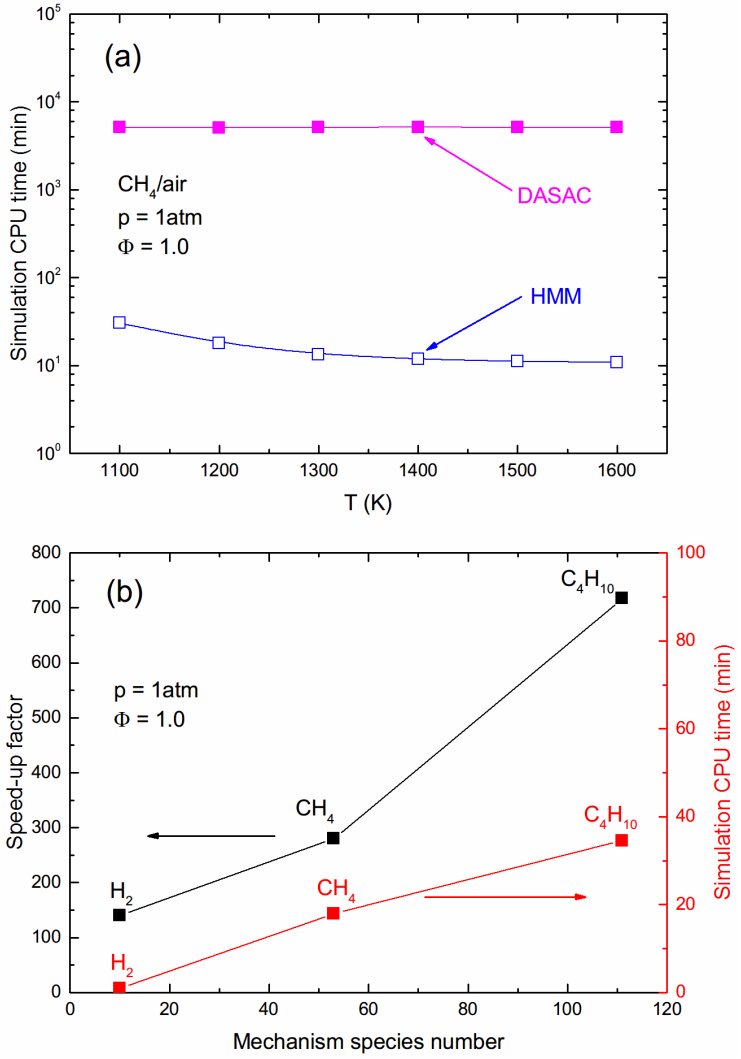

Figure 6.9 (a) Simulation CPU time for the integration of constant-volume auto-ignition for stoichiometric methane/air mixture at atmospheric pressure, calculated with DASAC (closed symbols) and HMM (open symbols), respectively. (b) Left Y: CPU time speed-up factor as a function of the mechanism species number; Right Y: Simulation CPU time with HMM as a function of the species number

Stability

The stability of the current HMM scheme should be discussed both in the micro and macro solvers. First of all, in the micro-solver, the time step as in Eq. (6.14a) is smaller than the minimum time scale in that species group. Hence, even though an explicit solver adopted, it is numerically stable to integrate the

stiff species in the micro solver. In the macro solver, as indicated in Eq. (6.18), only the slow species whose time scale is larger than the inner time step are integrated, thus the stability is guaranteed. In summary, the current HMM scheme estimates the timescale of each species before every inner time step and integrate them with time steps that are smaller than the minimum time scale in the species groups, thus no matter implicitly or explicitly in the micro and macro solvers, it is numerically stable.

6.3.4 HMM in multidimensional reactive flow simulations

CFD numerical framework

The current HMM is then implemented in a multidimensional engine simulation to test its fidelity in numerical chemistry integration with transportation terms and other complex physical phenomena. The numerical CFD framework used in this study is the KIVA-4 codes. Based on the previous version KIVA-3V which uses a finite volume method for arbitrary hexahedrons, KIVA-4 is capable of treating with unconstructed meshes. The spatial discretization in KIVA family codes is based on the method of arbitrary Lagrangian Eulerian (ALE). The transport terms are discretized by a quasi-second-order up-winding scheme and a second-order central scheme respectively for the convention term and the diffusion term. The temporal integration is based on a first-order time-splitting scheme. Three phases are adopted sequentially to advance source, diffusion, and convection terms by

splitting each time step. The combustion chemistry is originally in KIVA-4 calculated by a global one step reaction. In this study, we coupled CHEMKIN-II into KIVA-4 for chemistry kinetics treatment and computation. The turbulence model and spray break-up model in the current KIVA-4 code are the modified RNG $k-\varepsilon$ model [38] and KH-RT break-up model [41], respectively. It should be pointed out that even though all these models in KIVA-4 are formulated in the context of RANS, the current HMM scheme for the chemical source term integration is independent on the RANS related scales and thus is also applicable in LES and DNS.

Figure 6.10 summarizes the schematic flow chart of the integrated KIVA-4-CHEMKIN codes. As shown, the key variables exchanging between KIVA-4 and CHEMKIN are temperature, pressure and species concentrations. With the provided temperature, pressure and species concentrations, a matrix of ODEs is constructed. The solutions of the ODEs are the updated species concentrations, which will be reverted back to KIVA-4. In the original KIVA-4 CHEMKIN version coupled by NUS [156], VODE was adopted to integrate the stiff chemical ODEs. The HMM scheme proposed in this study is coupled into the current KIVA-4-CHEMKIN codes by replacing the original ODE integrator (as shown in Figure 6.10) VODE [94] by the current HMM scheme. All the other models were kept the same.

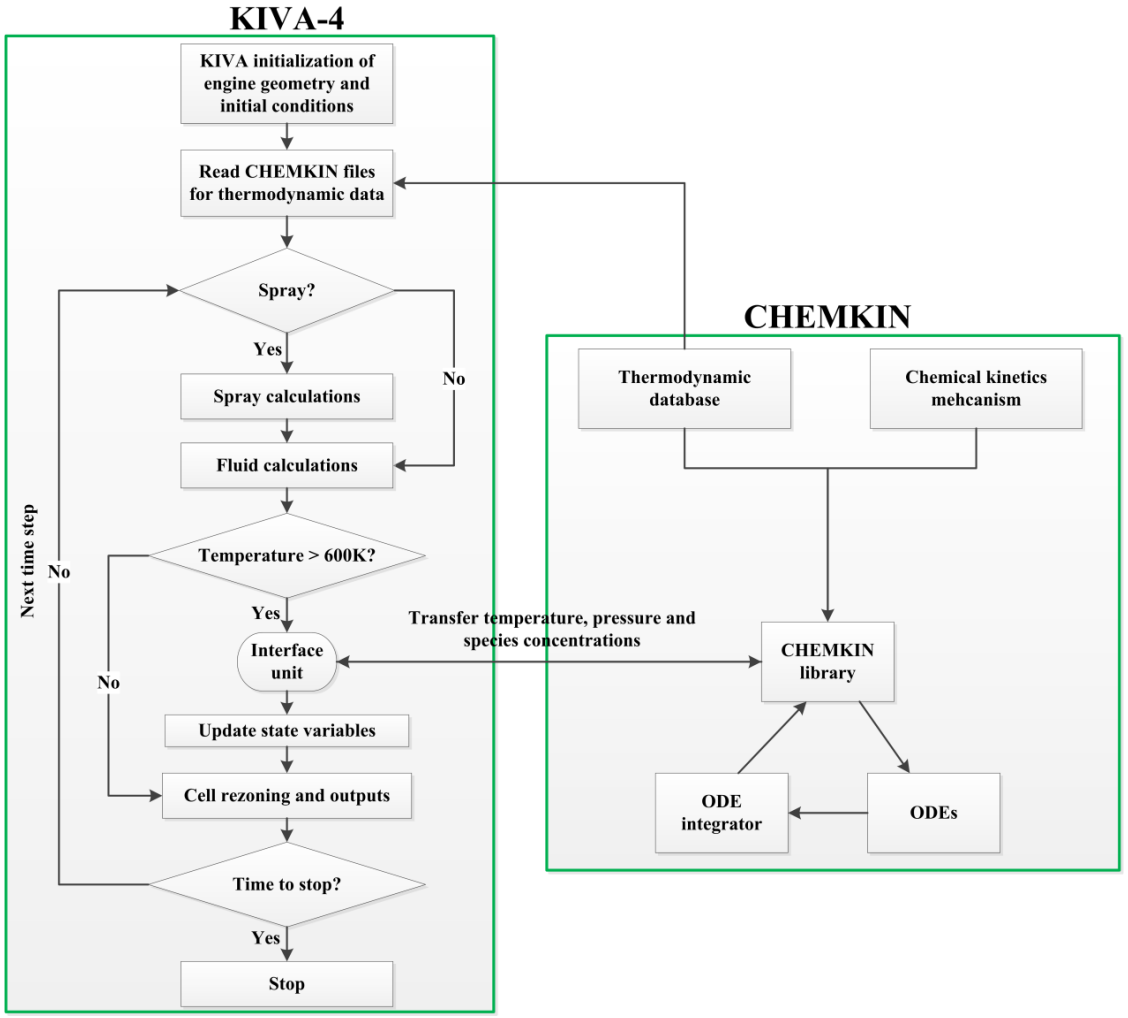

Figure 6.10 Schematic flow chart of the integrated KIVA-4 and CHEMKIN codes

A hybrid scheme

As discussed above, the current HMM with low order of accuracy solvers could be slow in high temperature and high pressure condition due to the extremely small time steps adopted to ensure the accuracy. However, in engine simulations, after the thermal runaway, the temperature and pressure are relatively high in the combustion chamber. Thus, the computational reduction performance of HMM in non-homogeneous charged engine simulations, as can be seen later, is not very satisfactory. Considering the higher order accurate scheme used in VODE (maximum 12), in the cases where extremely small time steps are needed to ensure accuracies, VODE could even outperform HMM. Hence, taking advantage of the reactivity stratification and the "reaction rate" stratification caused by the non-homogeneity in the engine, a hybrid scheme is proposed. In this hybrid scheme, due to the fact that the cells with slow reaction rate could adopt relatively large time step to resolve the system accurately, we define a "reaction rate" parameter in each cell at each time step by a Euclidean norm to wisely assign the cells into proper solvers (HMM or VODE):

$$R_{i4} = 1/||\omega_i \cdot mw_i / \rho|| \tag{6.30}$$

where R_{i4} represents the reaction rate parameter of a computational cell, the subscript *i4* is the cell index in KIVA. R_{i4} in different computational cells is then sorted in an ascending order. Then the speed performance of VODE and HMM is estimated by the number of cells computed within unit time:

$$Sp_{HMM} = N_{HMM} / C_{HMM} \tag{6.31}$$

$$Sp_{VODE} = N_{VODE} / C_{VODE} \tag{6.32}$$

where Sp is the speed of different solvers, N is the number of computational cells computed within one global time step, C is the computational cost to integrate the chemistry of N number of cells.

Before the thermal runaway in the engine, only one cell is computed by VODE and all the other cells are considered by the current HMM. After the combustion occurrence, if the speed of VODE exceeds HMM, N_{HMM} cells with the lowest values of R_{i4} (according to their sorted R_{i4} order evaluated in Eq. (6.30)) will be considered in VODE in the next time step, where N_{HMM} is given by:

$$N_{HMM} = N_{tot} \cdot \frac{\xi \cdot Sp_{VODE}}{(Sp_{HMM} + \xi \cdot Sp_{VODE})} \tag{6.33}$$

where ξ is a parameter to purposefully control the number of cells assigned into VODE. In this study, based on the numerical observation, $\xi = 2$ is adopted to assign cells into VODE during the combustion process. At each time step, Eq. (6.30)-(6.32) will be updated and Sp_{HMM} and Sp_{VODE} will be evaluated at the end of a global time step and used for the next time step in Eq. (6.33).

In this way, one could expect that the cells that could be integrated with large time steps are computed by HMM. In these cells, the calculation in HMM would be much faster than that in VODE. On the other hand, the cells with large

R_{i4} values computed in VODE will show better efficiency than that by HMM. Thus, an optimum performance could be achieved. The accuracy and efficiency of HMM, VODE and the current hybrid scheme in multidimensional CFD engine simulations will be presented and discussed in the next section.

HMM implementation in non-homogeneous engine simulations

The tested engine operating conditions and specifications are listed in Table 6.3. A computational sector mesh with 8580 hexahedron cells was created as shown in Figure 6.11.

Table 6.3 The testing engine specifications and operating conditions

Engine	GW4D20 diesel engine
Fuel	diesel
Bore, stroke (mm)	93.1, 92
Nozzle number	5
Compression ratio	16.7:1
Engine speed (rpm)	1600
Injection manner	direct injection
SOI (deg. ATDC)	-40
Intake tem. (K)	370
IVC (deg. ATDC)	-130
EVO (deg. ATDC)	55

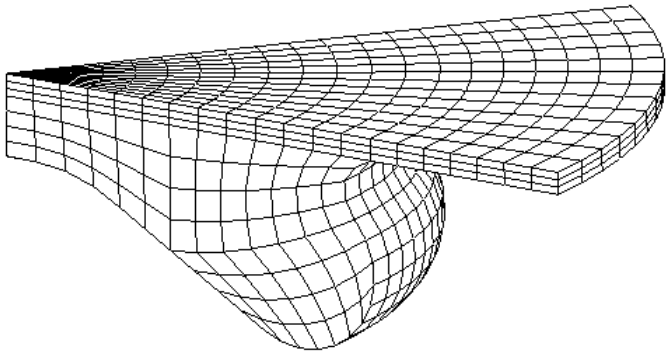

Figure 6.11 Computational meshes with 8580 hexahedron cells at top dead center

As compared in Figure 6.12, the pressure traces predicted by HMM, VODE and the hybrid scheme are nearly identical. As a function of the crank angle, their computational cost in each global time step is compared in Figure 6.13(a). It is observed that the computational cost in each global time step of HMM after the combustion occurrence process is much larger than that of the VODE. As explained above, this is caused by the extremely small time steps because of the low order of accuracy solvers in the current HMM. However, in Figure 6.13(b), the total simulation time from the intake valve closure (IVC) to exhaust valve open (EVO) by HMM is still smaller than that of the VODE, due to the better performance of HMM during the pre-combustion and post-combustion process. With respect to the hybrid scheme, it is seen that before the cells assignment as in Eq. (6.33) and when only one cell computed in VODE, the performance of the hybrid scheme is almost the same as in HMM. However, after the thermal runaway where the speed of VODE outperforms HMM, Eq. (6.33) assign the stiffest cells to VODE based on their speed benefit.

In the post-combustion process where most of the cells tend to be in equilibrium, HMM stands out again because even the global time step could be adopted as the inner time step under this condition.

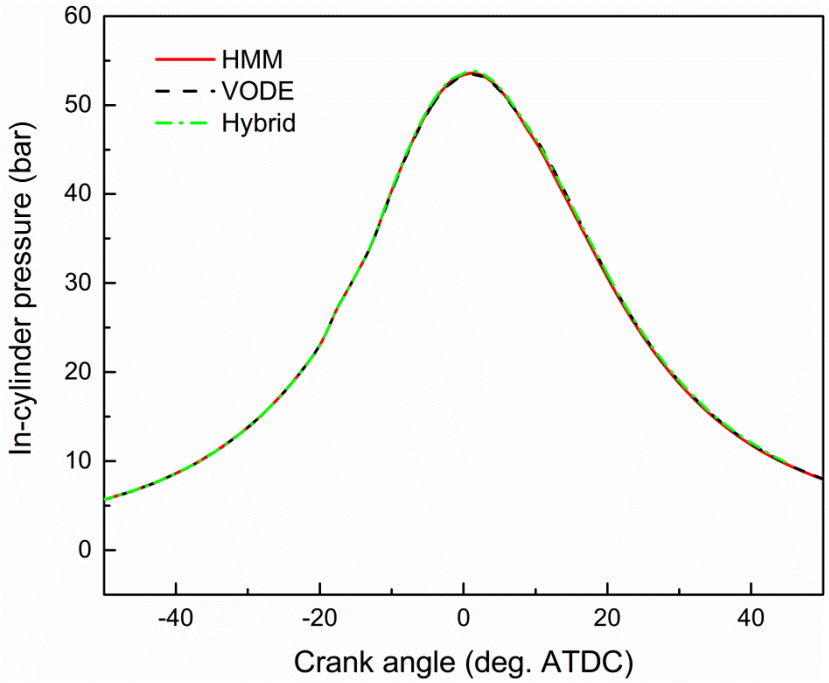

Figure 6.12 Comparison of in-cylinder pressure as a function of crank angle, calculated with HMM, VODE and the hybrid scheme, respectively

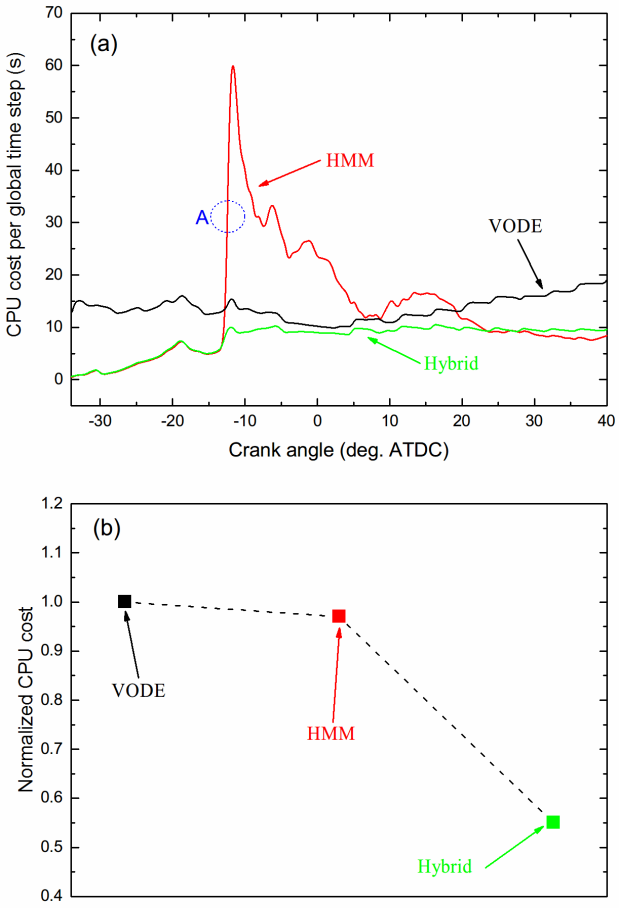

Figure 6.13 Computational cost of (a) chemistry integration in each global time step as a function of crank angle, (b) engine simulation from IVC to EVO, calculated with VODE, HMM and hybrid scheme. The computational cost in (b) is normalized by the VODE cost. Point A in (a) implies the maximum HMM cost rise rate point

Figure 6.14 plots the workload of VODE and HMM in the hybrid scheme and the speed of each solver as a function of the crank angle during the simulation process. It is shown that at Point A where the performance of HMM lag behind VODE, the number of cells in VODE dramatically increase. During the combustion process, the number of cells in VODE is more than that in HMM because of their speed performance and cell allocation as in Eq. (6.33). The better speed performance of HMM even in the combustion process indicates that the assignment of the cells with small R_{i4} values into HMM is

proper. In addition, Figure 6.15 shows that at the crank angle of Point A (shown in Figure 6.13), the low R_{i4} regions in Figure 6.15(a) basically corresponds to the region with high temperatures in Figure 6.15(b), indicating that at the initial stage of the combustion process, temperature is the dominant factor to control the reaction rate in the cells. The dash lines in Figure 6.15, where inside of the dash lines is the VODE computing region and outside of the dash lines is the HMM computing region, separate the HMM computing region from the VODE computing region . It is seen that the low R_{i4} as well as the high temperature regions roughly fall into the VODE region, proving the fidelity of Eq. (6.33). Therefore, with this hybrid scheme, we could take advantage of HMM and VODE under different conditions in multidimensional CFD simulations to achieve optimum efficiency.

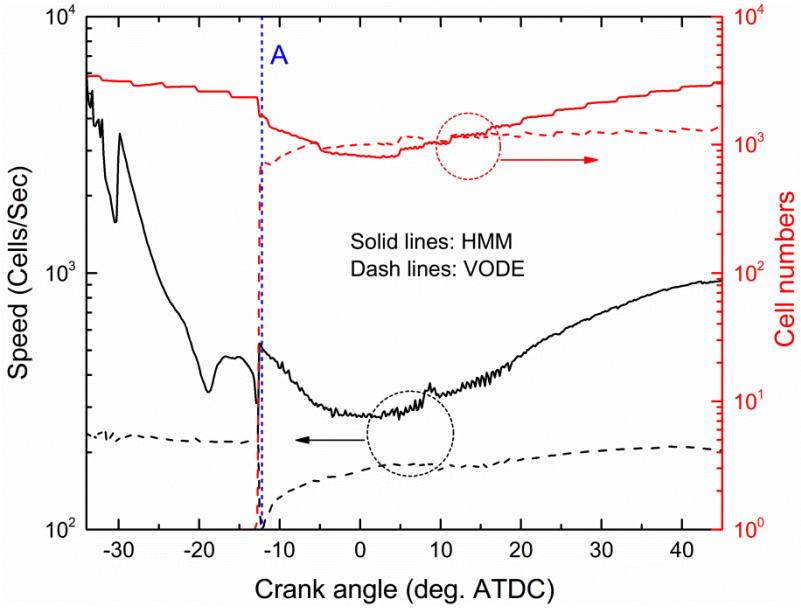

Figure 6.14 Speed (the number of computational cells calculated within a unit time) and the computing cell numbers in HMM and VODE, respectively, during the computing process with the hybrid scheme. The blue short dash line A corresponds to Point A in Figure 6.13

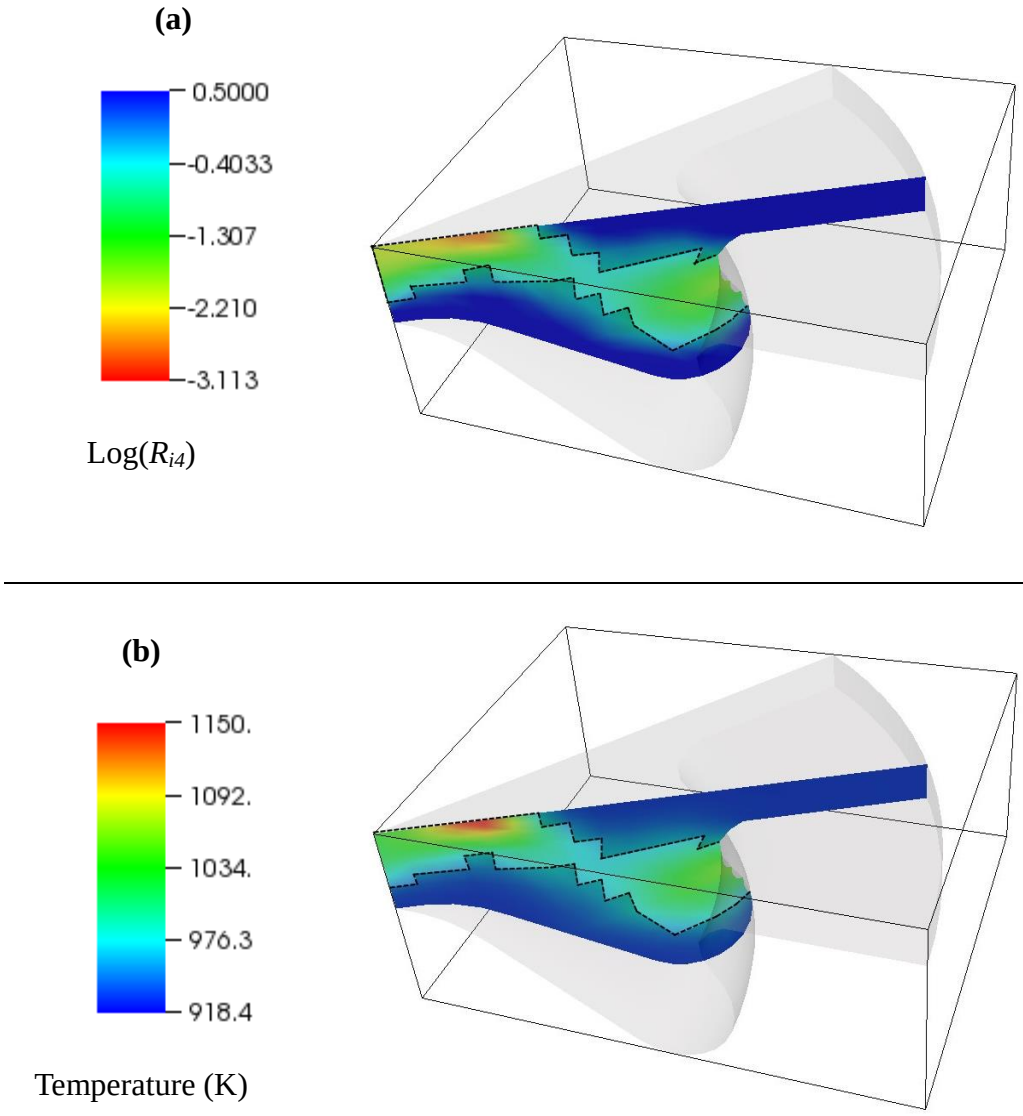

Figure 6.15 The Spatial contours in the combustion chambers of (a) R_{i4} and (b) temperature at the crank angle of Point A in Figure 6.13, illustrated with a slice in the middle. The region inside of the black dash line on the slice indicates the region computed by VODE while the region outside of the black dash line indicates the region computed by HMM

6.4 Summary

In summary, to accelerate the RCCI combustion simulation process, a parallel computing algorithm for chemical solver is firstly proposed and implemented. It is shown that dramatically-reduced computational time can be achieved.

The concept of heterogeneous multiscale method has been also applied into stiff chemistry integration. This HMM has tremendous flexibility since different discretization schemes could be applied in the macro and micro solvers. In this study, a first order explicit Euler scheme for the micro solver and a second order implicit trapezoidal rule for the macro solver were used for testing. The formulation of HMM was implemented into auto-ignition and multidimensional engine simulations. It is proved that this method could efficiently and accurately integrate the combustion chemistry in reactive flows.

It is also seen that the limitation of the current formulation of HMM is the low order solver necessitate small time steps under high temperature and high pressure conditions, which dramatically deteriorate the efficiency, as shown in the multidimensional engine simulations. Hence, a hybrid scheme with HMM and VODE to avoid computational cells with large reaction rate to be dealt with by the current HMM formulation was proposed.

The significance of this method is its huge flexibility of micro and macro schemes and its outstanding efficiency. The application of other discretization schemes in the macro and micro solvers and their performance in terms of efficiency and accuracy are recommended for future work.

Chapter 7 Conclusions and Recommendations

7.1 Conclusions

Numerical models and schemes are developed in this dissertation to more efficiently and accurately model the RCCI combustion process. A compact and accurate surrogate chemical reaction mechanism for diesel and gasoline, is firstly developed, validated and then incorporated into multidimensional CFD for RCCI dual fuel combustion simulations. In addition to the chemical mechanism, comprehensive and unified combustion models to investigate the complex combustion process in RCCI engines, including an innovative hybrid model with a characteristics timescale combustion model and a well-premixed reactor model to simulate the diffusion flame and auto-ignition, a novel Lagragian marker model to simulate the flame propagation, were proposed. Furthermore, numerical strategies including a MPI configuration of parallelizing chemical solvers, a heterogeneous multiscale method for stiff combustion chemistry integration, are proposed in this thesis to accelerate the RCCI combustion computing process more than 10 times than the conventional solvers in multi-dimensional engine simulations. The major findings in this dissertation are summarized in the following sections.

7.1.1 PRF mechanisms

The primary objective of this dissertation is to numerically investigate the

combustion process in RCCI engines. Hence, with different purposes, three different gasoline and diesel surrogate mechanisms were developed, including two PRF mechanisms with different sizes (M1: 51 species and 225 reactions, M2: 43 species and 144 reactions), one PRF mechanism coupled with PAH for soot prediction (72 species and 225 reactions). When developing these two PRF mechanisms with different sizes, the role of fuel cracking process to low carbon radicals was discussed. It is found that even simplifying the fuel cracking to C1 as in the M2 development, the basic combustion characteristics such as ignition delay and laminar flame speed can still be well captured. Compared with the previous PRF mechanisms in the literatures, M2 is more compact yet able to accurately predict the combustion characteristics. With respect to M1, the fuel cracking process was simplified to C2. It is observed that it gave more accurate laminar flame speed and intermediate species profile prediction that that of M2. M3 consists of a PAH submodel and M2. It is validated in constant volume combustion and also proved to be robust for combustion characteristics and soot emission prediction in RCCI, HCCI and PCCI engines fueled with PRF fuels or gasoline/diesel.

7.1.2 Auto-ignition and diffusion flame modeling

Considering the special way of combustion in RCCI engines, auto-ignition and diffusion flame need to be resolved. Unlike the common way in the literatures which adopted the well-premixed reactor assumption with

CHEMKIN solver to simulate the auto-ignition and diffusion flame, this dissertation proposed an innovative hybrid model with a characteristics timescale model to resolve the mixing controlled diffusion flame and the well-premixed reactor model with CHEMKIN to deal with the auto-ignition. In this way, the mixing controlled diffusion flame where the interaction between the turbulence and chemical timescales is significant is treated by the CTC model, the auto-ignition where the chemistry kinetics dominates is resolved by the well-premixed reactor model. By validating it in a RCCI engine with different injection timings and strategies, this hybrid model is proved to be able to improve the combustion prediction especially in the scenarios where mixing controlled diffusion flame is dominant. It is also noted that unlike the classical original CTC model which used generic chemical mechanism, this model incorporates a CEQ equilibrium solver and is able to calculate detailed chemistry. More importantly, it is shown that this hybrid is able to save more than half computational cost compared with the pure well-premixed reactor model in some cases due to less stiff ODEs solved in CHEMKIN. Therefore, this hybrid model is very promising to simulate the combustion process in RCCI engines accurately and efficiently. This newly developed model can also be used for accurate conventional diesel engine or PCCI engine combustion simulations because it covers the auto-ignition and diffusion flame combustion regimes.

7.1.3 Flame propagation modeling

Due to the special fuel intake manner (port fuel injection with low reactivity fuel and direct injection with high reactivity fuel), there could be one case scenario where the small-mass direct injected fuel acts as a spark plug in SI engine and thus causes flame propagation in the low reactivity fuel and air mixture. This situation has been observed both experimentally and numerically in RCCI combustion in the literatures. It is also reported that the omittance of flame propagation modeling in these cases would lead to erroneous predictions in RCCI combustion. To solve this problem, a novel flame propagation model is proposed in this work and incorporated into 3D CFD engine simulations. Based on a previous Lagragian markers model used in spark ignition flame propagation model, this flame propagation model applies discrete imaginary particles to represent the flame front resolution in the computational domain. The heat release of the flame front calculation is formulated to couple in detailed chemistry. Coupling with CHEMKIN for auto-ignition and diffusion flame calculation, it is proved that this model improves the prediction than that without consideration of flame propagation especially in the cases of flame-propagation-dominant RCCI combustion.

7.1.4 Computation acceleration of RCCI modeling

Besides the combustion chemical mechanisms and combustion models, another critical issue when simulating multidimensional is the expensive

computational cost. The last part of this dissertation is devoted to developing advanced schemes and algorithms to accelerate the computation of RCCI combustion. Of course, these schemes and algorithms are universal in other multidimensional reactive flow simulations.

First of all, due to the dominant cost of the chemical solver, a parallel algorithm to compute the chemistry integration process in the multidimensional computational domain in parallel is proposed based on a round-robin algorithm. It is shown that compared with the serial computation, a 16 cores CPU parallel computing by using this algorithm can save the computational cost by 80%. This simple but effective algorithm is able to alleviate the prohibitive computational cost caused by the chemistry integration in multidimensional CFD simulations with a large amount of cells.

Furthermore, a heterogeneous multiscale method is proposed and implemented in homogeneous 0-D auto-ignition and 3-D engine simulations. Good accuracy and efficiency have been achieved. In addition to this HMM scheme, a hybrid scheme with HMM and VODE is proposed and implemented in 3-D engine simulations to further optimize the computational efficiency. It is observed that a maximum of half computational time can be saved.

In sum, these algorithms and schemes can be applied not only in RCCI combustion simulations, but also in other engine simulation with stiff chemistry integration. Moreover, these algorithms and schemes are universally

helpful to accelerate the reactive flow simulations.

7.2 Recommendations for future work

7.2.1 Chemical mechanisms

Although the current PRF mechanisms are robust and efficient to simulate the RCCI combustion process fueled with gasoline and diesel, other fuel applications in RCCI simulations are desirable. Alcoholic fuels and biodiesel application in RCCI engines are an important research trend in the near future. Hence, it is recommended to develop a chemical surrogate mechanism platform which includes not only gasoline and diesel, but also most of the biofuels. With this platform, we can easily apply this chemical mechanism platform to conduct RCCI dual fuel simulations.

7.2.2 Combustion models in RCCI combustion

It is seen that the hybrid CTC and well-premixed reactor model predict the combustion characteristics very well. However, its prediction on the soot and NO_x emission has not been discussed in this model. Moreover, although this work has incorporated NO_x and soot emission in the flame propagation model, it is observed that the NO_x and soot emission have not been very accurately predicted by the current models. This might be due to the over-prediction of the local temperature in the flame propagation model. Hence, even though emission formation is not the focus of this dissertation, it is desirable to develop accurate emission formation models to predict the NO_x

and soot emissions in the auto-ignition, diffusion flame and flame propagations in RCCI engines in the future. In addition, more efforts should be dedicated to a thorough discussion on the flame propagation model and its sensitivity analysis of mesh cell numbers, critical temperature and initial discrete particle numbers.

7.2.3 Comprehensive acceleration methods

Although good acceleration and huge computational overhead saving have been accomplished for multidimensional engine simulations in this dissertation, it expects more computational time saving by improving the independent algorithms developed in this dissertation (parallel chemical solver computing and HMM).

CPU parallel architecture is limited to tens of cores even in a large university like Nation University of Singapore. Hence, modern GPU application should be a promising solution due to its highly parallel programmable processor with higher peak arithmetic and memory bandwidth than CPU. Hence, the chemical solver parallel algorithm could be implemented based on GPU clusters by reprograming it to fit in GPU.

The HMM developed in this dissertation is found to be very efficient. However, as pointed out in Section 6.3.4, the limitation of the current HMM formulation is the low order of accuracy solvers used in the macro and micro solvers, which leads to small time steps and huge computational cost under

high reaction rate situations. Therefore, the performance of the current HMM concept with solvers of different order of accuracy in the macro and micro solvers should be further discussed in the future.

Besides the improvement of the current schemes in this dissertation, simple combination of them due to their independence might achieve more computational efficiency. In addition, it is also recommended to implement other independent advanced high performance computing algorithms such as dynamic adaptive chemistry (DAC) in multidimensional reactive flow simulations, together with the methods developed in this dissertation to further accelerate engine simulations.

Bibliography

[1] Heywood JB, Internal combustion engine fundamentals, Mcgraw-hill New York, 1988.

[2] Lu X, Han D, Huang Z. Fuel design and management for the control of advanced compression-ignition combustion modes. Prog. Energ. Combust. 2011;37:741-83.

[3] Charalambides AG, Homogenous charge compression ignition (HCCI) engines, INTECH Open Access Publisher, 2013.

[4] Dec JE, Hwang W, Sjöberg M, An investigation of thermal stratification in HCCI engines using chemiluminescence imaging, SAE 2006-01-1518.

[5] Manente V, Johansson B, Cannella W. Gasoline partially premixed combustion, the future of internal combustion engines? International Journal of Engine Research 2011;12:194-208.

[6] Manente V, Tunestal P, Johansson B, Cannella WJ, Effects of ethanol and different type of gasoline fuels on partially premixed combustion from low to high load, SAE 2010-01-0871.

[7] Manente V, Zander C-G, Johansson B, Tunestal P, Cannella W, An advanced internal combustion engine concept for low emissions and high efficiency from idle to max load using gasoline partially premixed combustion, SAE 2010-01-2198.

[8] Yang Y, Dec JE, Dronniou N, Sjöberg M. Tailoring HCCI heat-release rates with partial fuel stratification: Comparison of two-stage and single-stage-ignition fuels. Proc. Combust. Inst. 2011;33:3047-55.

[9] Kokjohn S, Reitz R, Characterization of Dual-Fuel PCCI Combustion in a Light-Duty Engine, in: Proceedings of the International Multi-Dimensional Engine Modeling User's Group Meeting, 2010.

[10] Kokjohn SL, Hanson RM, Splitter DA, Reitz RD, Experiments and modeling of dual-fuel HCCI and PCCI combustion using in-cylinder fuel blending, SAE 2009-01-2647.

[11] Splitter D, Kokjohn S, Rein K, Hanson R, Sanders S, Reitz RD, An optical investigation of ignition processes in fuel reactivity controlled PCCI combustion, SAE 2010-01-0345.

[12] Eichmeier JU, Reitz RD, Rutland C. A Zero-Dimensional Phenomenological Model for RCCI Combustion Using Reaction Kinetics. SAE Int J Engine 2014;7:106-19.

[13] Li J, Yang W, Zhou D. Review on the management of RCCI engines. Renew Sust Energ Rev 2017;69:65-79.

[14] Reitz RD, Duraisamy G. Review of high efficiency and clean reactivity controlled compression ignition (RCCI) combustion in internal combustion engines. Prog. Energ. Combust. 2015;46:12-71.

[15] Turns S. An Introduction to Combustion: Concepts and Applications. 1996.

Oxygen-Enhanced Combustion 543.

[16] Lu T, Law CK. Toward accommodating realistic fuel chemistry in large-scale computations. Prog. Energ. Combust. 2009;35:192-215.

[17] Bockhorn H, Habisreuther P, Hettel M, Numerical modelling of technical combustion, in: 100 Volumes of 'Notes on Numerical Fluid Mechanics', Springer, 2009, pp. 325-40.

[18] Zeleznik FJ, McBride BJ. Modeling the internal combustion engine. 1985.

[19] Kong S-C, Han Z, Reitz RD, The development and application of a diesel ignition and combustion model for multidimensional engine simulation, SAE 950278.

[20] Kong S-C, Reitz RD. Application of detailed chemistry and CFD for predicting direct injection HCCI engine combustion and emissions. Proc. Combust. Inst. 2002;29:663-9.

[21] Long L, Reitz R, lyer C, Jianwen Y, Modeling knock in spark-ignition engines using a G-equation combustion model incorporating detailed chemical kinetics, SAE 2007-01-0165.

[22] Stiesch G, Merker GP, A Simplified Model for Description of Triple Flames in Stratified Charge Gasoline Engines, in: Proc 12th Int Multidim Engine Modeling Users Group Meeting, Detroit, MI, 2002.

[23] Singh S, Liang L, Kong S-C, Reitz RD. Development of a flame propagation model for dual-fuel partially premixed compression ignition engines. Int J Engine Res 2006;7:65-75.

[24] Singh S, Reitz RD, Wickman D, Stanton D, Tan Z, Development of a hybrid, auto-ignition/flame-propagation model and validation against engine experiments and flame liftoff, SAE 2007-01-0171.

[25] Bhagatwala A, Chen JH, Lu T. Direct numerical simulations of HCCI/SACI with ethanol. Combust. Flame 2014;161:1826-41.

[26] Chen JH, Hawkes ER, Sankaran R, Mason SD, Im HG. Direct numerical simulation of ignition front propagation in a constant volume with temperature inhomogeneities: I. Fundamental analysis and diagnostics. Combust. Flame 2006;145:128-44.

[27] Hawkes ER, Sankaran R, Pébay PP, Chen JH. Direct numerical simulation of ignition front propagation in a constant volume with temperature inhomogeneities: II. Parametric study. Combust. Flame 2006;145:145-59.

[28] Lu TF, Yoo CS, Chen JH, Law CK. Three-dimensional direct numerical simulation of a turbulent lifted hydrogen jet flame in heated coflow: a chemical explosive mode analysis. J Fluid Mech 2010;652:45-64.

[29] Van Kalmthout E, Veynante D, Candel S, Direct numerical simulation analysis of flame surface density equation in non-premixed turbulent combustion, in: Symposium (International) on Combustion, Elsevier, 1996, pp. 35-42.

[30] Yoo CS, Lu T, Chen JH, Law CK. Direct numerical simulations of ignition of a lean n-heptane/air mixture with temperature inhomogeneities at constant volume: Parametric study. Combust. Flame 2011;158:1727-41.

[31] Yoo CS, Sankaran R, Chen JH. Three-dimensional direct numerical simulation of a turbulent lifted hydrogen jet flame in heated coflow: flame stabilization and structure. J Fluid Mech 2009;640:453.

[32] Hu B, Rutland CJ, Flamelet modeling with LES for diesel engine simulations,

[33] Li Y, Kong S-C. Diesel combustion modelling using LES turbulence model with detailed chemistry. Combust Theor Model 2008;12:205-19.

[34] Nishad K, Pischke P, Goryntsev D, Sadiki A, Kneer R, LES based modeling and simulation of spray dynamics including Gasoline Direct Injection (GDI) processes using KIVA-4 code, SAE 2012-01-1257.

[35] http://www.bakker.org/dartmouth06/engs150/10-rans.pdf. Applied Computational Fluid Dynamics.

[36] Torres DJ, Trujillo MF. KIVA-4: An unstructured ALE code for compressible gas flow with sprays. J Comput Phys 2006;219:943-75.

[37] Hirt C, Amsden AA, Cook J. An arbitrary Lagrangian-Eulerian computing method for all flow speeds. J Comput Phys 1974;14:227-53.

[38] Han Z, Reitz RD. Turbulence modeling of internal combustion engines using RNG κ-ε models. Combust. Sci. Technol. 1995;106:267-95.

[39] Amsden AA, O'rourke P, Butler T, KIVA-II: A computer program for chemically reactive flows with sprays, Los Alamos National Lab., NM (USA), 1989.

[40] Faeth GM. Mixing, transport and combustion in sprays. Prog Energ Combust 1987;13:293-345.

[41] Beale JC, Reitz RD. Modeling spray atomization with the Kelvin-Helmholtz/Rayleigh-Taylor hybrid model. Atomization Spray 1999;9.

[42] Yoshida K, Shoji H, Tanaka H, Study on combustion and exhaust gas emission characteristics of lean gasoline-air mixture ignited by diesel fuel direct injection, SAE 982482.

[43] Chen C, Bardsley ME, Johns RJ, Two-zone flamelet combustion model, SAE 2000-01-2810.

[44] Peters N, Laminar flamelet concepts in turbulent combustion, in: Symposium (International) on Combustion, Elsevier, 1988, pp. 1231-50.

[45] Pitsch H, Wan Y, Peters N, Numerical investigation of soot formation and oxidation under diesel engine conditions, SAE 952357.

[46] Hasse C, Bikas G, Peters N, Modeling DI-diesel combustion using the eulerian particle flamelet model (EPFM), SAE 2000-01-2934.

[47] Pitsch H, Chen M, Peters N, Unsteady flamelet modeling of turbulent hydrogen-air diffusion flames, in: Symposium (international) on combustion, Elsevier, 1998, pp. 1057-64.

[48] Klimenko AY. Multicomponent diffusion of various admixtures in turbulent flow. Fluid Dynamics 1990;25:327-34.

[49] Marble F, Broadwell J. The coherent flame model of non-premixed turbulent combustion. Project Squid TRW-9-PU, Project Squid Headquarters, Chaffee

Hall, Purdue University 1977.

[50] Tap F, Hilbert R, Thevenin D, Veynante D. A generalized flame surface density modelling approach for the auto-ignition of a turbulent non-premixed system. Combust Theor Model 2004;8:165-93.

[51] Colin O, Benkenida A. The 3-zones extended coherent flame model (ECFM3Z) for computing premixed/diffusion combustion. Oil & Gas Science and Technology 2004;59:593-609.

[52] Fan L, Li G, Han Z, Reitz RD, Modeling fuel preparation and stratified combustion in a gasoline direct injection engine, SAE 1999-01-0175.

[53] Liang L, Reitz RD, Spark ignition engine combustion modeling using a level set method with detailed chemistry, SAE 2006-01-0243.

[54] Tan Z, Kong S-C, Reitz RD, Modeling premixed and direct injection SI engine combustion using the G-equation model, SAE 2003-01-1843.

[55] Tan Z, Reitz RD, Modeling ignition and combustion in spark-ignition engines using a level set method, SAE 2003-01-0722.

[56] Peters N, Turbulent combustion, Cambridge university press, 2000.

[57] Ogink R, Golovitchev V, Gasoline HCCI modeling: an engine cycle simulation code with a multi-zone combustion model, SAE 2002-01-1745.

[58] Kokjohn SL, Reitz RD. Investigation of the roles of flame propagation, turbulent mixing, and volumetric heat release in conventional and low temperature diesel combustion. J Eng Gas Turbines Power 2011;133:102805.

[59] Kee RJ, Rupley FM, Miller JA, Chemkin-II: A Fortran chemical kinetics package for the analysis of gas-phase chemical kinetics,

[60] Curran HJ, Gaffuri P, Pitz WJ, Westbrook CK. A comprehensive modeling study of n-heptane oxidation. Combust. Flame 1998;114:149-77.

[61] Mehl M, Pitz WJ, Westbrook CK, Curran HJ. Kinetic modeling of gasoline surrogate components and mixtures under engine conditions. Proc. Combust. Inst. 2011;33:193-200.

[62] Jia M, Xie M. A chemical kinetics model of iso-octane oxidation for HCCI engines. Fuel 2006;85:2593-604.

[63] Liu YD, Jia M, Xie MZ, Pang B. Enhancement on a skeletal kinetic model for primary reference fuel oxidation by using a semidecoupling methodology. Energ. Fuel 2012;26:7069-83.

[64] Ra Y, Reitz RD. A reduced chemical kinetic model for IC engine combustion simulations with primary reference fuels. Combust. Flame 2008;155:713-38.

[65] Tanaka S, Ayala F, Keck JC. A reduced chemical kinetic model for HCCI combustion of primary reference fuels in a rapid compression machine. Combust. Flame 2003;133:467-81.

[66] Tsurushima T. A new skeletal PRF kinetic model for HCCI combustion. Proc. Combust. Inst. 2009;32:2835-41.

[67] Wang H, Yao M, Reitz RD. Development of a Reduced Primary Reference

Fuel Mechanism for Internal Combustion Engine Combustion Simulations. Energ. Fuel 2013;27:7843-53.

[68] Patel A, Kong S-C, Reitz RD, Development and validation of a reduced reaction mechanism for HCCI engine simulations, SAE 2004-01-0558.

[69] Yoo CS, Lu T, Chen JH, Law CK. Direct numerical simulations of ignition of a lean n-heptane/air mixture with temperature inhomogeneities at constant volume: Parametric study. Combust. Flame 2011;158:1727-41.

[70] Davis S, Law C, Laminar flame speeds and oxidation kinetics of iso-octane-air and n-heptane-air flames, in: Symposium (international) on combustion, Elsevier, 1998, pp. 521-7.

[71] Huang Y, Sung C, Eng J. Laminar flame speeds of primary reference fuels and reformer gas mixtures. Combust. Flame 2004;139:239-51.

[72] Kumar K, Freeh JE, Sung CJ, Huang Y. Laminar Flame Speeds of Preheated iso-Octane/O2/N2 and n-Heptane/O2/N2 Mixtures. Journal of Propulsion and Power 2007;23:428-36.

[73] van Lipzig JPJ, Nilsson EJK, de Goey LPH, Konnov AA. Laminar burning velocities of n-heptane, iso-octane, ethanol and their binary and tertiary mixtures. Fuel 2011;90:2773-81.

[74] Liu Y-D, Jia M, Xie M-Z, Pang B. Enhancement on a skeletal kinetic model for primary reference fuel oxidation by using a semidecoupling methodology. Energy & Fuels 2012;26:7069-83.

[75] Kazakov A, Foster DE, Modeling of soot formation during DI diesel combustion using a multi-step phenomenological model, SAE 982463.

[76] Tao F, Golovitchev VI, Chomiak J. A phenomenological model for the prediction of soot formation in diesel spray combustion. Combust. Flame 2004;136:270-82.

[77] Vishwanathan G, Reitz RD. Development of a Practical Soot Modeling Approach and Its Application to Low-Temperature Diesel Combustion. Combust. Sci. Technol. 2010;182:1050-82.

[78] Imren A, Haworth DC. On the merits of extrapolation-based stiff ODE solvers for combustion CFD. Combust. Flame 2016;174:1-15.

[79] Lu T, Law CK. A criterion based on computational singular perturbation for the identification of quasi steady state species: A reduced mechanism for methane oxidation with NO chemistry. Combust. Flame 2008;154:761-74.

[80] Lu T, Law CK, Yoo CS, Chen JH. Dynamic stiffness removal for direct numerical simulations. Combust. Flame 2009;156:1542-51.

[81] Lu T, Law CK. A directed relation graph method for mechanism reduction. Proc. Combust. Inst. 2005;30:1333-41.

[82] Lu T, Law CK. On the applicability of directed relation graphs to the reduction of reaction mechanisms. Combust. Flame 2006;146:472-83.

[83] Lu T, Law CK. Linear time reduction of large kinetic mechanisms with directed relation graph: n-Heptane and iso-octane. Combust. Flame 2006;144:24-36.

[84] Niemeyer KE, Sung C-J. On the importance of graph search algorithms for DRGEP-based mechanism reduction methods. Combust. Flame 2011;158:1439-43.

[85] Niemeyer KE, Sung C-J, Raju MP. Skeletal mechanism generation for surrogate fuels using directed relation graph with error propagation and sensitivity analysis. Combust. Flame 2010;157:1760-70.

[86] Lam S. Using CSP to understand complex chemical kinetics. Combust. Sci. Technol. 1993;89:375-404.

[87] Lam S. Reduced chemistry-diffusion coupling. Combust. Sci. Technol. 2007;179:767-86.

[88] Lam S, Goussis D. The CSP method for simplifying kinetics. Int. J. Chem. Kinet. 1994;26:461-86.

[89] Massias A, Diamantis D, Mastorakos E, Goussis D. An algorithm for the construction of global reduced mechanisms with CSP data. Combust. Flame 1999;117:685-708.

[90] Massias A, Diamantis D, Mastorakos E, Goussis D. Global reduced mechanisms for methane and hydrogen combustion with nitric oxide formation constructed with CSP data. Combust Theor Model 1999;3:233-57.

[91] Maas U, Pope SB. Simplifying chemical kinetics: intrinsic low-dimensional manifolds in composition space. Combust. Flame 1992;88:239-64.

[92] Gear CW, Numerical initial value problems in ordinary differential equations, Prentice Hall PTR, 1971.

[93] Petzold LR, A description of DASSL: A differential/algebraic system solver, in: Proc. IMACS World Congress, 1982, pp. 430-2.

[94] Brown P, Hindmarch A, Byrne G, DVODE: Computer Subroutine Package for Solving Ordinary Differential Equations, 1992.

[95] Mott DR, Oran ES, van Leer B. A quasi-steady-state solver for the stiff ordinary differential equations of reaction kinetics. J Comput Phys 2000;164:407-28.

[96] Shi Y, Green WH, Wong H-W, Oluwole OO. Accelerating multi-dimensional combustion simulations using GPU and hybrid explicit/implicit ODE integration. Combust. Flame 2012;159:2388-97.

[97] Qureshi SR, Prosser R, Implementation of α-QSS stiff integration methods for solving the detailed combustion chemistry, in: Proceedings of the World Congress on Engineering, 2007.

[98] Sun P, Chock DP, Winkler SL. An implicit-explicit hybrid solver for a system of stiff kinetic equations. J Comput Phys 1994;115:515-23.

[99] Dabdub D, Seinfeld JH. Extrapolation techniques used in the solution of stiff ODEs associated with chemical kinetics of air quality models. Atmos Environ 1995;29:403-10.

[100] Gear CW, Kevrekidis IG. Projective methods for stiff differential equations: problems with gaps in their eigenvalue spectrum. Siam J Sci Comput 2003;24:1091-106.

[101] Gao Y, Liu Y, Ren Z, Lu T. A dynamic adaptive method for hybrid

integration of stiff chemistry. Combust. Flame 2015;162:287-95.

[102] Pope SB. Computationally efficient implementation of combustion chemistry using in situ adaptive tabulation. 1997.

[103] Shi Y, Green WH, Wong H-W, Oluwole OO. Redesigning combustion modeling algorithms for the Graphics Processing Unit (GPU): Chemical kinetic rate evaluation and ordinary differential equation integration. Combust. Flame 2011;158:836-47.

[104] Jangi M, Bai X-S. Multidimensional chemistry coordinate mapping approach for combustion modelling with finite-rate chemistry. Combust Theor Model 2012;16:1109-32.

[105] Sun W, Gou X, El-Asrag HA, Chen Z, Ju Y. Multi-timescale and correlated dynamic adaptive chemistry modeling of ignition and flame propagation using a real jet fuel surrogate model. Combust. Flame 2015;162:1530-9.

[106] You X, Egolfopoulos FN, Wang H. Detailed and simplified kinetic models of n-dodecane oxidation: The role of fuel cracking in aliphatic hydrocarbon combustion. Proc. Combust. Inst. 2009;32:403-10.

[107] Hirasawa T, Sung C, Joshi A, Yang Z, Wang H, Law C. Determination of laminar flame speeds using digital particle image velocimetry: binary fuel blends of ethylene, n-butane, and toluene. Proc. Combust. Inst. 2002;29:1427-34.

[108] Held T, Marchese A, Dryer F. A semi-empirical reaction mechanism for n-heptane oxidation and pyrolysis. Combust. Sci. Technol. 1997;123:107-46.

[109] Zeppieri SP, Klotz SD, Dryer FL. Modeling concepts for larger carbon number alkanes: a partially reduced skeletal mechanism for n-decane oxidation and pyrolysis. Proc. Combust. Inst. 2000;28:1587-95.

[110] Wang H, You X, Joshi AV, Davis SG, Laskin A, Egolfopoulos F, Law CK. USC Mech Version II. High-Temperature Combustion Reaction Model of H2/CO/C1-C4 Compounds. http://ignis.usc.edu/USC_Mech_II.htm May 2007.

[111] Li J, Zhao Z, Kazakov A, Chaos M, Dryer FL, Scire JJ. A comprehensive kinetic mechanism for CO, CH2O, and CH3OH combustion. Int. J. Chem. Kinet. 2007;39:109-36.

[112] Lutz AE, Kee RJ, Miller JA, SENKIN: A FORTRAN program for predicting homogeneous gas phase chemical kinetics with sensitivity analysis, SAND-87-8248, Sandia National Labs., Livermore, CA, USA.

[113] Kee RJ, Grcar JF, Smooke M, Miller J, Meeks E. PREMIX: a Fortran program for modeling steady laminar one-dimensional premixed flames. Sandia National Laboratories Report 1985.

[114] Metcalfe WK, Burke SM, Ahmed SS, Curran HJ. A hierarchical and comparative kinetic modeling study of C1− C2 hydrocarbon and oxygenated fuels. Int. J. Chem. Kinet. 2013;45:638-75.

[115] Golovitchev VI, Nordin N, Jarnicki R, Chomiak J, 3-D diesel spray simulations using a new detailed chemistry turbulent combustion model, SAE 2000-01-1891.

[116] Wang H, Frenklach M. A detailed kinetic modeling study of aromatics formation in laminar premixed acetylene and ethylene flames. Combust. Flame 1997;110:173-221.

[117] Bergman M, Golovitchev VI, Application of transient temperature vs. equivalence ratio emission maps to engine simulations, SAE 2007-01-1086.

[118] Fieweger K, Blumenthal R, Adomeit G. Self-ignition of SI engine model fuels: a shock tube investigation at high pressure. Combust. Flame 1997;109:599-619.

[119] Ciezki H, Adomeit G. Shock-tube investigation of self-ignition of n-heptane-air mixtures under engine relevant conditions. Combust. Flame 1993;93:421-33.

[120] Kumar K, Freeh J, Sung C, Huang Y. Laminar flame speeds of preheated iso-octane/O2/N2 and n-heptane/O2/N2 mixtures. J Propul Power 2007;23:428-36.

[121] Dagaut P, Reuillon M, Cathonnet M. High Pressure Oxidation of Liquid Fuels From Low to High Temperature. 1. n-Heptane and iso-Octane. Combust. Sci. Technol. 1993;95:233-60.

[122] Dagaut P, Reuillon M, Cathonnet M. High Pressure Oxidation of Liquid Fuels from Low to High Temperature. 2. Mixtures of n-Heptane and iso-Octane. Combust. Sci. Technol. 1994;103:315-36.

[123] Bakali AE, Delfau J-L, Vovelle C. Experimental study of 1 atmosphere, rich, premixed n-heptane and iso-octane flames. Combust. Sci. Technol. 1998;140:69-91.

[124] Marchal C, Delfau J-L, Vovelle C, Moréac G, Mounaïm-Rousselle C, Mauss F. Modelling of aromatics and soot formation from large fuel molecules. Proc. Combust. Inst. 2009;32:753-9.

[125] Sarathy SM, Vranckx S, Yasunaga K, Mehl M, Oßwald P, Metcalfe WK,Curran HJ. A comprehensive chemical kinetic combustion model for the four butanol isomers. Combust. Flame 2012;159:2028-55.

[126] http://www.sandia.gov/ecn/ Egine Combustion Network.

[127] Beale JC, Reitz RD. Modeling spray atomization with the Kelvin-Helmholtz/Rayleigh-Taylor hybrid model. Atomization Spray 1999;9:623-50.

[128] Siebers DL, Higgins B, Flame lift-off on direct-injection diesel sprays under quiescent conditions, SAE 2001-01-0530.

[129] Mohan B, Yang W, kiang Chou S. Development of an accurate cavitation coupled spray model for diesel engine simulation. Energ. Convers. Manage 2014;77:269-77.

[130] Zhou D, Yang W, An H, Li J, Shu C. A numerical study on RCCI engine fueled by biodiesel/methanol. Energ. Convers. Manage 2015;89:798-807.

[131] Zhou DZ, Yang WM, An H, Li J. Application of CFD-chemical kinetics approach in detecting RCCI engine knocking fuelled with biodiesel/methanol. Appl Energ 2015;145:255-64.

[132] Sahoo D, Petersen B, Miles PC, Measurement of equivalence ratio in a light-duty low temperature combustion diesel engine by planar laser induced

fluorescence of a fuel tracer, SAE 2011-24-0064.

[133] Li J, Yang W, An H, Zhou D, Yu W, Wang J, Li L. Numerical investigation on the effect of reactivity gradient in an RCCI engine fueled with gasoline and diesel. Energ. Convers. Manage 2015;92:342-52.

[134] Kokjohn S, Hanson R, Splitter D, Kaddatz J, Reitz R, Fuel reactivity controlled compression ignition (RCCI) combustion in light-and heavy-duty engines, SAE 2011-01-0357.

[135] Li YP, Jia M, Chang YC, Liu YD, Xie MZ, Wang TY, Zhou L. Parametric study and optimization of a RCCI (reactivity controlled compression ignition) engine fueled with methanol and diesel. Energy 2014;65:319-32.

[136] Dec J. A Conceptual Model of DI Diesel Combustion Based on Laser-Sheet Imaging. Final manuscript received in March 1999 1997;SAE 970873.

[137] Abraham J, Bracco F, Reitz R. Comparisons of computed and measured premixed charge engine combustion. Combust. Flame 1985;60:309-22.

[138] Bergeron CA, Hallett WL. Ignition characteristics of liquid hydrocarbon fuels as single droplets. The Canadian Journal of Chemical Engineering 1989;67:142-9.

[139] Pope SB. The computation of constrained and unconstrained equilibrium compositions of ideal gas mixtures using Gibbs function continuation. Cornell University, Ithaca, NY, Report No. FDA 2003;03-2.

[140] Zhou D, Yang W, Li J, Tay KL. Simplified fuel cracking process in reduced mechanism development: PRF–PAH kinetic models for combustion and soot prediction. Fuel 2016;182:831-41.

[141] Hu B, Rutland CJ, Shethaji TA. A Mixed-Mode Combustion Model for Large-Eddy Simulation of Diesel Engines. Combust. Sci. Technol. 2010;182:1279-320.

[142] Metghalchi M, Keck JC. Burning velocities of mixtures of air with methanol, isooctane, and indolene at high pressure and temperature. Combust. Flame 1982;48:191-210.

[143] Gulder OL, Correlations of laminar combustion data for alternative SI engine fuels, SAE 841000.

[144] Yang S, Reitz RD, Integration of a continuous multi-component fuel evaporation model with an improved G-equation combustion and detailed chemical kinetics model with application to GDI engines, 2009-01-0722.

[145] Kech JM, Reissing J, Gindele J, Spicher U, ‘Analysis of the Combustion Process in a Direct Injection Gasoline Engine, in: COMODIA 98, 4th Int. Symp. on Diagnostics and Modeling of Combustion in Internal Combustion Engines, 1998.

[146] Nagle J, R. Stickland-Constable Proceedings of the Fifth Carbon Conference, vol. 1, in, Pergamon Press, Oxford, 1962.

[147] Neoh K, Howard J, Sarofim A, Effect of oxidation on the physical structure of soot, in: Symposium (International) on Combustion, Elsevier, 1985, pp. 951-7.

[148] Splitter D, Hanson R, Kokjohn S, Wissink M, Reitz R, Injection effects in low load RCCI dual-fuel combustion, SAE 2011-24-0047.

[149] Weinan E, Engquist B, Li X, Ren W, Vanden-Eijnden E. Heterogeneous multiscale methods: a review. Commun. Comput. Phys 2007;2:367-450.

[150] Gou X, Sun W, Chen Z, Ju Y. A dynamic multi-timescale method for combustion modeling with detailed and reduced chemical kinetic mechanisms. Combust. Flame 2010;157:1111-21.

[151] Weinan E. Analysis of the heterogeneous multiscale method for ordinary differential equations. Commun. Math. Sci 2003;1:423-36.

[152] Maclean J, Gottwald GA. On convergence of the projective integration method for stiff ordinary differential equations. arXiv preprint arXiv:1301.6851 2013.

[153] Pernice M, Walker HF. NITSOL: A Newton iterative solver for nonlinear systems. Siam J Sci Comput 1998;19:302-18.

[154] Ó Conaire M, Curran HJ, Simmie JM, Pitz WJ, Westbrook CK. A comprehensive modeling study of hydrogen oxidation. Int. J. Chem. Kinet. 2004;36:603-22.

[155] Smith GP, Golden DM, Frenklach M, Moriarty NW, Eiteneer B, Goldenberg M,Gardiner WJ. GRI 3.0. Gas Research Institute, Chicago, IL, http://www.me.berkeley.edu/gri_mech 2000.

[156] HUI A, Combustion Process and Emission Formation in Diesel Engines Fuelled by Biofuels and Blend Fuels, 2013.